



FACULTY
OF MATHEMATICS
AND PHYSICS
Charles University

DOCTORAL THESIS

Iurii Melnichuk

Nano-structured multicomponent plasma polymers for controlled immobilization of biomolecules

Charles University, Department of Macromolecular Physics

Supervisor of the doctoral thesis: Doc. Ing. Andrey Shukurov, Ph.D.

Study programme: Physics

Specialization: F4 – Biophysics, Chemical and Macromolecular Physics

Prague 2016

I declare that I carried out this doctoral thesis independently, and only with the cited sources, literature and other professional sources.

I understand that my work relates to the rights and obligations under the Act No. 121/2000 Coll., the Copyright Act, as amended, in particular the fact that the Charles University has the right to conclude a license agreement on the use of this work as a school work pursuant to Section 60 paragraph 1 of the Copyright Act.

In Prague, 29th December 2016

“When you play the game of thrones, you win or you die. There is no middle ground.”

– **George R.R. Martin, A Game of Thrones**

This thesis was the biggest task I have ever taken. An outcome could be either giving up or making it done. A balance was shifted to the favorable one only because of people supported me. Your support made the victory inevitable. I devote my thesis to each of you.

Thank you

Andrey Choukourov, my supervisor, for a guidance through an academic world of research, excellent leadership and transformation of thesis from prototype to end-product.

Hynek Biederman, Danka Slavínská and Lenka Hanyková for sharing extensive knowledge and creating an auspicious environment for study.

Ivan Gordeev for being an "elder brother" and introducing experimental facilities.

Pietro Favia and Fabio Palumbo, my hosts at the University of Bari, for a memorable time inside and outside of laboratory; ensuring absolute assistance to accomplish my scientific mission.

Lucie Bačáková and Marta Vandrovcová for teaching me how cells are similar to people.

Marcela Bilek for demonstrating a joy of being scientist and endless ideas.

Artem Ryabov for being Artem Ryabov, a theoretical physicist with a human DNA.

Ondřej Kylián for answering numerous questions and a passion for Italy.

Jan Hanuš for being XPS guru and traveler to distant destinations.

Jaroslav Kousal for bringing to the table Moravian accent and out-of-the box thinking.

Anna Kuzminova, Artem Shelemin, Daniil Nikitin, Martin Petr, Mykhajlo Vaydulych, colleagues from the Department of Macromolecular Physics, for sharing laughter, tea and hard work.

Michal Hauf, mejor amigo, for journeys and stories we created together; your positive attitude cheered me up thousand times and counting.

Clara Melniczuk for French elegance and Melniczuk soul.

Jan Thustak, for empowering my life journey by setting an example of creator and start-up artist. Worknb!

Aleksandra Zheleznova; Each your postcard brings me a small part of city you visit.

Hedvinka Boukalová for questions, listening and reminders that human behavior consists of rational AND emotional parts.

Francis Hellyer for BIG IDEAS of making the world better place and believing in me.

Fellow Members of VŠE Toastmasters International for excellence in public speaking and leadership. Every Tuesday, you recharge my inner batteries.

Mom, Dad, Granny; I have no words to describe a scale of your input into my life. With you, I was able to get where I am now and regardless of the situation I knew I could count on you.

Dear sister for love and care that make each of us stronger and push borders of possible further.

Název práce: Nanostrukturované plazmové polymery pro řízenou imobilizaci biomolekul

Autor: Iurii Melnichuk

Katedra/Ústav: Katedra Makromolekulární Fyziky/Univerzita Karlova

Vedoucí doktorské práce: Doc. Ing. Andrey Shukurov, Ph.D.

Abstrakt: V této práci studujeme možnosti aplikace nanostruktur při funkcionalizaci povrchů pro interakce s biomolekulami.

V první části práce zkoumáme vznik a počáteční stadia růstu tenkých nanostrukturovaných polymerních vrstev nanášených metodou vakuové termální depozice. Růst polyethylenových (PE) ostrůvků je diskutován jak z hlediska kinetických rovnic, tak pomocí teorie dynamického škálování. Druhá část práce je věnována imobilizaci proteinů prostřednictvím kovalentního navázání na nanostrukturované povrchy aktivované bariérovým výbojem. Diskutujeme jak ovlivňuje morfologie povrchu a přítomnost tropoelastinu proces přežívání buněk na takových površích. Ultra-tenké hydrokarbonové vrstvy schopné imobilizace proteinů jsou vytvořeny metodou plazmové polymerace.

Mezi hlavní výsledky práce patří stanovení kritického rozměru ostrůvků a objasnění průběhu nukleace v počáteční fázi jejich růstu. Ošetření PE nanostruktur atmosférickým nízko-teplotním plazmatem vede k jednoduché a účinné kovalentní imobilizaci proteinů na povrchu. Chování buněk na takových površích je závislé na nano-drsnosti. Biologická odezva buněk byla nejvyšší pro kombinaci tropoelastinu s relativně hladkými povrchy.

Klíčová slova: Polyethylen, nano-strukturovaná tenká vrstva, nízkoteplotní plazma, ostrůvkový růst, imobilizace bílkovin

Title: Nano-structured multicomponent plasma polymers for controlled immobilization of biomolecules

Author: Iurii Melnichuk

Department / Institute: Department of Macromolecular Physics/Charles University

Supervisor of the doctoral thesis: Doc. Ing. Andrey Shukurov, Ph.D.

Abstract: The aim of this thesis is to highlight the feasibility of tailored nano-structures in functionalizing surfaces for biointerfacial interactions. Development of new techniques for the production of nanoscaled biomaterials can be of use in a variety of medical and biological applications, e.g. biosensors, microarrays, drug sensors, implants, blood-contacting devices.

This thesis first examines the early stages of nano-structured thin film growth fabricated by vapor phase deposition of poly(ethylene). We discuss island growth within a framework of rate equation theory, dynamic scaling theory and capture zone distribution. In a second stage, we test dielectric barrier discharge to activate PE nano-pattern for covalent immobilization of proteins. Finally, we assess cell behavior on surfaces in dependence on morphology and the presence of cell adhesive protein tropoelastin. We employ plasma polymerization to produce ultrathin hydrocarbon layer capable of protein anchoring.

The thesis findings for the first time manifest the critical island size and nucleation mechanism of the initial stages of macromolecular film growth. Treatment of poly(ethylene) nanopattern with atmospheric low-temperature plasma enables one-step covalent surface immobilization of proteins. Biological response of cells is the highest for tropoelastin-mediated flat plasma polymers. Additionally, it is concluded that cell behavior depends on the surface nanoroughness.

Keywords: poly(ethylene), nano-structured thin film, low-temperature plasma, island growth, protein immobilization

Contents

1. INTRODUCTION	1
1.1. Micro- and nanopatterned surfaces	1
1.1.1. Bottom-up: general concepts of thin film growth	3
1.1.2. Issues specific to organic thin film growth	9
1.1.3. Fabrication of organic micro- and nanostructures	10
1.1.4. Nanostructured materials in biomedicine	18
1.2. Plasma surface modification of polymers for covalent protein immobilization	19
1.2.1. Role of surface embedded radicals for biomolecule immobilization	21
1.2.2. Surface modification of polymer films with a dielectric barrier discharge at atmospheric pressure	22
1.2.3. Protein immobilization on plasma polymer thin films	24
1.3. Aims of the doctoral thesis	26
2. EXPERIMENTAL	27
2.1. Experimental apparatus, facilities and specimens	27
2.1.1. Vapor phase deposition	27
2.1.2. Low pressure plasma activation	29
2.1.3. Atmospheric pressure dielectric barrier discharge activation	29
2.2. Methods of sample characterization	31
2.2.1. X-ray photoelectron spectroscopy (XPS)	31
2.2.2. Nuclear magnetic resonance spectroscopy (NMR)	31
2.2.3. Sessile droplet method for wettability measurements	32
2.2.4. Ellipsometry	32
2.2.5. Fourier transform infrared spectroscopy (FTIR)	32
2.2.6. Gel permeation chromatography (GPC)	33
2.2.7. Atomic force microscopy	33
2.2.8. Calculation of scaled island size distribution	33
2.2.9. Data processing for analysis of capture zone distributions	34
2.3. Biological tests	36
2.3.1. Attachment of proteins	36
2.3.2. Cell seeding and culture conditions	37

2.3.3. Evaluation of the cell number	38
2.3.4. Measurement of the cell adhesion area	38
2.3.5. Statistical analysis	38
3. RESULTS AND DISCUSSION	39
3.1. Growth of PE islands fabricated by vapor phase deposition	39
3.1.1. Chemical composition	39
3.1.2. Island growth	42
3.1.3. Rate equation theory	45
3.1.4. Dynamic scaling theory	49
3.1.5. Capture zone distributions	52
3.2. Dielectric barrier discharge activation of PE nano-pattern for covalent immobilization of biomolecules	55
3.2.1. Types of PE nano-patterns for plasma activation	56
3.2.2. DBD plasma modification of continuous PE film	58
3.2.2.1. <i>Surface roughness and morphology</i>	58
3.2.2.2. <i>Surface chemistry</i>	61
3.2.2.3. <i>Wettability analysis</i>	64
3.2.3. Immobilization of BSA on DBD activated PE films	65
3.3. Control of osteoblast-like cell adhesion using a PE nano-pattern	68
3.3.1. Films analysis	69
3.3.2. Protein immobilization studies	73
3.3.3. Osteoblast cell adhesion, growth and differentiation	78
CONCLUSIONS	83
BIBLIOGRAPHY	84
LIST OF TABLES	96
LIST OF ABBREVIATIONS	97
ATTACHMENTS	99
AUTHOR'S CONTRIBUTION	105

1. INTRODUCTION

1.1. Micro- and nanopatterned surfaces

Human civilization strives for exploration of nature on any possible scale. The diameter of the observable universe of 91 billion light-years (8.6×10^{26} m) [1] is on the large magnitude side. On the diametrically opposite side, material science operates with the smallest unit of matter – atom, being approximately 10^{-10} m. The scale in this thesis is close to the lower bound. We will research and discuss micro- and nanostructures. According to [2], nanostructures are “structures that are defined as having at least one dimension between 1 and 100 nm”. Similarly, one may claim a definition for microstructures as structures having at least one dimension in range of micrometers.

Undoubtedly, microstructures gained a profound attention in the late twentieth and early twenty-first centuries when computers with microstructured components demonstrated calculation powers never seen before. Raising in electronics happened because of replacement of discrete circuits in electronic devices with integrated circuits (ICs). A discrete circuit is constructed from individual electronic components while an IC contains them all on one chip. Performance wise, IC is better due to faster switch times and shorter wire length between components. To be financially viable, the microelectronics industry aims to produce ICs with more and more transistors per unit area. More transistors per chip means more computing power, more computing power means electronic systems with better functionality and performance. The first generation of complementary metal-oxide semiconductor (CMOS) chips were produced by 10 μm process [3]. In 2014, a minimum feature size reached a value of 14 nm [4].

Nanostructured materials contributed greatly to the miniaturization of electronic devices; unsurprisingly, scientists soon realized that new type of materials are attractive for applications outside of electronics such as biomedical applications. In biomedicine, micro- and nano-structures provide solutions for tissue engineering, drug delivery, biosensing, analytical methods [5], tailoring cell function and cell proliferation, implantable devices, etc.

There are two basic categories currently adopted in research into nanostructures. The first category comprises thin or thick nanostructured films,

which manifest mechanical, catalytic, optical and magnetic properties different from microstructured analogues. A wide range of materials including metals, metal-oxides, polymers and plasma polymers is used in fabrication of such coatings [6], [7].

The second category considers patterns of organized nanoislands, i.e. objects obtained in submono-/sublayer growth. In this case, surfaces with nanofeatures have regions of different structure. Extra heterogeneity occurs when materials of substrate and islands are different. This is exemplified in the work performed by Brétagnolet al. [8] who demonstrated selective bonding of protein on nano-scale patterns of plasma-polymerized acrylic acid (PAAC). A substrate underneath was plasma-polymerized poly(ethylene oxide)-like (PEO-like) layer with prominent non-fouling character.

There are different ways to build up nanostructured systems with characteristic size ≤ 100 nm either or both in horizontal and vertical dimensions. Classification of nanofabrication methods is graded on the basis of phenomena happening during the creation of nanoscale structures [9]. There are two main types: “top-down” and “bottom-up” methods. A grand strategy of the top-down approach is to start from larger dimensions and reduce pattern to the desired size by nanofabrication tools. This philosophy is implemented in conventional lithography where mask shades required pattern of micro-/nanostructured film and uncovered material is etched away. A family of top-down approaches extend over mechanical etching, scanning probe lithography, nanoimprint lithography and block co-polymer lithography, etc. [10], [11].

Bottom-up nanopatterning techniques construct nanoscale assemblies from atomic or molecular building blocks. Bottom up nanofabrication takes advantage of self-organization of adsorbate atoms/molecules on a solid substrate. By this route, final structure can be specified on the lowest level and multifunctional nanostructural materials and devices can be produced. This methodology is also considered as a low waste and high percentage of material end up in the final system.

1.1.1. Bottom-up: general concepts of thin film growth

Bottom-up production techniques construct micro-/nano-scale structures from basic components - atoms, molecules, macromolecules. In practice, the fabrication process generally involves the deposition of particles onto the solid substrate. Surface processes taking place in the initial stages of film growth define morphology and properties of final thin film. Dinelli et al. examined the charge carrier mobility in sexithienyl thin films as a function of layer numbers [12]. The research demonstrated that “only the first two molecular layers next to the dielectric interface contribute to the charge transport”.

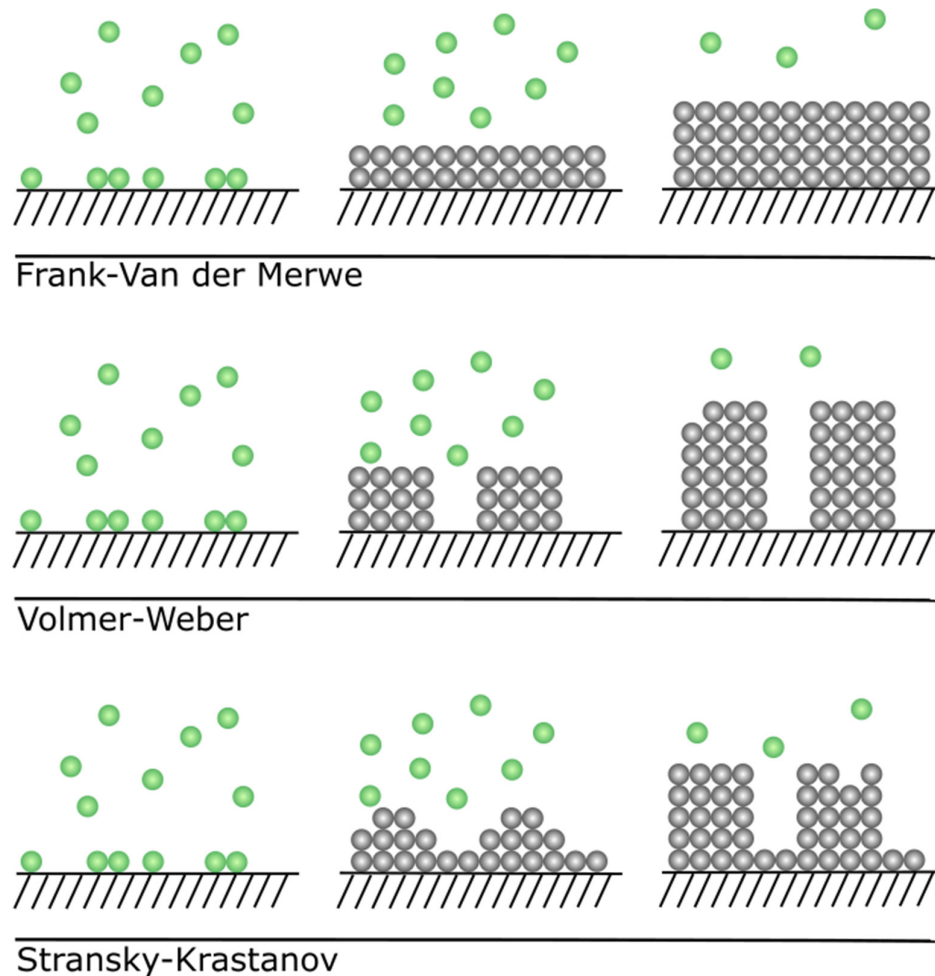


Figure 1. Simplified growth modes on solid surfaces: Frank-Van der Merwe (layer by layer), Volmer-Weber (islands), Stranski-Krastanov (layer plus islands).

According to the classical work by Bauer [13], growth on singular (flat) surfaces belongs to one of the three modes, which are depicted in Figure 1. The concept of surface and interface energies (the free energy of the substrate surface, γ_s , the free energy of interface between the film surface and the vapor, γ_f , and the surface free energy between film and substrate, γ_i) describes growth relation between adsorbates and substrate. Depending on the result of competition of surface energies

$$\Delta\gamma = \gamma_f + \gamma_i - \gamma_s \quad (1)$$

during deposition, the different growth modes occur. Sum of the surface energy values corresponds to three different growth morphologies:

- $\Delta\gamma < 0, \gamma_f + \gamma_i < \gamma_s$, Frank-Van der Merwe (layer-by-layer)

If delta is negative, monolayers of the evaporated material grow one after another. The scenario is fulfilled because molecules from the vapor are more strongly bound to the substrate than to each other. Frank-Van der Merwe mode is often desired in fabrication of smooth films with homogenous thickness and was observed in semiconductor growth [14], [15].

- $\Delta\gamma > 0, \gamma_f + \gamma_i > \gamma_s$, Volmer-Weber (islands starting at the first monolayer)

In the island mode, delta is positive, i.e. the free substrate surface energy is lower than the total of the free surface energy of the film and of the interfacial energy. Therefore, most energetically favorable situation for the system is when adsorbates stick together in islands and minimize contact with the substrate. Vacuum-deposited thin films that follow the Volmer-Weber structure expanded from metal and inorganic deposits to organic molecular compounds (see 1.1.3. “Fabrication of micro- and nanostructures”).

- $\Delta\gamma < 0 \rightarrow \Delta\gamma > 0$, Stranski-Krastanov (SK) (layer plus islands after a certain critical thickness)

The case of SK features a change in value of delta combining the two previous scenarios. When at the start of the growth delta is negative, one or more layers are formed (usually referred as wetting layer). After the wetting layer is formed, influence of substrate is shielded and delta becomes positive. Continuation of deposition leads to clustering of material.

In the scope of these thesis, the submonolayer structure formation in the Volmer-Weber mode is a center of interest. For a recent and thorough reviews about structuring in thin organic films beyond the first monolayer, we refer to Refs. [16], [17].

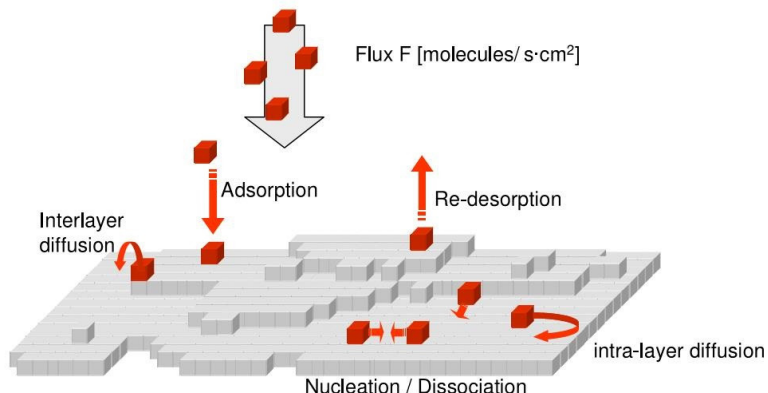


Figure 2. Schematic of fundamental processes relevant in thin-film growth [17].

Thin-film growth depends on the energetic factors of the film-vapor, substrate-film and substrate-vapor interactions. Under equilibrium conditions, the arriving to the system molecules carry enough thermal energy or have enough time to continue motion on the surface until they find an equilibrium (minimum) energy state. The growth in the equilibrium or close to it usually happens in crystal growth from melts. On the other hand, a non-equilibrium phenomenon describes situations when deposited species diffuse and freeze on the substrate considering energetic AND kinetic factors. It should be emphasized that thin film growth is often a non-equilibrium process complicated with kinetic aspects. The final structure depends on the rates of individual atomistic processes and significant post-growth reorganization. Elementary processes include (not necessary in order of occurrence) (see Figure 2. Schematic of fundamental processes relevant in thin-film growth [17].Figure 2)

- the adsorption of an atom or molecule by deposition,
- the re-evaporation of adsorbed molecule (re-desorption),
- the intralayer surface diffusion,
- the nucleation of the seed,
- the formation of a stable nucleus,
- the aggregation into existing islands,

- the decay of the existing island,
- the interaction between islands
- the edge diffusion of admolecule.

The submonolayer evolution of a thin film begins with lonely admolecule diffusion on the bare substrate. At some point, molecules may meet and form seeds that will decay or continue to grow by attaching other molecules. The probability of decay or growth is given by the interplay between the energy loss required to increase the interfacial area and the energy gain obtained from the difference of chemical potential between the lonely molecule on the surface and the molecule as a part of existing island. Typically, energy loss dominates for attachment of a molecule to smaller islands and energy gain prevails for attachment to larger ones. By definition, the amount of molecules in the largest island able to decay is denoted as a critical island size i (Figure 3). It means that the attachment of a single molecule to the cluster of i molecules ensures irreversible island formation. Molecules newly arriving onto the surface will diffuse until they nucleate into new seeds or join the existing ones. The total number of islands per unit area increases in this regime. When the mean free path of diffusing admolecules becomes equal to the mean island separation, admolecules will attach to existing islands with much higher probability than create new seeds. This regime is called an aggregation regime and it is characterized by a constant number of islands per unit area. At later stage, islands coalesce and their surface density drops.

In the above consideration, we ruled out re-evaporation of incoming molecules. We also assumed that molecules arriving on top of an existing island will diffuse to its edge, go down one step and attach at the rim as a first layer particle (zero step barrier diffusion effect leading to two-dimensional island growth). Both assumptions were earlier justified for organic depositions [18], [19].

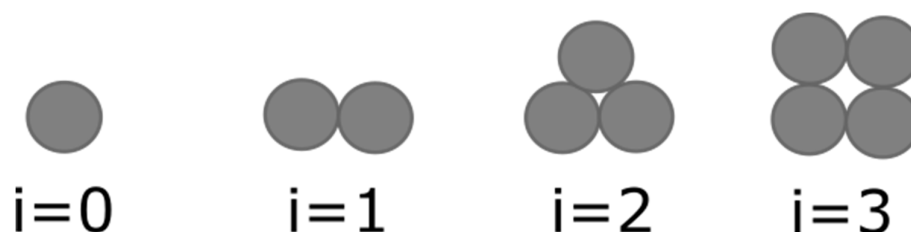


Figure 3. Graphical explanation of the relationship between critical island size and number of species constructing the island.

The concept of critical island size i is an essential quantitative descriptor of the nucleation and growth of films in the submonolayer regime. The critical size determines when islands become irreversible aggregates and it is crucial for understanding the regime of film growth, the final film structure and morphology [20].

A variety of indirect methods have been developed to extract this number. However, quantitative analyses were massively done for atomic systems and only recently were applied to small organic molecules. The aim of our research is to examine the initial island growth of model polymer poly(ethylene) (PE) on silicon by means of rate equation, dynamic scaling and capture zones scaling theories.

For the first time, the interplay between deposition, diffusion and desorption of the monomers for metallic film growth was quantified by the system of rate equations for the individual processes. On the basis of rate equation theory, Venables et al. [20] successfully predicted island number density N as a function of the external parameters: temperature T_D and deposition rate R :

$$N \propto \left(\frac{R}{v}\right)^{\alpha(i)} e^{E_N/k_b T_D}. \quad (2)$$

Here, E_N is the activation energy for homogeneous nucleation, $\alpha(i)$ is the scaling exponent depending on the critical nucleus size i , T_D is the deposition temperature, k_b is the Boltzmann factor, v is the particle jump rate on the surface. The particle jump rate is given by relation:

$$v = v_0 e^{-E_D/k_b T_D}, \quad (3)$$

where v_0 is the attempt frequency and E_D is the energy barrier the particle has to overcome.

Then, in pre-coalescence regime at constant temperature the maximum island density N_{sat} scales with deposition rate

$$N_{sat} \sim R^{\alpha(i)}. \quad (4)$$

Consequently, $\alpha(i)$ can be determined from the slope on the log-log plot of deposition rate versus saturated island density.

An alternative approach to estimate critical island size at complete condensation is to apply a Dynamic Scaling Theory (DST). The DST describes the island size distribution and its development with coverage. Compared to the rate

equation's approach for which experiments at different growth rates are necessary, experimental data for the DST analysis can be successfully obtained from even one sample if enough data points for better statistics are provided.

In the aggregation (precoalescence) regime of two-dimensional growth, according to the dynamic scaling assumption [21], the general scaling form is

$$N_a(\theta) = \theta f(u) \cdot A(\theta)^{-2}, \quad (5)$$

where θ is the coverage (ratio of the area occupied by islands to the total area of the substrate), $N_a(\theta)$ – the distribution of islands of area a per unit area, $A(\theta)$ - the mean island size, $u = \frac{a}{A(\theta)}$ and $f(u)$ is a universal scaling function for the island size distribution for a critical island size of i . When the DST holds, the distribution density $N_a(\theta)$ scales with the average island size $A(\theta)$.

Amar and Family in the study of diffusion-mediated systems [22] designed an analytical expression for the universal scaling function in the form

$$f_i(u) = C_i u^i \exp(-i a_i u^{1/a_i}), \quad (6)$$

where the constants C_i and a_i are indexed to indicate their dependence on i and satisfy the expressions¹ to assure normalization and proper asymptotic behavior of $f(u)$:

$$C_i = \frac{(i a_i)^{(i+1)a_i}}{a_i \Gamma[(i+1)a_i]}, \quad (i a_i)^{a_i} = \frac{(i a_i)^{(i+1)a_i}}{a_i \Gamma[(i+1)a_i]} \quad (7)$$

The most recent approach to extract critical island size is based on the Capture Zone Distributions (CZDs) [23]. In this type of analysis, capture-zones of growing islands are represented by proximity polygons of Voronoi cells with respect to the island centres. Considering CZD and DST, the former is less dependent on the accuracy of measurement of morphology and the surface scans with lower resolution allow to locate the island center of mass. Pimpinelli and Einstein [24] proposed to describe CZD by a single-parameter Generalized Wigner Distribution (GWD). The GWD contains only one parameter β and is the product of a power-law rise and a Gaussian decay:

¹ The gamma function for any real value of x is defined by the integral

$$\Gamma(x) = \int_0^{\infty} e^{-t} t^{x-1} dt$$

$$P_{\beta}(s) = a_{\beta} s^{\beta} \exp(-b_{\beta} s^2), \quad (8)$$

where $P_{\beta}(s)$ is the probability of finding a given value of the dimensionless area $s = v/\langle V \rangle$, v is the Voronoi cell size, $\langle V \rangle$ is the mean value of v , a_{β} and b_{β} are constants assuring the normalization of the function $P_{\beta}(s)$ to unity, with unit mean:

$$a_{\beta} = 2\Gamma\left(\frac{\beta+2}{2}\right)^{\beta+1} / \Gamma\left(\frac{\beta+1}{2}\right)^{\beta+2}, \quad b_{\beta} = [\Gamma\left(\frac{\beta+2}{2}\right) / \Gamma\left(\frac{\beta+1}{2}\right)]^2 \quad (9)$$

The coefficient β is described using $\beta=(2/d)(i+1)$, where $d=1,2$ is the spatial dimension.

1.1.2. Issues specific to organic thin film growth

Inorganic micro- and nanostructured films were in the origins of microelectronic revolution and were successfully applied in many other applications. A new milestone happened in the 1970s, when Nobel prize winners Heeger, Shirakawa and MacDiarmid discovered conductivity in conjugated polymers and oligomers [25]. Organic materials offer almost infinite number of examples. They can be produced case-by-case with tailored properties. Regardless of the application aim, mechanisms and fundamental processes of organic film growth should be examined and understood in order to achieve desired properties.

With respect to the nucleation and initial film growth, the difference between organic and inorganic building blocks can be classified as follows.

- 1) metals and inorganic semiconductors are considered as zero dimensional particles (their atomic size is much smaller than typical island length scale). Organic molecules are extended objects with complex spatial structure. Internal degrees of freedom are a fundamental distinction between growth of inorganic atomic and molecular organic systems.
- 2) The extended shape of organic molecules enriches the interaction potentials (molecule-molecule, molecule-substrate). Organic molecules have anisotropic configuration so that orientation of the admolecule relative to the substrate or to other molecules determines the strength and direction of the interaction.
- 3) Organic compounds have weak Van der Waals intermolecular forces and size exceeding lattice size; these factors open up possibilities for the non-epitaxial deposition [26] of high-quality thin films on variety of substrates.

- 4) All the mentioned above points influence film growth both in vertical and horizontal scale. In contrast to atomistic inorganic deposition, organic molecular conformation and orientation on surfaces are additional parameters that tremendously diversify the kinetics of growth (diffusion rates, energy barriers).

Despite the differences with organic films, inorganic systems offer models and approaches that can serve as a convenient starting point in exploring of the physics behind growth of organic thin films (rate equation, DST, CZD).

1.1.3. Fabrication of organic micro- and nanostructures

Historically, Langmuir-Blodgett films pioneered preparation of ultrathin organic films and monolayer control was realized by repeated immersion of solid substrate into liquid with self-assembled monolayer of an organic matter [27]. Later, an essential advance in growth and understanding of organic structures was achieved by deployment of low-pressure gas phase fabrication techniques. Experimentally, it made possible to grow a submonolayer nanostructured system containing island-type agglomerates. The deposition process, especially under conditions of ultrahigh vacuum (UHV), provided fine control over the growth, high chemical purity of environment, substrate and deposit components.

In this chapter, we will cover methods to form nanoscale organic interfaces and patterns with the focus set on vapor phase deposition including organic molecular beam deposition (OMBD) and plasma polymerization. The distinction between deposition of small organic molecules and macromolecules will be discussed. Finally, applications of organic nanostructured surfaces in biomedicine will be presented.

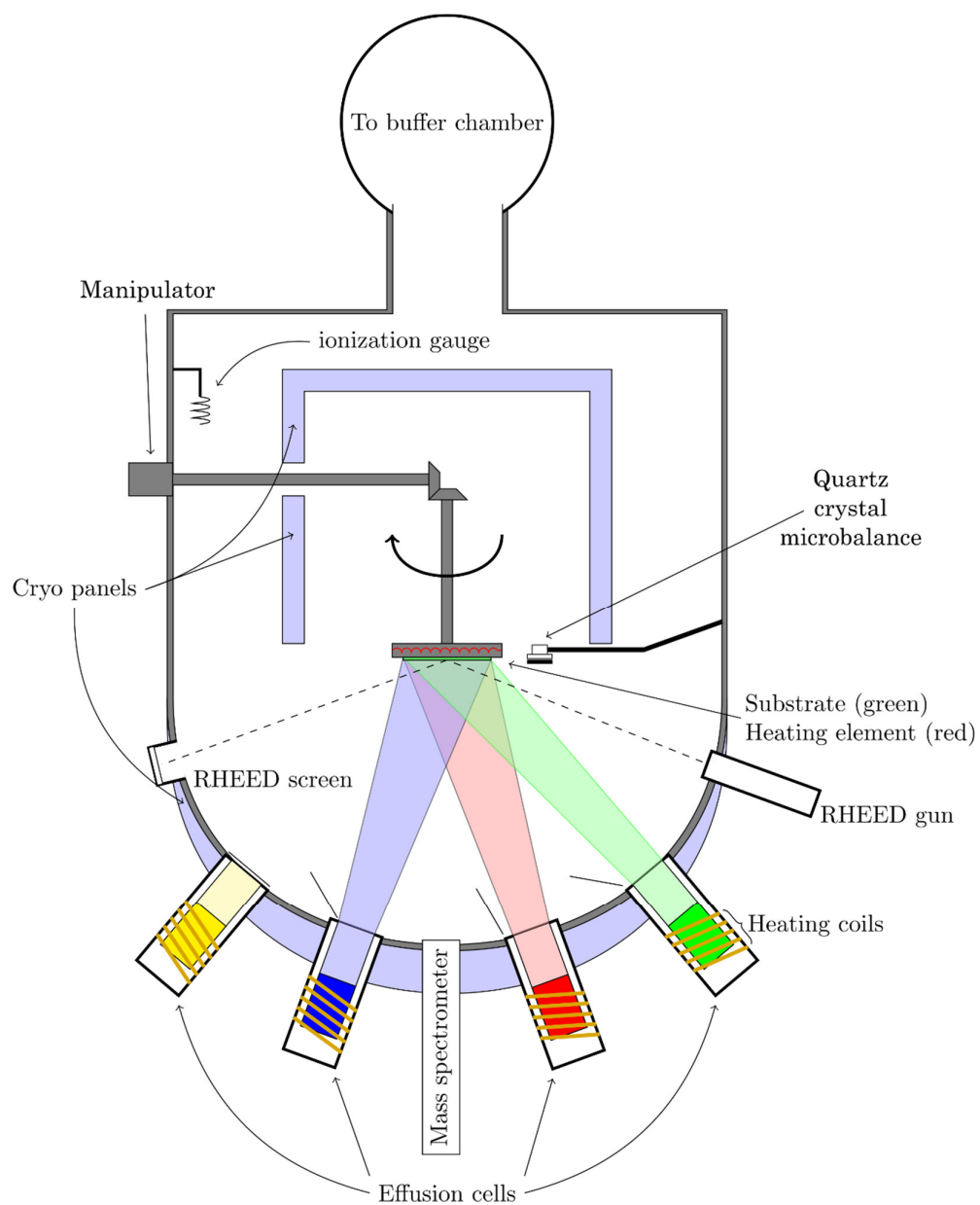


Figure 4. The experimental arrangement for fabrication of organic thin films by OMBD in UHV [28].

OMBD is an organic thin film growth process from the vapor phase of evaporated organic substance performed in UHV. The first reports on OMBD reflected the fact that experimental setup for growth of organic thin films, in essence, was slightly modified apparatus for molecular beam epitaxy used for inorganic materials. The schematic of UHV apparatus is shown on Figure 4. A working pressure is monitored by ionization gauge and it ranges from 10^{-5} to 10^{-9} Pa. The evaporant is located in a Knudsen cell (effusion cell heated by coils) in a form of purified powder or, rarely, a melt of organic source material. The organic molecular beam is aimed to the substrate by passing through a series of orifices. The molecular flux is controlled by temperature of Knudsen cell and mechanical shutter operating in “ON”-“OFF” regime. A quartz crystal microbalance (QCM) head is used for the measurements and adjustments of the deposition rate. The details about thin-film growth (crystalline structure, time evolution, surface roughness) can be closely scrutinized via *in situ* high-resolution characterization methods, such as reflection high energy electron diffraction (RHEED gun and screen) [29], [30], mass spectrometry, X-ray diffraction (XRD) [31], [32] or low He diffraction [33].

There are many organic systems involved in research of ultrathin films grown by OMBD and similar techniques. The most intensively studied materials are small aromatic or otherwise conjugated π -electron molecules. Majority of studies is focused on rod-like compounds (for example, acenes, phenylenes, etc.) and plate-like molecules (for example, phthalocyanines, porphyrins, etc.) [34]. Brief examinations of the molecular structure of dyes and organic semiconductors reveals rigid polycyclic core (Table 1). In the sub-monolayer coverage regime, height distribution of grown islands measured by Atomic Force Microscopy (AFM) (or any other appropriate characterization method) shows how molecules are oriented on surface because of conserved molecular dimensions. In terms of the growth physics, macrocyclic planar or polycyclic aromatic compounds are reported to form upright-standing or flat-lying clusters when deposited on various substrates, including silicon-dioxide surfaces.

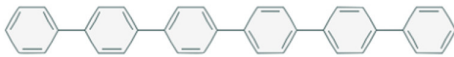
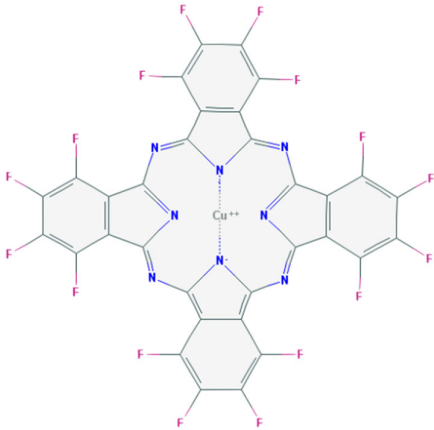
Organic molecule	2D structure	Dimensions	Molecular orientation on substrate
Pentacene (5A) [35]		16.01 Å × 7.90 Å [36]	Standing [37], [33], [38], [39], [40] Lying [41], [42], [38], [43]
para-Hexaphenyl (6P) [44]		26.24 Å × 8.09 Å [45]	Standing [46], [47], [48], [49] Lying [46], [47]
Diindenoperylene (DIP) [50]		18.40 Å × 7.00 Å [51]	Standing [51], [52], [17]
Copper hexadecofluorophthalocyanine (F16CuPc) [53]		14.50 Å × 14.50 Å [54]	Standing [55], [56] Lying [56]

Table 1. Organic semiconductor molecules and molecular orientation on substrate.

OMBD growth of thin films from small aromatic molecules contributed significantly to the understanding of underlying growth dynamics on heterogeneous interfaces. However, insufficient attention has been paid to the fundamental processes in the formation of thin films from large organic molecules (macromolecules, polymers). A specific feature of long carbon chains is various internal degrees of freedom. Vibrational, conformational and orientational degrees of freedom can effect growth behavior. For example, (PE) macromolecules composed of $-CH_2-$ building blocks, despite belonging to simplest polymers, possess significant extent of rotational freedom and may acquire a multitude of possible conformations on solid surfaces [57].

The use of polymers in the gas phase construction of nanostructured materials was limited due to absence of the clear answer to question: how can they be introduced into the gas phase? Heating in vacuum often leads to unwanted degradation of polymers. Nevertheless, Madorsky et al. [58], [59] reported thermal decomposition of PE under vacuum at temperature 300-400 °C. The group of Madorsky found that the flux of evaporated material consisted of oligomeric species of various size. The size distribution extended from a monomer to molecules of about $1000 \text{ g}\cdot\text{mol}^{-1}$. Later, Luff and White [60] explored two temperature stages of PE thermal evaporation. According to them, one could achieve vaporized material of different molecular weights depending on either the polymer was heated to temperature of 300 °C or above 350 °C. Despite the availability of studies done on Physical Vapor Deposition (PVD) of PE and characterization of these films [59]–[63], there is still a lack of information on the basic growth principles at the start of film growth. Li with coworkers [64], [65] uniformly patterned carbon nanotubes (CNTs) with PE single crystal rods perpendicular to the CNT axes. PE oligomers self-organized into numerous small islands with an average height of 10 nm on flat substrate surface uncoated with CNTs. The phenomenon of PE nanoislands synthesis was left beyond the scope of the discussion and kinetics of growth was hardly examined as well.

Implementation of low temperature plasma may further broaden the field of the gas phase production of nano-structured polymeric thin films. Organic molecules (or macromolecules) introduced into the glow discharge may undergo complex transformations due to interaction with energetic electrons, metastables and ultraviolet (UV) radiation. Thus-activated organic species may recombine both in

volume and on the surfaces adjacent to plasma contributing to the formation of solid polymer-like material. Randomness of the recombination processes results in the growth of highly cross-linked and branched polymeric networks Figure 5 displays idealized molecular structure of PE as compared to random structure of hydrocarbon plasma polymer.

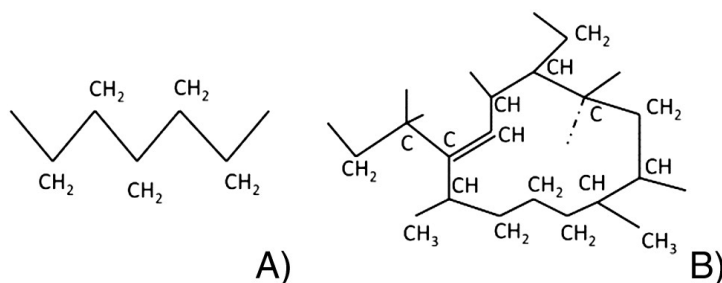


Figure 5. Schematic representation of (A) linear PE chain and (B) hypothetical structure of a hydrocarbon plasma polymer (taken from [66]).

First plasma polymers were allegedly produced already in the 18th century when deposition of "carbonaceous" layers from oil vapors exposed to atmospheric pressure electrical discharge was reported [67], [68], [69]. Later, König and Helwig [70] reported on the first deliberate deposition of hydrocarbon plasma polymers. The researchers polymerized benzene vapors in a glass bell jar reactor with parallel plate electrodes powered by 50 Hz, 2kV voltage. The intensive research on hydrocarbon plasma polymers was also performed by Kobayashi et al [71] who studied radio frequency (RF) discharges in many simple saturated and unsaturated hydrocarbons. The plasma polymers were found to be deficient with hydrogen as compared with corresponding precursors. Saturated hydrocarbons (alkanes: methane, ethane) were polymerized mainly due to hydrogen subtraction and the loss of hydrogen was the highest among the studied hydrocarbon molecules.

Formation of plasma polymer is typically explained by a complex interplay between the stages of initiation, propagation and termination of macromolecular chains combined with simultaneous ion bombardment and UV radiation. The group of Lam [72] reported the model for plasma-polymerized unsaturated hydrocarbons. They considered three conventional polymerization stages of initiation, chain propagation and termination, and investigated the probability of these stages either on the surface or in the gas phase. It was found that initiation in the gas phase and

chain propagation/termination on the surface provide the best agreement with the experimental data.

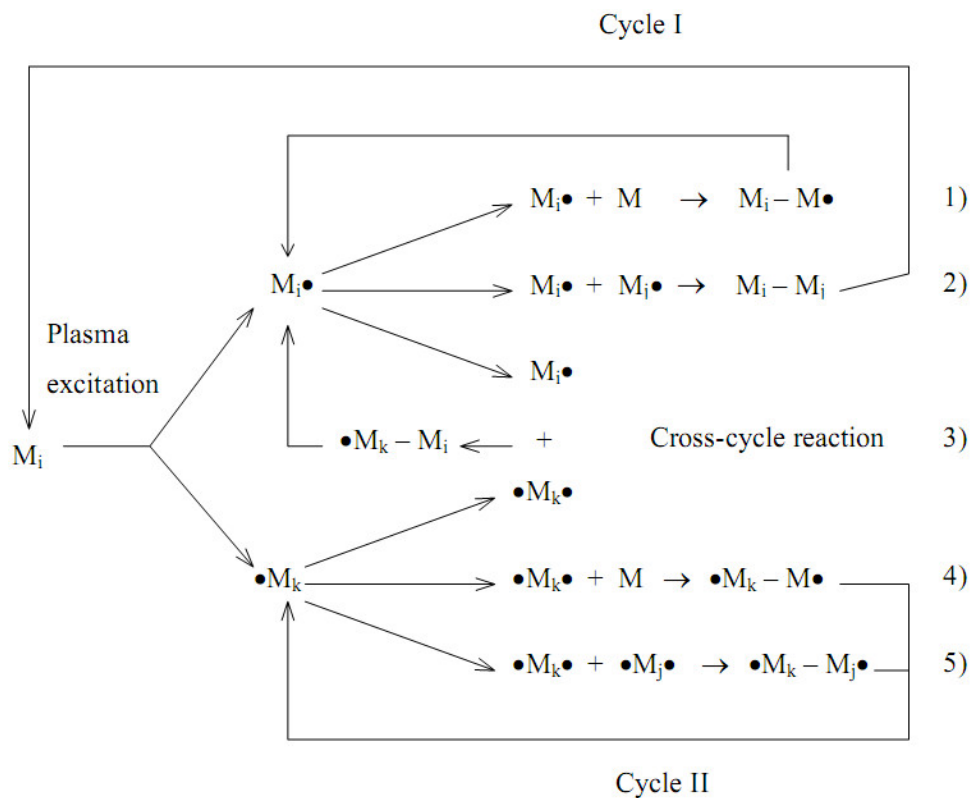


Figure 6. The rapid step-growth polymerization mechanism of plasma polymerization. M is any neutral species. $M\bullet$ refers to an activated monomer molecule. The $\bullet M\bullet$ is an activated difunctional species (taken from [73]).

Later, Yasuda suggested a competitive ablation and polymerization mechanism (CAP) that takes into account simultaneous bombardment of the growing film by energetic ions. Yasuda suggested that the film formation proceeds by rapid step-growth polymerization process via free radicals and considered two cycles of the mechanism [74]. The scheme of the bicyclic pathway is depicted in Figure 6. Here, M stands for the original organic molecule. After the plasma activation, monofunctional $M\bullet$ or difunctional $\bullet M\bullet$ free radicals appear which may attach to another precursor molecule or recombine with each other. Cycle I involves the iterative activation of the reaction products from monofunctional radicals whereas Cycle II proceeds similarly but the involvement of difunctional radicals. The reactions encountered within the cycles can be summarized as follows:

- (1) the first step of propagation through the addition mechanism;
- (2) termination by recombination;
- (3) recombination of mono- and diradicals;
- (4) see (1);
- (5) recombination of two difunctional radicals.

Hydrocarbon plasma polymers can also be obtained by RF magnetron sputtering of a polymer target. Ion bombardment cleaves the macromolecular bonds and results in the ejection of low molecular mass species from the target to the gas phase. In this case, a diverse mixture of the precursors is available instead of single-type molecules. Nevertheless, plasma polymerization processes are considered to be analogous to those proceeding in the discharges in volatile precursors. Using a PE target, Kholodkov et al. [75] deposited hydrocarbon plasma polymers. It was demonstrated that higher powers resulted in coatings more resembling conventional PE because of excessing heating and subsequent co-evaporation of PE oligomers.

Traditionally plasma polymers are referred to as smooth and pinhole-free thin films. Production of nanostructured plasma polymers is also possible, especially under an increased pressure of organic vapors at which the probability of the gas phase recombination is higher. In this case, the formation of nanoparticles in the discharge volume is typically observed [66]. Nanoparticles formed in the glow discharge can be further collected ex situ on solid substrates. This area of research has been extensively covered in the field of dusty plasmas and, later, in the field of gas aggregation cluster sources, yet it falls beyond the scope of this thesis. Nanostructuring of plasma polymers during their heterogeneous growth on the surface has been studied to much lesser extent. Michelmore et al. [76] reported on island-like topography of heptalamine [$\text{CH}_3\text{-(CH}_2\text{)}_6\text{-NH}_2$] plasma polymers. At smaller coverages, islands were 12-13 nm in height and about 100 nm in diameter. Fluorocarbon volatile precursors have also been shown to be effective in fabrication of micro- and nanostructure on the surface. Experiments with pulsed discharges or in afterglow produced different nanoobjects on the surface including ribbons, petals, domes, dots etc. [77]–[81]. Alternatively, RF magnetron sputtering of conventional poly(tetrafluoroethylene) at increased substrate/target distance resulted in the growth of fluorocarbon plasma polymer thin films with dome-like nanofeatures [82], [83]. In

both approaches, interplay between the ion bombardment and the flux of long-living CF_2 radicals was suggested to explain the formation of the observed nanostructure.

Plasma-assisted deposition of larger macromolecular species was also attempted, yet the research is scarce. Plasma-Assisted Vapor Phase Deposition of PEO has been found to produce thin films with tunable crosslink density [84], [85]; however, the coatings were extremely flat and no nanostructure was observed. The lack of structure was attributed to good wetting of hydrophilic silicon substrates by hydrophilic PEO oligomers which accumulated on the surface in the layer-by-layer mode. Hence, island type growth and nanostructuring can be expected if incompatible (for example, hydrophilic/hydrophobic) film/substrate combination is chosen.

1.1.4. Nanostructured materials in biomedicine

After conquering a key role in the fields of electronic and optical engineering, nano-structured systems have been introduced to many other areas, such as medicine and biology. Biosensors and microarrays, drug sensors, implants, blood-contacting devices and many others require surfaces with specifically engineered chemical composition and topography. New generation of biodevices follows the trend of miniaturization due to requirement of the smaller reagent quantities and lower detection limits. In many cases, biocompatibility of artificial device can be improved through understanding cell-material interaction. For example, successful integration or adverse body response to implant are determined largely by surface properties of the biodevice. While selection of materials with desirable bulk characteristics is important for implant functioning, biocompatibility is influenced by surface chemistry, charge, wettability and topography [27], [86], [87]. Once prosthesis is implanted into the body, biointerfacial interactions are initiated by non-specific adsorption of proteins. Micro- or nanostructured materials have a high surface to volume ratio and ensure bigger area (vs flat surfaces) available for adsorption of proteins [88]. After fast protein adsorption, cells probe and accommodate on the surface. When favorable active sites on adsorbed proteins are detected, cells attach to the surface via focal adhesion points that shape the cytoskeleton and connect it to the surface. There is strong evidence that among other factors surface topography can

affect cell alignment and migration [89]–[91]. It has been also reported that nanoscale topography of materials seems to be more beneficial for the proliferation of bone cells than microscale topography [92], [93].

Scanning probe-based lithography, electron-beam lithography and focused-ion beam lithography [94], [95] are very effective in creation of nano-patterned surfaces, although they feature common shortcomings including time consumption and treated area limitations [96]–[98]. Therefore, there exists an urgent need of new approaches for preparation of micro- and nanostructured surfaces.

1.2. Plasma surface modification of polymers for covalent protein immobilization

Design of new biomedical devices is of global interest, which interconnects many research areas in a common effort. The origins of therapeutic or diagnostic systems go back to ancient times when first artificial noses, ears, teeth, and eyes were produced [99]. Selection of materials was limited; for example, gold was popular in dental treatment and glass was used for eye prosthesis. Since then, new categories of biomaterials were discovered. The use of ceramics, metals, polymers, and composites became widespread practice [99]–[101].

Polymeric materials offer lightness, ease of forming into shapes, mechanical strength, and resistance to corrosion in chemically active environments [102]. Polymers are attractive in applications including, but not limited to, vascular grafts [103], drug delivery systems [104], bone implants [100] and biosensors [105]. Different polymers such as PE, polytetrafluoroethylene (PTFE), polypropylene (PP), polyesters (PES), polyamides (PA), polyurethane (PU), or polyetheretherketone (PEEK) are used [106].

PE can be viewed as the simplest example of polymer consisting of repeating CH_2 structural units. In biomedical field, low-density polyethylene (LDPE) (density range of $0.910\text{--}0.940\text{ g/cm}^3$) has diverse applications (e.g. artificial heart valves, stents, blood bags, etc.) because of its abundant supply, superior mechanical properties, low cost and biocompatibility [107]–[110].

Despite the intense studies on synthetic biomaterials and biomedical devices, response of the host body to implantable device remains often unfavorable causing

the rejection of the device [27]. While revision surgery is expensive, the biggest concern is the health of the patient being exposed to the danger of severe immune response. Most of unfavorable responses are inflammation, bacterial infection and encapsulation in a thick film of fibrotic tissue, i.e. a foreign-body response. Adverse foreign-body reaction is caused by the host's recognition of the implanted biomaterials as foreign. The induction of clots and the activation of immune response occur due to the accumulation of denatured protein on the surface of the medical device.

A strategy to make a surface of the implant more biocompatible is to attach a layer of bioactive protein. In this case, the surface is bio-functionalized with a protein interlayer. The protein is selected based on desired functions and location of action. Ideally, such coated layers should promote desirable biological responses in interactions with host tissues and mask the underlying surface of synthetic biomaterial. For example, bone morphogenetic proteins 2 was immobilized on the surface of implant and improved bone healing in *in vivo* studies on rabbits [111].

One form of protein attachment to surfaces is physisorption through the van der Waals attraction. However, physisorbed proteins are prone to desorption in biological fluids or to the replacement phenomenon (the Vroman effect) which leads to displacement of the pre-coated protein with other proteins from the biological media [112]. Another form of protein attachment is chemisorption with covalent bonds. The major advantage of covalently grafted molecules is a durable performance over extended periods [113]. For example, microarrays and biosensors with irreversibly attached biomolecules withstand washing and preserve orientation for maximum sensitivity [114]–[116].

Polymeric biomaterials are usually viewed as chemically inert and not providing much possibilities for chemical attachment of proteins. Plasma-based strategies can be utilized for activation of polymer surfaces, which can perform very effective in protein binding.

Plasma-based methods with advantages of dry processing, low energy consumption, low amounts of hazardous chemicals and waste offer an attractive approach to bind biologically active proteins on the surface of biomedical devices with enhancement of the performance of such devices and with decreasing the risk of undesirable host's response.

1.2.1. Role of surface embedded radicals for biomolecule immobilization

According to Bilek [117], covalent immobilization of biological macromolecules from a solution can be achieved through polymer surface activation by plasma immersion ion implantation (PIII). These plasma modifications affect only the surface and do not change the bulk of the implant material, thus preserving required mechanical properties. Established by Conrad et al [118], PIII method allows to extract ions from RF plasma and accelerate them by the application of negative high voltage. Bombardment of polymers with 5-20 keV ion energies results in macromolecular bond cleavage and in the formation of free radicals [117], [119]. For example, LDPE foils were treated by nitrogen PIII [120]. Their modification was examined in terms of unpaired electron density by electron paramagnetic resonance (EPR) as a function of the treatment time. The results confirmed that the LDPE surface layer became a reservoir of free radicals.

Biofunctionalization of PIII treated surface occurs in aqueous solution of targeted protein. The exact mechanism of the covalent binding of biomolecules to plasma-treated polymer surface in the solution is still unknown. It is believed that radicals captured in the sub-surface region of polymers react with accessible side groups of the adsorbed protein or via opening of carbonyl-based groups of the backbone polypeptide chain. Responsibility of free radicals for biomolecule immobilization was suggested after studies on the kinetics of covalent immobilization [121] and correlation between the degree of anchoring and radical density [122]. It was also found that proteins retained their biofunctionality after having attached covalently to PIII-treated polymer surfaces.

Nosworthy et al demonstrated attachment of poly-l-lysine and catalase to the PE surfaces after the RF plasma and PIII treatments [123]. Modified PE surfaces attached functional catalase, which remained on the surface after sodium dodecyl sulfate (SDS) or NaOH rinsing. After washing of untreated samples in SDS solution, biomolecules were easily removed. PE surfaces were also modified to achieve covalent attachment of dense and active layer of horseradish peroxidase (HRP) [124], [125].

The use of plasma methods for treatment of polymers has proved to be a universal recipe for the covalent binding of proteins in a single step. Nonetheless,

researches are mainly focused on continuous surfaces for plasma modification, leaving without proper attention nano-patterned structures with envisioned future in biosensors and diagnostic arrays [126].

1.2.2. Surface modification of polymer films with a dielectric barrier discharge at atmospheric pressure

Surface activation (radical formation) of polymers is possible using atmospheric pressure (AP) dielectric barrier discharge (DBD) as well.

The study of DBD was initiated almost 150 years ago when Siemens revolutionized ozone production [127]. Additionally, to contribution to ozone industry, DBD based applications became integrated in, for example, gas cleaning and synthesis, biological and chemical decontamination of media, plasma chemical vapor deposition, excitation of lasers and excimer lamps, etc. [128], [129]. Recently, increasing number of studies investigated the use of atmospheric plasma DBD for the modification of surfaces of polymers and biomaterials (e.g. polypropylene [130], poly(ethylene terephthalate) [131], [132], polyurethane [133], polyimide [134], PE [135], [136], poly(methyl methacrylate) [137] or polyamides [138]).

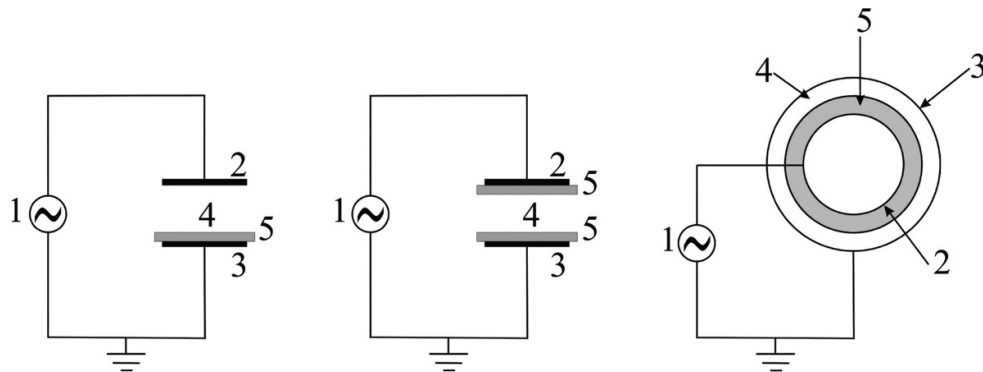


Figure 7. Schematic of typical planar and cylindrical DBD geometries: (1) Alternating current (AC) high-voltage (HV) source; (2) HV electrode; (3) ground electrode; (4) discharge gap; (5) dielectric barrier [139].

Schematic diagrams of typical DBD set-ups are presented in Figure 7. A feature of DBD systems is a presence of at least one dielectric barrier over metal electrode. Because of the insulator layer, operation of the discharge requires

alternating power source. For systems with insulators on both electrodes (Figure 7 center), voltage in the range from a few hundred V to several kV is applied to initiate plasma at atmospheric pressure. Overall, the discharge properties depend on several parameters, such as the dielectric type, AC voltage and frequency, electrode geometry, discharge gap, working gas type and pressure. The functioning discharge can be filamentary [140] or glow [141].

Kikani and collaborators [142] examined plasma treatment of PE by low-pressure plasmas and DBD at atmospheric pressure. They found that the physical and chemical changes of PE surface were more influenced by the low-pressure treatment. Regardless of the technique, charged particles (mainly ions) with energies exceeding 1 eV governed the polymer surface modification. At atmospheric pressure, mean free path is 5.7×10^{-8} cm and particles are involved in the frequent elastic and inelastic collisions. It means that in AP DBD possess energetic ions are not available for surface modification. Instead, UV radiation and highly reactive excited species are responsible for the changes induced in polymers upon atmospheric pressure plasma treatment.

DBD treatment of PE changes the chemical structure of the polymer. When the polymer is placed in the discharge, plasma induces dehydrogenation and ablation of low molecular weight species. Along polymer backbones free radicals are formed. Radicals on disrupted C-C and C-H bonds generally have three pathways to take. First, free radicals remain unreacted in the bulk, eventually forming a reservoir of embedded radicals. Second, they undergo rapid recombination and enhance the cross-linking of the material. Next, free radicals participate in reactions with species from the gas phase or, in case of inert working gas, with atmosphere immediately after the samples have been extracted. The last reactions are able to introduce new functionalities into the polymer and commonly these chemical groups contain oxygen and, to a lesser extent, nitrogen.

Ren with coworkers [135] showed that in contrast to untreated PE surfaces, the surface of PE modified with AP DBD in air contained new functionalities such as ketone $[-(C=O)-]$, acetal carbons $[-(O-C-O)-]$ and carboxyl carbons $[-(C-O)-O-]$. Other authors came to the same conclusion that after plasma treatment the PE surfaces obtain in abundance C-O and C=O bonds contributing to increasing surface energy of polymer [136], [142], [143].

1.2.3. Protein immobilization on plasma polymer thin films

Characteristic feature of plasma polymers is the availability of free radicals trapped within the network. Despite being often considered as unwanted products, trapped radicals can be used for covalent attachment of biomolecules. One particular feature of plasma polymer films that makes this approach particularly attractive is that deposition can be done virtually over any solid support. Moreover, plasma polymerization is well known for producing conformal coatings even over objects with complex shape, which can be advantageous for modification of real biomedical devices including, for instance, orthopedic devices.

Biomaterial functionalization technique built on plasma polymers is beneficial from economical and efficiency standpoints. The era of protein anchoring to plasma polymer layers started when Bohnert et al. [144] employed RF glow discharge to generate fluorocarbon surfaces with abundant free radicals for subsequent adsorption of albumin and fibrinogen. The control biomaterials, poly(ethylene terephthalate) (PET) and PTFE, showed higher protein elutability levels than the plasma functionalized surfaces. Resistance to elution was tested with usage of sodium dodecyl sulfate, a strong detergent capable of destroying physical interactions between a surface and a protein.

Further studies manifested a decisive role of the free radicals in the immobilization of proteins by forming covalent linkages. The degree of covalent binding increased with the radical density in a plasma polymer film [122], [145]. The effect of thickness on the covalent attachment supported the concept of the plasma polymer film acting as a reservoir of radicals. For example, level of tropoelastin covalent immobilization to plasma-polymerized acetylene grew linearly with the deposit thickness [122].

In the domains of biosensors and body implants, a dense layer of attached biomolecules faces a strict requirement of remaining bioactive. Studies on functionality of proteins bound to plasma polymer surfaces confirmed that, after adsorption from protein-containing solution, the protein layers retain the activity [119], [146]. When HRP was tested on uncoated PE controls, neither covalent anchoring nor enzyme bioactivity were detected. By contrast, hydrocarbon plasma polymer coatings deposited by RF plasma polymerization of n-hexane on PE

substrates enabled covalent coupling of the enzyme. Levels of covalent attachment and activity of enzyme were enhanced on surfaces fabricated with bias voltages of around 200 V than on no-biased hydrocarbon layers. Higher radical density on the biased samples contributed to an increase of surface energy by post-deposition reactions with atmospheric oxygen and introduction of polar groups. Hydrophilic surfaces usually preserve the native conformation of adsorbed protein and may contribute to retaining of biological activity as well.

1.3. Aims of the doctoral thesis

The thesis aims to design a nano-structured platform on the base of polymeric thin films for biomedical applications. In order to achieve this aim, we have:

- 1) Employed physical vapor deposition of polyethylene to observe the island-type growth of thin films with ex situ measurements of morphology and chemical structure;
- 2) Analyzed the nucleation and growth of two dimensional (2D) PE nano-island pattern in the framework of three different growth theories;
- 3) Examined changes of PE-evaporated surfaces after modification by atmospheric-pressure DBD;
- 4) Demonstrated covalent attachment of protein to PE nano-island patterns activated by DBD treatment;
- 5) Investigated covalent immobilization capability of ultra-thin hydrocarbon plasma polymer layers fabricated by magnetron sputtering;
- 6) Studied biological response of the protein-attached multifunctional surfaces in terms of adhesion, growth and differentiation of human osteoblast-like MG 63 cells.

The objectives 3) and 4) were performed in a collaboration with Prof. Pietro Favia and Fabio Palumbo as a part of my short-term scientific mission to the University of Bari, Italy.

2. EXPERIMENTAL

2.1. Experimental apparatus, facilities and specimens

In this work, experimental facilities were utilized for deposition of PE films, deposition hydrocarbon (CH) plasma polymers and treatment of polymer surfaces with low-temperature plasma at atmospheric pressure. First two approaches were done at the Department of Macromolecular Physics. The last one was carried out in the laboratory at the University of Bari, Italy.

Technical details of the experimental methods will be described at the beginning of this chapter. Further, diagnostic and characterization techniques will be described. The last section report methods and materials used for studies that involved protein or cells.

2.1.1. Vapor phase deposition

Vapor Phase Deposition of PE was performed in a vacuum chamber of 0.04 m³ volume. The side view cross-section of the experimental setup is included in Figure 8. The cylindrical chamber was connected to the rotary and diffusion pumps and the base pressure was 10⁻³ Pa. After evacuating to the base pressure, argon (purity 99.99%) was let into the chamber at a 5 sccm flow rate and the working pressure was set at 1 Pa.

Solid PE granules (~5 mm diameter, Sigma-Aldrich) were loaded into a copper crucible and covered with copper filings to prevent uncontrollable spitting. The electrically heated crucible rested on two molybdenum stripes and was brought to a temperature of about 300 °C by electric current. At this temperature, PE depolymerized and low molar mass fragments were released into a gas phase. The temperature of the substrates was examined by a thermocouple and was under 30 °C.

PE was deposited on polished silicon wafers. Silicon substrates were ultrasonically cleaned in acetone, ethanol and distilled water prior to deposition. After the cleaning, the substrates were mounted on a substrate holder and were introduced to the vacuum chamber via a load-lock system. The substrates were residing in the load-lock chamber until the experimental parameters (Ar pressure and flow rate, PE evaporation rate) were tuned and stabilized. The apparatus setup

allowed to organize load-lock configuration in a way to move the substrate holder either horizontally (right-left) and vertically (down-up). Majority of Vapor Phase Deposition (VPD) experiments were performed with the horizontal movement of the substrate holder and with vertical distance between the crucible and substrates fixed at 10 cm. After the deposition, the samples were extracted from the evaporation zone back to the load-lock chamber.

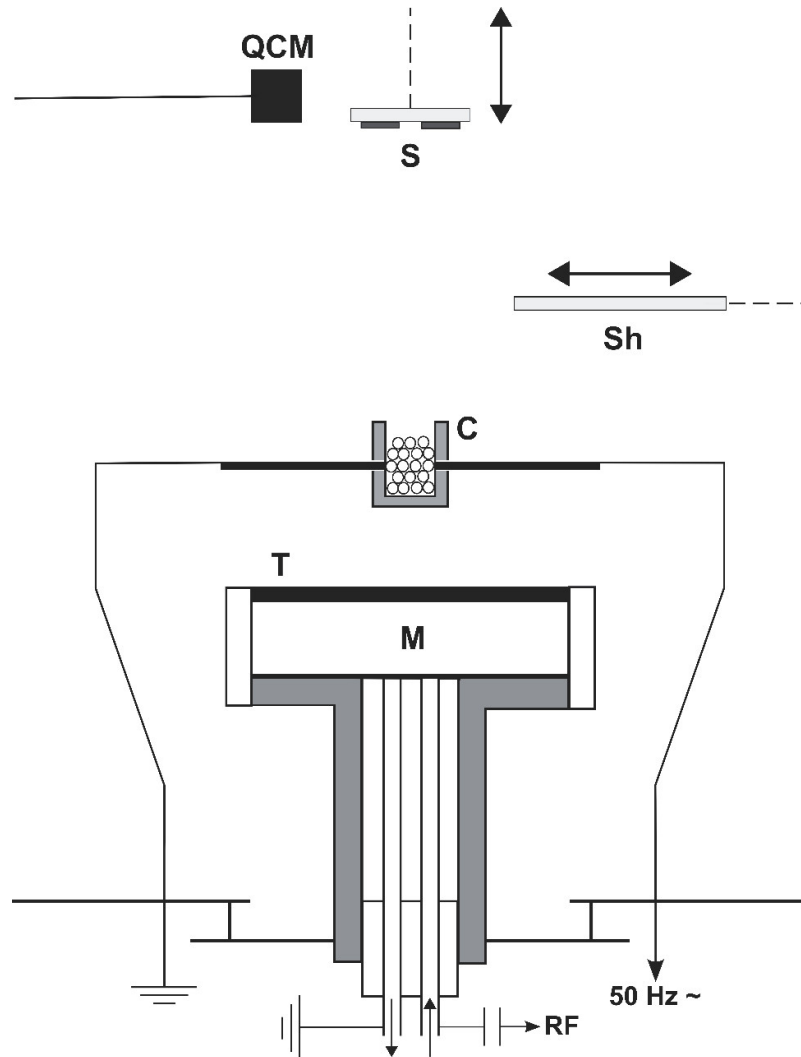


Figure 8. The schematic view of experimental set-up used for VPD of PE and magnetron sputtering. C – copper crucible loaded with granules of PE, QCM – quartz crystal microbalance, M – water-cooled planar RF magnetron, T – circular graphite target, Sh – shutter, S – silicon substrates on substrate holder).

The deposition rate was observed by QCM placed in plane with the substrates 10 cm above the crucible. At preliminary calibration experiment, PE films were deposited over silicon substrate at fixed rate and their thickness was measured ellipsometrically afterwards. It was found that the 20 Hz/min QCM frequency shift corresponded to the deposition rate of 11 nm/min.

2.1.2. Low pressure plasma activation

A series of Si wafers with or without PE nanopattern were used as substrates for further deposition of hydrocarbon plasma polymer overcoats. The experiments were performed in the same reactor.

A planar magnetron with water-cooling was situated 5 cm under the copper crucible. The magnetron was equipped with a graphite target 75 mm in diameter. RF power of 50 W was delivered to the magnetron by an rf generator (Dressler Ceasar 13.56 MHz) through a matching unit. The processing time was 30 seconds. As a result, an ultra-thin carbonaceous layer (further referred to as a CH overlayer) was deposited on the samples replicating the topography of the treated surface. Immediately after the treatment, the specimens were removed from the working zone via the load-lock chamber to the atmosphere.

2.1.3. Atmospheric pressure dielectric barrier discharge activation

Atmospheric pressure plasma dielectric barrier discharge was employed to activate the nanostructures prepared by VPD of PE. The experiments were conducted during a short-term scientific mission at the University of Bari (Bari, Italy). Silicon wafers (1×1 cm) with various PE film thickness were fabricated at the Charles University. These samples were used in the research work with AP DBD.

The DBD reactor consisted of two parallel plate silver electrodes, 1.3 mm apart, both covered with alumina sheets (Figure 9 A, B). The plates with the electrodes were confined within a poly(methyl methacrylate) (Plexiglas) chamber. For the treatment process, the working gas (either argon or helium) was injected into the chamber through an electronic mass flow controller (MKS instruments, see Figure 9 C). The total flow rate was kept constant at 5 slm. Before and after running

the process, the system was purged with the working gas for 5min. The discharge was ignited using an AC power supply. A high-voltage (P6015A, Tektronix) and a resistance type current probes, both connected to an oscilloscope (TDS 20145C, Tektronix, see Figure 9 C), were utilized for determination of the voltage and the current delivered to the system. The applied high AC voltage was kept between 4.68 and 5.20 kV_{pp} (peak-to-peak voltage) and frequency 23.2 kHz. From oscillograms, value of power density (the average discharge power divided by the electrode surface area) was determined to be 0.35-0.45 W·cm⁻². The average power was calculated by multiplying the energy per voltage cycle by the frequency. The energy per cycle was calculated from the time integral of the current times the voltage in one cycle.

Silicon substrates were positioned at the middle of the electrode. The exposure time was adjusted to treat different PE surfaces.

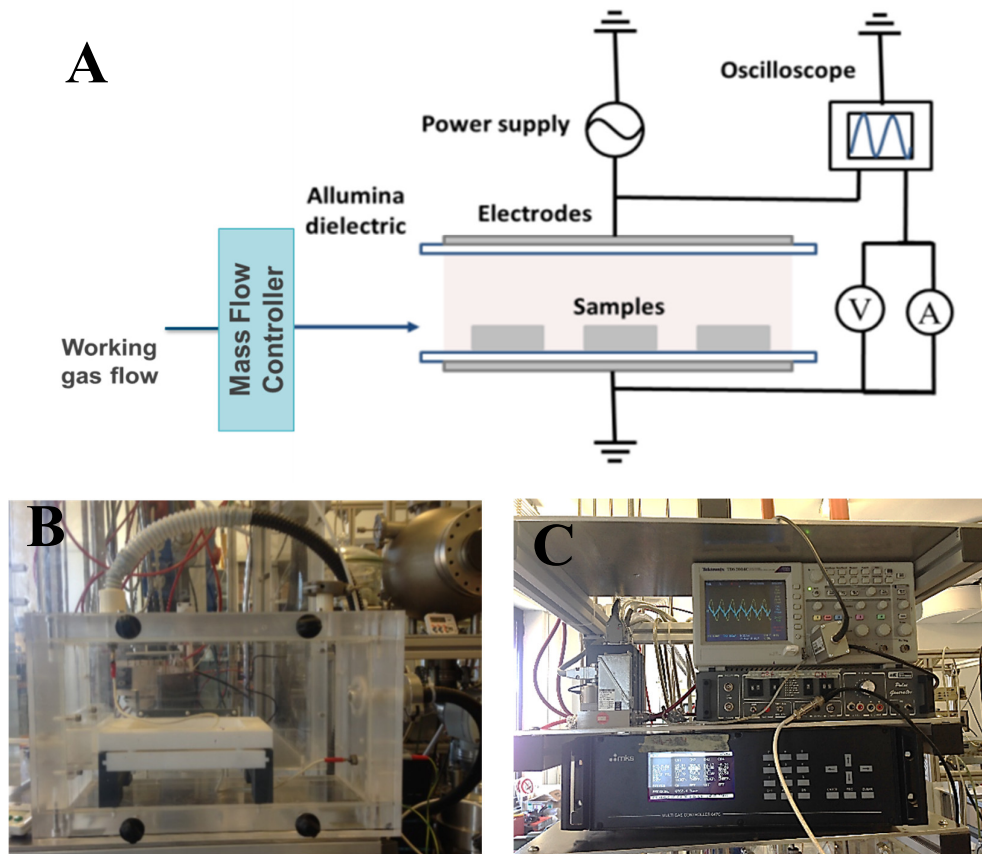


Figure 9. (A) Schematics of the AP DBD with designated key components. Adopted with permission from [147]. Real-life views of (B) the working chamber with electrodes and (C) electronics for measuring gas flow and plasma parameters.

2.2. Methods of sample characterization

2.2.1. X-ray photoelectron spectroscopy (XPS)

XPS was utilized to determine the chemical composition of the specimens. Analysis was performed with a XPS spectrometer equipped with a hemispherical analyzer (Phoibos 100, Specs, Germany) and a line delay detector with nine channels. XPS spectra were recorded at constant take-off angle of 90° using Al K α X-rays source (1486.6 eV, Specs) operated at 200 W. Survey spectra captured binding energies in the range of 0 - 1100eV at a pass energy of 40 eV (dwell time 100 ms, step 0.5 eV). High-resolution spectra were acquired at pass energy of 10 eV with 10 scans (dwell time 100 ms, step 0.05 eV).

Data were processed using CasaXPS software. The charge compensation was done by offsetting the binding energy relative to the hydrocarbon component (C-H) of the C1s spectrum at 285.0 eV. Furthermore, Shirley background was chosen for curve fitting. Results of XPS characterization were reproduced with accuracy of 15%.

2.2.2. Nuclear magnetic resonance spectroscopy (NMR)

The structural conformation and chemical environment of the PE film were investigated by NMR. Solid-state ¹³C Cross Polarization Magic Angle Spinning (CP/MAS) measurements were performed using an NMR Bruker Avance 500 spectrometer operating at 500.1 MHz. The MAS frequency was 10 kHz, recycle delay 5 s; 2000 spectra were accumulated. The contact time was set to 1 ms. The spectra were externally referenced to the signal of the carbonyl carbon of glycine. In addition, bulk PE (Sigma Aldrich) was measured as well.

NMR technique required relatively large amount (> 1 mg) of the sample. To achieve this goal, VPD of PE was carried out on a bigger 20×20 cm glass substrate. The substrate was 10 cm above the crucible and deposition rate was set to 20 Hz/min. After the deposition, the film was scraped off the glass with a razor blade into NMR rotor.

2.2.3. Sessile droplet method for wettability measurements

The wettability of samples was determined using a custom-built goniometer via a sessile water drop method. In this method, high-resolution camera observed 20 μl water droplets placed at three different positions on the specimen surface. The standard deviation of the wettability analysis was estimated to be 2%.

In the section 3.2 Dielectric barrier discharge activation of PE nano-pattern for covalent immobilization of biomolecules, the wettability was measured with a commercial goniometer equipped with a charge-coupled device camera (CAM 2008, KSV Instruments) in the laboratory at the University of Bari. Procedure of contact angle measurements (error $\pm 4\%$) included static, advancing, and receding mode [148].

2.2.4. Ellipsometry

Ellipsometry was used as a contact free tool for determination of the thickness of fabricated films. The measurements were performed using a spectroscopic ellipsometer (Wollam M-2000DI). The data were fitted using an effective-medium theory Cauchy model. Each sample was measured in three different locations and the mean value of thickness was taken.

2.2.5. Fourier transform infrared spectroscopy (FTIR)

Infrared measurements were carried out using a Bruker Equinox 55 FTIR spectrophotometer in a reflectance-absorbance mode. For this case, samples were fabricated on the gold-coated silicon substrates. The pure gold-coated silicon wafers served as a reference. FTIR spectra were recorded in the range of 400-4000 cm^{-1} (400 scans). The resolution was set at 2 cm^{-1} . FTIR spectra manipulation, i.e. background subtraction, were performed with the Opus 4.0 software (BRUKER Optics).

2.2.6. Gel permeation chromatography (GPC)

GPC measurements were performed with a PL-GPC 220 chromatograph apparatus equipped with a PL-220DRI refractive index detector, columns 3×PL gel 10 μm MIXED-B, 300×7.5 mm, with guard column PL gel 10 μm MIXED-B, 50×7.5 mm. The sample solutions were prepared in filtered 1,2,4-trichlorobenzene for chromatography (Scharlau) containing 0,025 wt% of an antioxidant Santonox R to prevent oxidative degradation of polymers. The GPC analysis was performed at 160 °C. The columns were calibrated with poly(styrene) standards (Waters a Polymer Laboratories).

2.2.7. Atomic force microscopy

The topography of the deposited samples was analyzed by atomic force microscopy. The ex-situ analysis was performed on an Ntegra Prima (NT-MDT) machine in a semi-contact mode under ambient air conditions. The AFM device was equipped with a soft silicon cantilevers (NSG03, NT-MDT, typical spring constant $k=1.7$ N/m, typical radius of curvature $r=10$ nm). The AFM images were obtained with 256×256 points resolution. The image processing was done using Image Analysis software (NT-MDT, 3.5.0.2069 release).

2.2.8. Calculation of scaled island size distribution

Image Analysis software provided island size distribution by analyzing AFM images. The steps to achieve scaled island distribution are highlighted below.

- 1) Exclude boundary islands from the AFM image (5x5 μm).
- 2) Take 10 AFM images (5x5 μm) of the same sample for better statistics.
- 3) Calculate the coverage θ and mean island size A . For example, there were found 1252 islands per 250 μm^2 (per 10 AFM images, each with 25 μm^2 area). The total area occupied by islands was 53 μm^2 , which gave the coverage $\theta=53/250=0.21$. The average island size was $S=0.04$ μm^2 .
- 4) Build a histogram of areas a with the bin interval of b μm^2 .

- 5) To get the area distribution density N_a in μm^{-4} , divide the above distribution counts N by the bin interval b and by the total analyzed area ($250 \mu\text{m}^2$).
- 6) Rescale the axis by multiplying on constants: $N_a \rightarrow N_a A^2 / \Theta$ and $a \rightarrow a/A$. The integral over the scaled function should yield 1.

2.2.9. Data processing for analysis of capture zone distributions

By a capture zone, one understands a zone around the island where diffusing molecule will be incorporated into the island with high probability. Frequently, a convenient way to approximate capture zones on a plane is to use Voronoi tessellations. Voronoi diagram is a set of Voronoi cells that represent regions of a plane whose points are closest to the center of mass of the islands than to any other point.

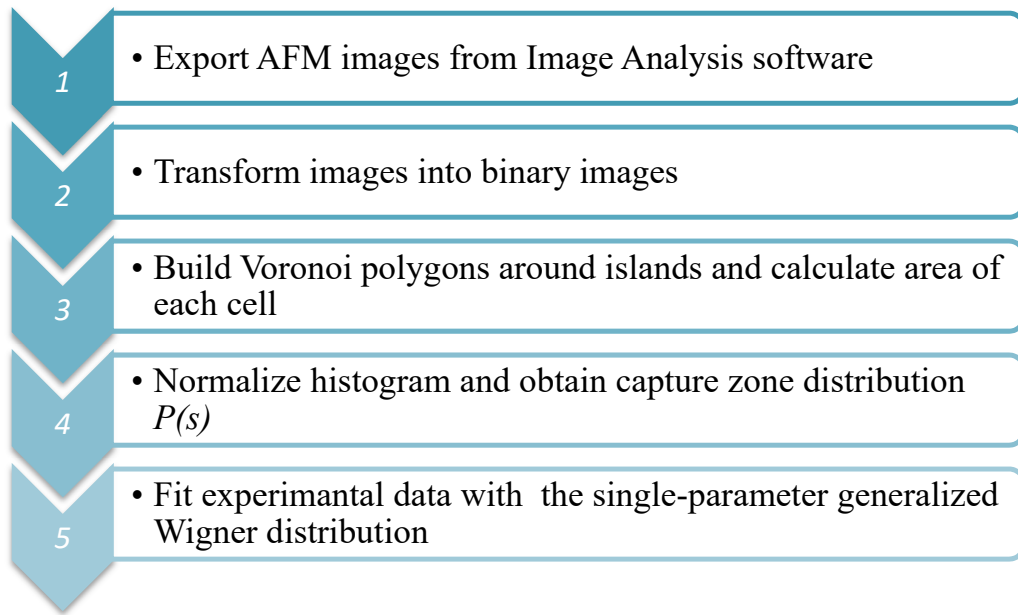


Figure 10. Diagram illustrating steps in the data processing of CZD analysis of PE islands on silicon.

A procedure to obtain CZD from AFM images is presented in Figure 10. Five AFM images ($5 \times 5 \mu\text{m}$) of each sample were exported from Image Analysis software and were cropped to the size of 757×757 pixels. ImageJ software [149] was used to execute binarization of images. As an output, binary images with white islands on

black background are obtained. After this point, all operations were performed using the Wolfram Mathematica (ver. 10.4) script developed by the author (see Attachment 1 and 2). Voronoi polygons were built around the islands with the *DistanceTransform* function. This function transforms the images so that the value of each pixel is replaced by its distance to the nearest boundary pixel. If we imagine situation of two neighboring islands we find the maximum intensity of *DistanceTransform* at the line, which is equidistant to each of the islands. *WatershedComponents* function performed the digitalization and allowed calculating individual cell areas. Function *DeleteBorderComponents* was applied to rule out capture zones located on the image edge.

The next step was calculating the function $P(s)$, which is normalized to unity, with unit mean. We omit the discussion of the code from Attachment 1. Instead, the general idea of such normalization is presented. Let us call $N(x)$ the raw histogram. We first compute the integral A of $N(x)$

$$A = \int N(x)dx \quad (10)$$

and define

$$M(x) = N(x)/A \quad (11)$$

Since $M(x)$ is normalized to unity, we can use it as a probability distribution and define the mean

$$\langle x \rangle \equiv B = \int xM(x)dx \quad (12)$$

Let us now define

$$s = x/\langle x \rangle = x/B \quad (13)$$

Therefore,

$$x = sB \quad (14)$$

and with (12) and (14)

$$1 = \frac{1}{B} \int (sB)M(sB)d(sB) = \int s[BM(sB)]ds \quad (15)$$

Defining from (14) and (14)

$$P(s) = BM(sB) = \frac{B}{A}N(x) \quad (16)$$

yields function normalized to unity with unit average

$$\int P(s)ds = \int BM(x)d\left(\frac{x}{B}\right) = 1 \quad (17)$$

and

$$\int \left(\frac{x}{B}\right) BM(x)d\left(\frac{x}{B}\right) = 1 \quad (18)$$

Finally, the nonlinear model based on generalized Wigner distribution (8) was used to fit the function $P(s)$ and described CZD.

2.3. Biological tests

2.3.1. Attachment of proteins

Bovine serum albumin (BSA) was purchased from Sigma Aldrich. Human recombinant tropoelastin (TE) was provided through the courtesy of prof. A. Weiss from the Sydney University. Solutions of both BSA and TE were produced in-house as described in Ref. [150]. BSA and TE were diluted to the 50 $\mu\text{g/ml}$ concentration in phosphate buffered saline (PBS, Sigma Aldrich) or deionized water at 25 $^{\circ}\text{C}$. Samples on silicon were placed to the 24-well plate (TPP, Switzerland; internal well diameter 15.4 mm).

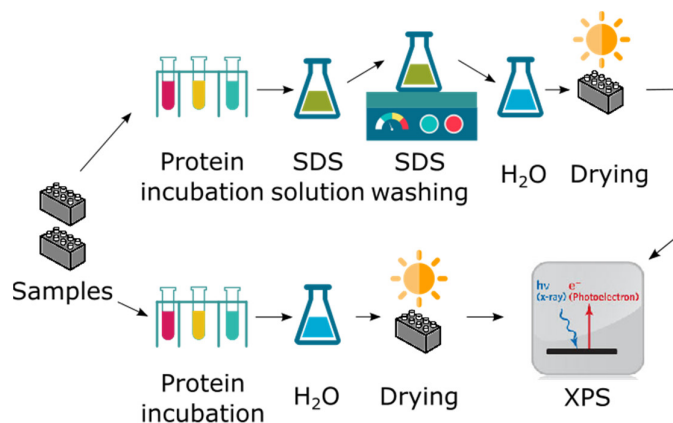


Figure 11. Schematic diagram of detection of protein attachment.

Amount of covalently immobilized biomolecules was examined by means of resistance to SDS (Sigma–Aldrich) elution. The SDS is capable to disrupt non-covalent bonds of physically adsorbed molecules. Thus, only proteins strongly bound to the surface can endure the SDS washing. A schematic diagram (Figure 11) shows the procedure sequence. Samples were incubated in 0.5 ml protein solution for periods selected for the research. For studies on AP DBD treatment of polymer film,

24 hours incubation time was used. Research aimed to control cell behavior employed various incubation times. After the expiration of the incubation time, the protein solution was removed. Duplicates of the samples were then immediately washed in a 3% SDS solution in distilled water for 1 h at 80 °C to remove all physisorbed proteins from the surface while keeping those attached covalently according to [119]. After the SDS washing, the samples were rinsed three times (10 min each) with 2 ml of distilled water. Our approach to detect a presence of protein on polymer surface was based on noticeable difference in the elemental structure of protein and PE: large biomolecules contain nitrogen within polypeptide backbone and in amino acid residues whereas PE does not. The surface-immobilized proteins were assessed by measuring the XPS N 1s signal before and after SDS washing to determine the proportion of the protein immobilized covalently. All the samples were dried prior to the XPS measurements.

2.3.2. Cell seeding and culture conditions

For the cell culture experiments, two sets of specimens were prepared: CH overlayer on a flat silicon substrate and CH overlayer on the pattern of PE islands. Both were sterilized in 70% ethanol overnight followed by washing procedure with sterile PBS. One- half of each set of the samples was incubated in the 50 µg/ml tropoelastin solution in PBS for 65 h while the second half remained untreated. As the next step, the samples were rinsed with pure PBS and inserted into the standard tissue culture plastic (TCP) cell culture dishes. Then they were seeded with human osteoblast-like MG-63 osteosarcoma cells (European Collection of Cell Cultures, Salisbury, UK) and suspended in Dulbecco's modified Eagle's Minimum Essential Medium (DMEM; Sigma, USA, Cat. No. D5648) with 10% fetal bovine serum (FBS; Sebak GmbH, Aidenbach, Germany) and gentamicin (40 µg/ml, LEK, Ljubljana, Slovenia). Each well contained 20,000 cells (i.e., approximately 10,700 cells/cm²) and 2 ml of the medium. The cells were cultured for 1, 2, 3 and 4 days at 37°C in a humidified air atmosphere containing 5% CO₂. Three samples were used for each experimental group and time interval. Untreated standard polystyrene wells (TPP, Switzerland) were used as controls.

2.3.3. Evaluation of the cell number

On day 1 after seeding, the samples were rinsed with PBS, fixed with 70% frozen ethanol (room temperature, 20 min) and stained with a combination of the fluorescent dyes Texas Red C2-maleimide, which stains proteins of the cell membrane and cytoplasm (Molecular Probes, Invitrogen, USA, Cat. No. T6008; 20 ng/ml in PBS) and Hoechst #33258, which stains the cell nuclei (Sigma–Aldrich, USA; 5 µg/ml in PBS). Both dyes were applied for 2 h at room temperature. The number of cells and their shape on the material surface were evaluated on microphotographs taken under an IX 51 microscope, equipped with a DP 70 Digital Camera (both from Olympus, Japan, objective 20 ×). On days 2, 3 and 4, samples were treated in the same way as on day 1 after seeding, except for staining solely with Hoechst #33258.

2.3.4. Measurement of the cell adhesion area

Cells stained with the membrane dye Texas Red C2-maleimide and the nuclear dye Hoechst #33258 on day 1 after seeding were also used for measuring their spreading area on microphotographs. The size of the area projected on the material was measured using Atlas Software (Tescan, Brno, Czech Republic). Cells that developed intercellular contacts were excluded from the evaluation. For each experimental group, three independent samples (containing 282–542 cells in total) were evaluated.

2.3.5. Statistical analysis

The quantitative data were calculated as mean ± standard error of mean (SEM) from triplicates. The statistical analyses were performed using SigmaStat (Jandel Corporation, USA). The multiple comparison procedures were carried out by the ANOVA, Student–Newman–Keuls Method. A value of $p \leq 0.05$ was considered significant.

3. RESULTS AND DISCUSSION

3.1. Growth of PE islands fabricated by vapor phase deposition

This chapter discusses phenomena of self-organization of PE oligomers on silicon surface and describes the process in terms of several growth theories.

3.1.1. Chemical composition

Whenever a new coating is developed, a question of chemical composition arises. Deposition methods, such as OMBD, occur under ultra-high vacuum with well-controlled chemistry of incoming particles. However, such deposition methods are limited in a choice of precursor and do not allow working with polymers. To fabricate a polymer film, conventional VPD can be adopted that involves thermal fragmentation of polymer backbone, transport of vaporized oligomers in vacuum and condensation on the substrate. VPD of PE results in the deposition of hydrocarbon coatings on silicon substrates.

XPS demonstrates elemental composition of the resultant film. Survey spectrum of PE on silicon consists of a single carbon peak (Figure 12) which is symmetric and typical for PE (high-resolution C 1s spectra is depicted in the inset). The peak is centered at 285.0 eV and attributed to aliphatic carbon.

The FTIR spectrum of the vapor phase deposited PE is shown in Figure 13 and it confirms the hydrocarbon character of the deposited film. The methylene groups reveal themselves across the entire absorption region. The characteristic peaks at 2918 and 2851 cm^{-1} are assigned to the asymmetrical (larger wavelength) and symmetrical (smaller wavelength) stretching vibrations of CH_2 . The deformational vibrations of CH_2 are apparent through the peaks at 1463 cm^{-1} (scissoring), 1377 cm^{-1} (wagging) and 910 cm^{-1} (scissoring). The peak at 1641 cm^{-1} can be assigned to the C = C bonds formed in a small amount as a result of radical disproportionation during thermal degradation of PE [151].

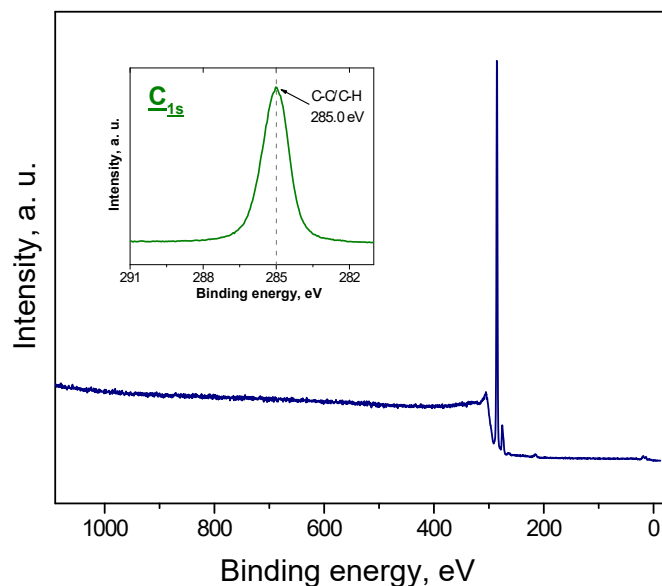


Figure 12. Survey XPS spectrum of PE film. In the inset, the high-resolution C1s spectrum is shown.

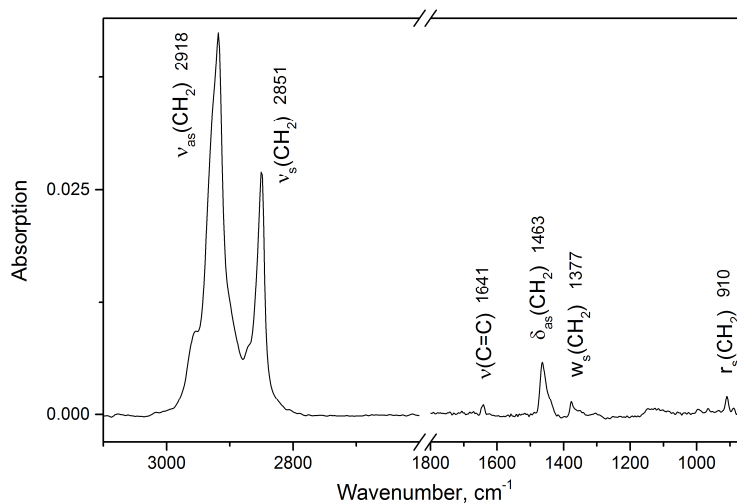


Figure 13. FTIR spectra of PE film produced by Vapor Phase Deposition.

Molecular mass distribution of the PE precursor and of the film prepared by vapor phase deposition of PE was analyzed by GPC and the results are compared in Figure 14. The broad black curve corresponds to the precursor with the number average molar mass $M_n = 19355$ g/mol. The mechanism of vacuum thermal degradation can be explained as random polymer backbone scission and release of low molar mass oligomers into the gas phase [151]. The blue curve in Figure 14

corresponds to the coating formed by VPD and it represents a prominent confirmation of this phenomena. Narrow and symmetric distribution of the PE oligomers is centered at $M_n = 1384$ g/mol. Our results are in accordance with the earlier report of Satou et al [63] who identified the molar mass of evaporated PE to be 1300 g/mol. The narrowness of mass distribution is reflected by the parameter of dispersity

$$D_m = M_w/M_n. \quad (19)$$

After the evaporation, dispersity drops drastically from the initial $D_m = 9.36$ (black curve) down to $D_m = 1.10$ (blue curve). Recalling the fact that the molar mass of the $-\text{CH}_2-$ monomeric unit is 14 g/mol, majority of incoming oligomers have approximately one hundred $-\text{CH}_2-$ groups and the general formula can be designated as $(-\text{CH}_2-)_{100}$. Further in the text, we will refer to this material as PE for simplicity, yet bearing in mind that it is composed of the mixture of oligomers with the average mass of $(-\text{CH}_2-)_{100}$ and dispersity of $D_m = 1.10$.

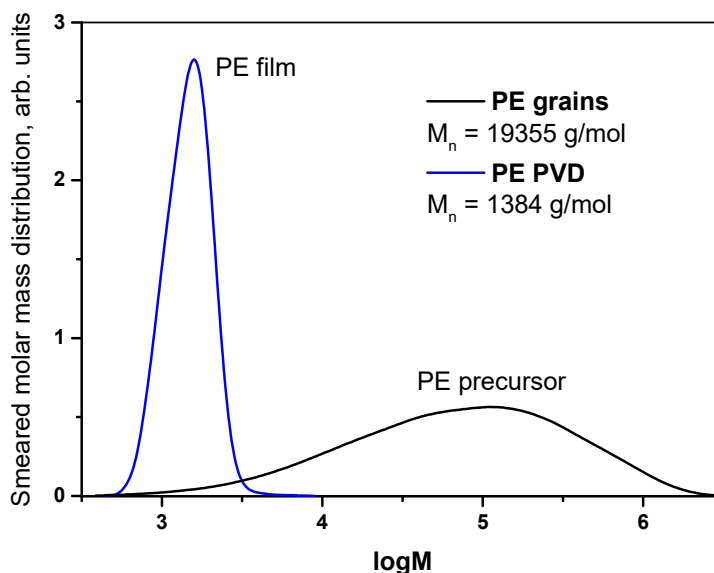


Figure 14. Molecular weight distributions of: PE precursor (black) and evaporated PE film (blue).

Overall, these results indicate the remarkable behavior of polyethylene when vacuum heating secures a source of oligomers with the very narrow size distribution.

The NMR analysis was used to determine macromolecular structure in the VPD-deposited PE film. According to the solid-state ^{13}C CP/MAS NMR spectrum (Figure 15), a strong peak at 32.4 ppm and a shoulder at 30.1 ppm are observed. These signals correspond to the crystalline and amorphous phases of methylene units, respectively [152]. The end groups of the chain, methyls, give signal at 14.6 ppm. The area ratio of the integrated intensities of signals from methylene units and methyls was used to calculate that for every $-\text{CH}_3$ group is presented 25 $-\text{CH}_2-$ groups in the PE chains. The region at 100-150 ppm (see inset in Figure 15) can be assigned to the unsaturated carbon in various $\text{C}=\text{C}$ configurations. Relative molar fraction of these peaks is less than one percent of the $-\text{CH}_2-$ groups. Taken together, NMR characterization determined semi-crystalline structure of predominantly linear PE chains.

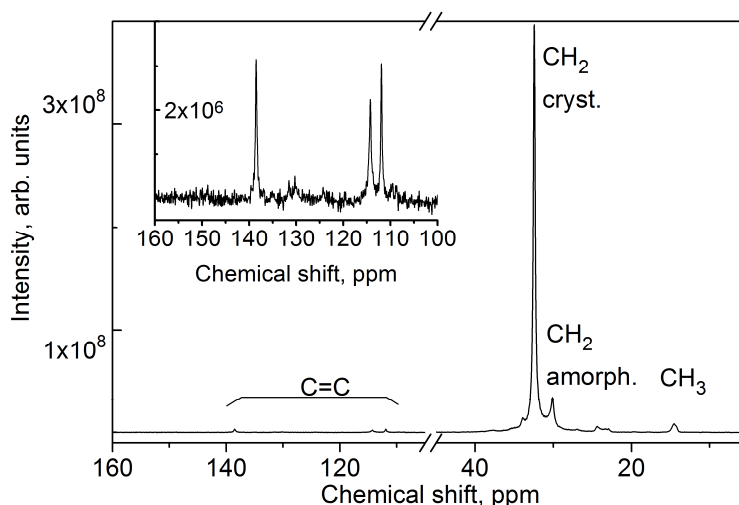


Figure 15. The ^{13}C CP/MAS NMR spectrum of the film prepared by vapor phase deposition of PE on Si. The inset illustrates in detail the region of the unsaturated carbon.

3.1.2. Island growth

The AFM analysis was performed on the PE samples prepared for different deposition time and it revealed that the initial stages of the film growth proceed with the formation of islands. Figure 16 provides a representative set of the AFM top view images from the very low up to almost a 100 % coverage θ . Thin film passes through

several distinctive intervals which are typical for island-type growth. Initially, numerous small seeds spread chaotically and mark foundations for islands. From $\theta = 0.1$, newly arriving oligomers cease to form new seeds but rather join to already existing nuclei and the system enters the aggregation regime which is characterized by the constant number of islands per unit area. The end of the regime at $\theta = 0.3$ is indicated by partial coalescence when macromolecular bridges connect isolated islands. As coverage increases to $\theta = 0.5$, the islands reach percolation. Before the layer completion, we observe ongoing (from $\theta = 0.7$) formation of features on top of the existing coating. In the final stage, topography changes to mounds due to rapid roughening.

The cross-section measurement reveals a notable aspect of the island morphology (Figure 17): the islands maintain their thickness at approximately 7-8 nm in the course of growing until θ reaches 0.7 and the second-layer features become numerable. The conserved height together with the flat top and steep wall slope make a unique appearance of the PE islands and allow considering them as 2D objects, at least below percolation. The 2D nature of the island growth is caused by effective surface diffusion and downward movement of oligomers landing on the top of the existing islands (small Ehrlich-Schwoebel barrier).

The next step of the research was to obtain a quantitative interpretation of the kinetics of the PE island growth at the silicon surface. AFM, being a powerful analytical tool, can effectively probe the morphology evolution and provide input data for analysis such as: the coverage, the island density, the island-size distribution, etc. Applying various growth theories to the data should help to establish detailed mechanisms involved in island-type self-organization of macromolecules.

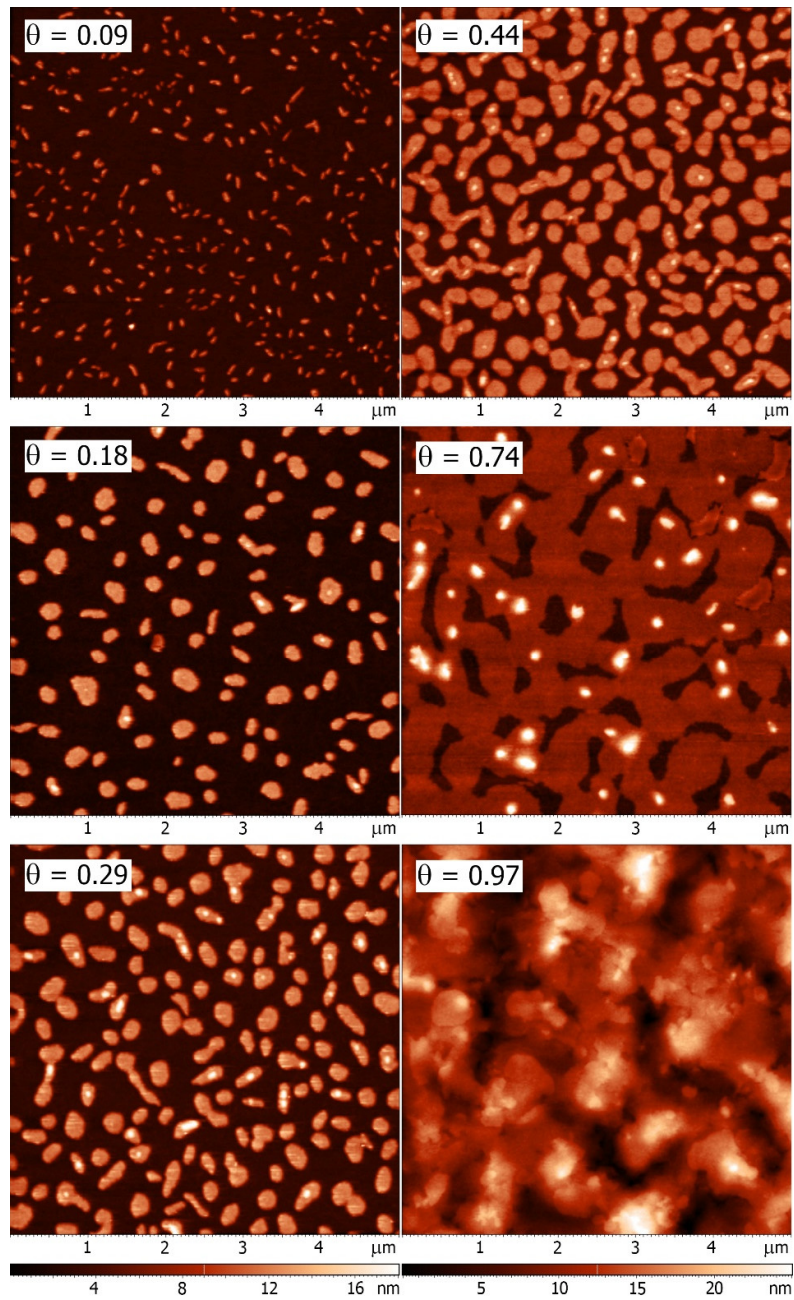


Figure 16. AFM top view images ($5 \mu\text{m} \times 5 \mu\text{m}$) of PE grown on silicon surfaces at room temperature, with several representative coverages in the range from 0.09 to 0.97.

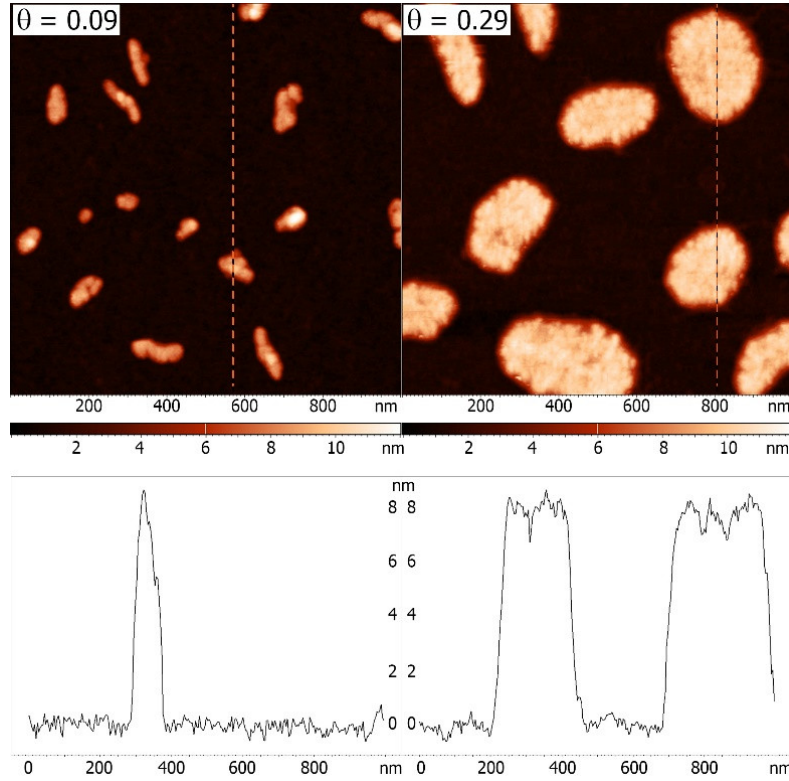


Figure 17. The height invariance of the PE islands grown by VPD deposition on Si as observed by AFM: height images (top) and cross-sections (bottom).

3.1.3. Rate equation theory

Presence of the distinguishable aggregation region allows application of the well-known inorganic film growth models for the analysis of the nucleation and growth of the PE islands. The oldest approach is based on kinetic “rate equations” which calculate interrelation between various elementary surface processes for island growth with the number of isolated particles moving on the substrate and islands of a given size. According to rate equations, the saturated island density N_{sat} in the aggregation regime for a rectangular lattice at constant temperature is a function of the deposition rate R [39]:

$$N_{sat} \sim R^\alpha, \quad (20)$$

where α is the exponent varying with growth modes and closely connected to the critical island size i . To ensure that the aggregation regime is fulfilled, the coverage was confined within the range between 0.1 and 0.3. Below this coverage, the film

grows in the nucleation regime where the island density still increases with coverage; above, the island density starts to decrease due to coalescence.

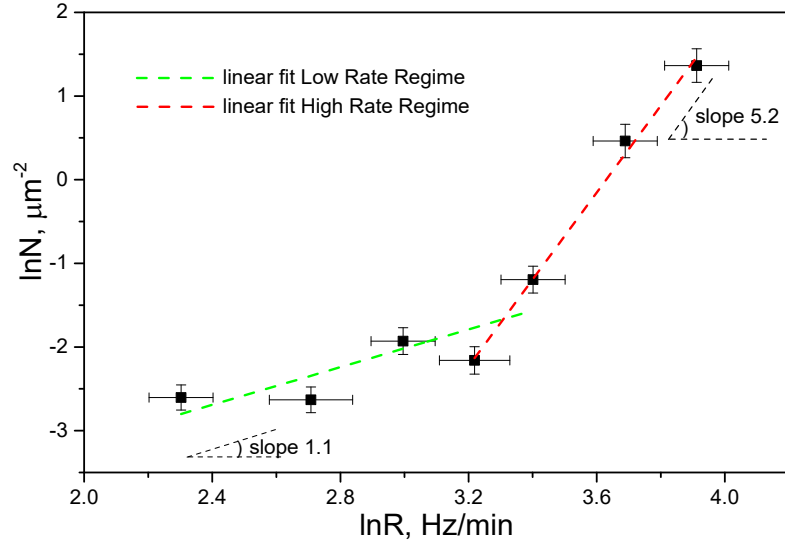


Figure 18. Dependence of saturated island density as a function of deposition rate² for PE on silicon at a substrate temperature of 25 °C.

In Figure 18, the plot of $\ln N_{sat}$ vs $\ln R$ is depicted. On the plot, the slope should correspond to the parameter α . In our case, data points are arranged in a way that two linear sections are seen. The crossover point is detected for $R = 25 - 30$ Hz/min. Let us designate a regime for smaller deposition rates as Low Deposition Rate Regime (LRR) and a regime for bigger deposition rates as High Deposition Rate Regime (HRR).

Linear fits for the two sections reveal the average values of exponent for lower deposition rates

$$\alpha_{LRR} = 1.1 \pm 0.1 \quad (21)$$

and for higher deposition rates

$$\alpha_{HRR} = 5.2 \pm 0.2 \quad (22)$$

² Deposition rate R was measured in terms of QCM frequency shift that corresponds to the increase of mass per unit area.

For diffusion mediated growth model, the exponent in the rate equation is [20]

$$\alpha = \frac{i}{i+2}, \quad (23)$$

with α approaching, but not exceeding, unity with increasing i . Apparently, the value of α_{LRR} is out of the range for diffusion-limited process for which the attachment probability is 100%.

A feasible explanation for this result may be identified in the works of Kandel [153] and, more recently, of Venables and Brune [154]. The researches have considered a scenario where the attachment of the incoming particle to the island is hindered by island edge barriers. As it was found above, the incoming PE oligomers consist of $(-\text{CH}_2-)_{100}$ chains. A distinctive feature of hydrocarbon chains is an ability to adapt themselves dynamically to changing physical interaction with the environment. Dynamic adaptation of hydrocarbon structure may involve mutual re-orientation between the approaching macromolecules and the macromolecules immobilized at the edge of the island. Impediment to join the island may result in the decrease of the sticking coefficient. Various simulations of sub-monolayer depositions with reducing sticking coefficients generated structures that approached the compact island shape [155]. On the contrary, the diffusion-limited aggregation (DLA) model gives rise to the fractal morphology. Visual inspection of the PE islands (Figure 16, Figure 17) confirms the compact shape of the aggregates and, hence, the assumption of non-unity attachment probability is validated. For nucleation described by attachment-limited aggregation (ALA), the slope of the $N = f(R)$ in log-log coordinates is expressed as [153]:

$$\alpha = \frac{2i}{i+3}, \quad (24)$$

where the value for α can vary between 0.5 (for $i = 1$) and 2 (for large i). From α_{LRR} , one extracts the critical island size in the range $i_{LRR} = 3.7 \pm 0.7$ for PE grown at incoming flux below 30 Hz/min.

While ALA describes the system at low incoming rate of molecules to substrate (LRR), the scenario with hindered attachment does not look applicable to the early stages of PE growth at elevated deposition rates. There is only a small amount of literature available concerning the nucleation of rodlike organic molecules on surfaces [16], [17], [34] and no sources discuss the high value of exponent $\alpha_{HRR} = 5.2 \pm 0.2$ as the one observed in Figure 18. The recent study by Morales-

Cifuentes et al. [156] offers the full rate-equation model for island nucleation and growth. The authors assume that incoming species consist of two categories: “hot” state adsorbates with high kinetic energy that propagate ballistically, and thermalized monomers that diffuse on the surface in a random-walk manner. For fast thermalization (low incoming flux), the DLA regime is fulfilled. For slow thermalization, a novel hot monomer aggregation (HMA) regime was found that turned out to be essentially non-thermal (no dependence on thermally activated processes) ALA. Between limiting DLA and HMA regimes, the researchers discovered six intermediate scaling regimes envisioning nonmonotonic crossover of i . Thus, the application of the “hot precursor” nucleation model to the dependence of island density vs deposition rate $N_{sat}(R)$ gives a single curve fit of a crossover for fixed i instead of linear sections with individual i values. Figure 19 illustrates this difference in nucleation mechanism on the recent organic-molecule deposition experiments [157] where the latter is in striking agreement with the data.

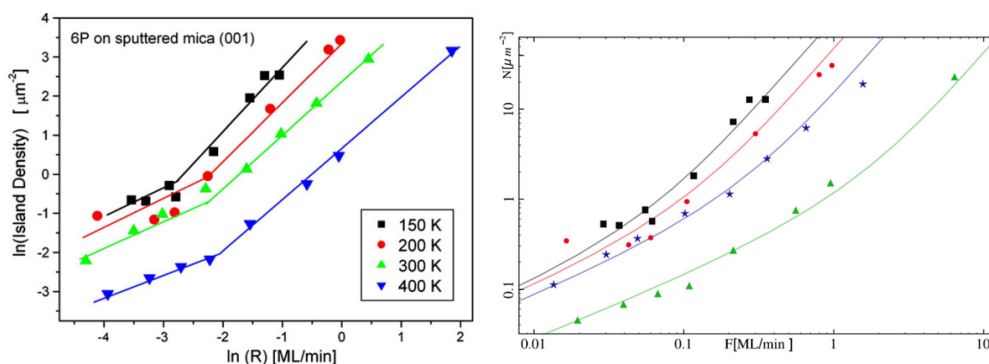


Figure 19. Island density vs deposition rate for hexaphenyl on sputter-modified mica at different temperatures. Left: the drawn lines change the slope and signal the two different regimes with different i [157]. Right: the best fit of experimental data by the novel “hot” precursor model with $i=4$ (adapted by removing insets from [156]).

A critical drawback of this work is that the developed theory has a complicated mathematical apparatus without well-defined analytical formulas. The shortcoming does not allow the independent experimental examination of the mechanism lying behind the growth of organic 2D nano-islands.

Overall, this chapter examined the growth mechanism of PE nanoislands by analyzing the saturated island density as a function of the deposition rate. The classic

rate equation theory described nucleation at low deposition rates as ALA with critical nucleus size $i_{LRR} = 3.7 \pm 0.7$, indicating that when 4-6 oligomers of PE are sufficient to form a stable island. With elevation of the deposition rate, the system appears to be more complicated and the mechanism of the island growth at HRR is yet to be elucidated. The following chapters elaborate the experimental data at low deposition rate when the nucleation mechanism seems to resemble the well-established inorganic models.

3.1.4. Dynamic scaling theory

In the section that follows, it will be argued that the DST accesses quantitative information of the 2D growth of PE on silicon prepared by VPD. A confirmative argument of the complete condensation (no re-evaporation from substrate) of PE growth at a small rate of incoming species was given in the previous chapter.

Information about island-size distributions was collected from the frequency-count analysis of the AFM images. Figure 20 plots the island-size statistics for five coverages (deposition times) within the aggregation mode $0.1 < \theta < 0.3$. The horizontal axis corresponds to the island area in μm^2 . On the vertical axis, the island size distribution density is expressed in μm^{-4} and it fulfils the sum rule $\int N_a da = N$ (N is the number of islands per unit area). For each coverage, the curve has a well-defined peak which corresponds to the average island size that increases with increasing coverage θ . Peculiar distribution shape for $\theta=0.09$ is suggested to origin from a bigger error in software processing of the small islands.

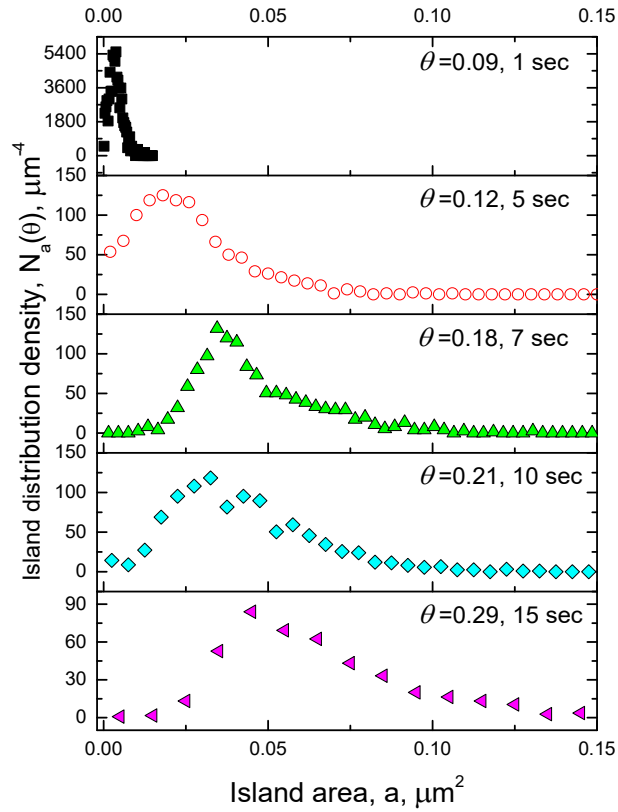


Figure 20. Island size distribution density $N_a(\theta)$ for various PE coverages in the range $0.09 < \theta < 0.29$ grown on silicon at room temperature.

The obtained distributions were further processed according to the scaling law (5) and the scaling plot of $\frac{N_a A^2}{\theta}$ vs a/A is shown in Figure 21. The symbols on the plot correspond to the data scaled from the island size histograms for six samples within the range $0.09 < \theta < 0.30$. There is a clear collapse of the data points into a single distribution. As it has been introduced above, the experimental curve $f(u)$ can be single-parametrized by critical island size i applying theoretical expression (6); hence, we simulated the scaled distribution for the critical sizes from $i=1$ to 3. When one fixes the parameter i , the best-fit parameters C_i and a_i cannot be arbitrary and must take into account the normalization assumption set by (7) to make the model physically correct. In the investigation of initial stages of organic para-hexaphenyl molecules growth, Potocar et al [49] constructed the universal function $f(u)$ with the required constraints on the parameters. The ultimate values of C_i , a_i and i are listed in the Table 2.

i	a_i	C_i
1	0.2715	1.1091
2	0.2976	1.9678
3	0.3086	3.2385

Table 2. A list of parameters a_i and C_i in Eq. (6), for $i = 1-3$ [49].

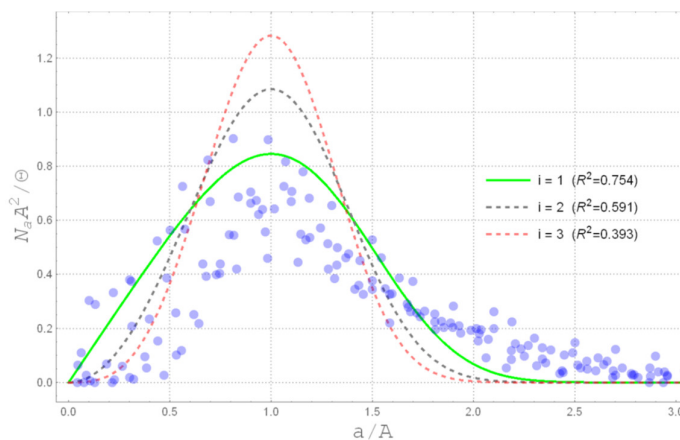


Figure 21. The scaled island size distribution density of PE islands on silicon in the aggregation regime (light blue circles). The best-fit simulation of the scaling function $f(u)$ for $i=1$ is indicated by solid green curve.

The simulated curves in Figure 21 are colored differently in dependence on the value of critical island size i : green for $i=1$, grey for $i=2$, red for $i=3$. The best fit with the coefficient of determination of $R^2=0.754$ was obtained for $i=1$. This implies that only two PE oligomers suffice to create a stable nucleus. Nonetheless, the absolute value of R^2 for the best-fitted model makes this interpretation questionable because of lack of the quantitative agreement between the experimental and the simulated data. The applied analytical model extends only for the DLA growth; and mismatch between the theory and the experiment indicates that the film formation kinetics of PE on silicon does not obey solely to diffusion-mediated behavior.

The general appropriateness of the DST as a method to gain insights about PE island growth was checked by collapsing the scaled island size distributions for different coverages into a single masterplot (Figure 21). To date, there is a DLA mechanism with derived analytical approximation to the universal scaling function.

Monte-Carlo simulations of the nucleation and growth of two-dimensional islands generate various structures. Selecting and adjusting input model allows to modify a shape of the scaled curve. Rastch et al [158] used a pair-bond solid-on-solid model and demonstrated that the island size distribution scaling function peak is higher when a quantity λ (the ratio of the dimer dissociation rate to the rate of adatom capture by dimers) increases.

Taken together, these results suggest that valid scaling assumption for surface growth of PE oligomers on silicon substrates should encourage theoretical work on establishing sophisticated models for long organic molecules growth to understand underlying mechanisms better.

3.1.5. Capture zone distributions

We now consider the distribution of capture zones of the PE islands on silicon in the aggregation regime. The use of CZD is advantageous over DST from several points of view. The lower resolution of morphology images is sufficient to obtain positions of center of masses; hence, capture zones. A function describing CZD achieves better fit for asymmetrical data³ than scaling relationship [48], [159]. One of the most powerful aspects of the analytical form of CZD is the ability to extract critical island size i without defining the aggregation mechanism in advance (more details are given below) [160].

To get a capture zone distribution, the first step is to identify individual meshes associated with each island. The Voronoi cells were constructed on the 5×5 μm height images for the same specimen discussed in the chapter before. To automatize the process (large amount of similar images), we coded a script in Wolfram Mathematica. Technical details can be found in the Experimental section. Here, we present an initial image (Figure 22A) and a final representative Voronoi tessellation calculated for the starting image (Figure 22B). It is important to note that boundary islands at the image edge were excluded from the analysis to reduce the statistical error.

³ PE islands partially coalesce even at small coverage and the large islands contribute to the shift of the symmetry of the size distributions.

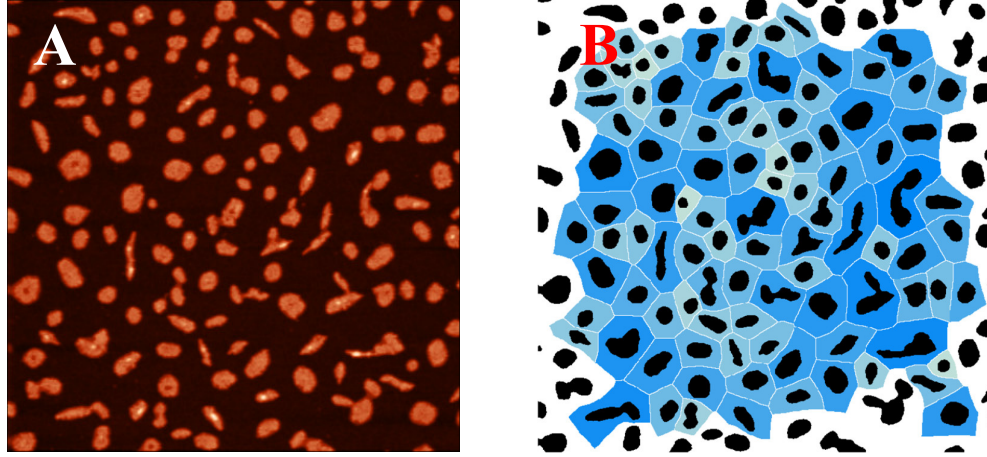


Figure 22. (A) AFM image ($5 \mu\text{m} \times 5 \mu\text{m}$) of nano-patterned PE islands on silicon ($\theta=0.18$) deposited at room temperature. Z-scale is 16 nm. (B) Corresponding Voronoi tessellation. Cell color intensity (azure hue) indicates relative mesh area value; bigger areas are represented by darker color. Islands without cells on the image edges were not included in area histogram.

The GWD was used to describe the CZD. Figure 23 provides the summary statistics of CZD for ensemble of five samples as the probability function $P_\beta(s)$ versus dimensionless area s . Through applying the Wigner surmise (8)

$$P_\beta(s) = a_\beta s^\beta \exp(-b_\beta s^2),$$

to our CZD measurements, we determined the free fit with highest value of R^2 of 0.989. All the values of the fitting parameters, along with their standard errors, are presented in Table 3. The corresponding parameter β in the GWD solution is:

$$\beta = 2.38 \pm 0.22. \quad (25)$$

	<i>Estimate</i>	<i>Standard error</i>
β	2.384	0.224
a_β	4.944	0.779
b_β	1.638	0.139

Table 3. A list of parameters in Eq. (8) simulating the best fit of experimental data.

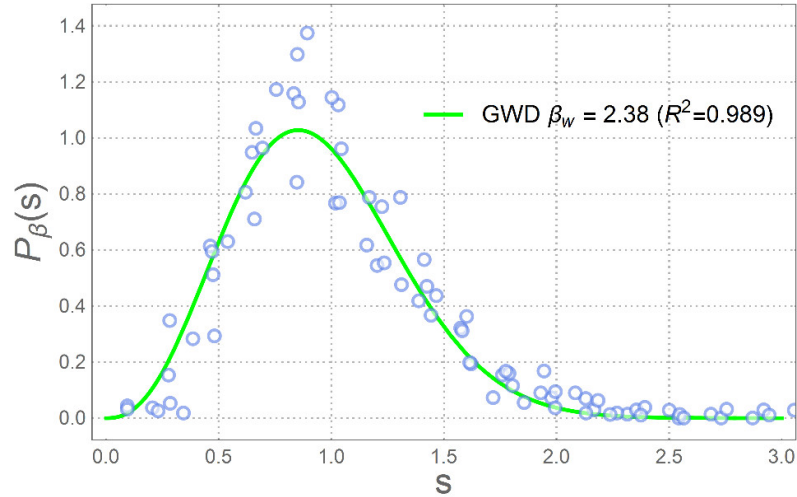


Figure 23. Capture-zone histogram obtained for the ensemble of PE islands on silicon at five different coverages in the aggregation regime. About 2100 capture-zone areas were analyzed. Capture-zone distributions for the biggest R^2 is marked with a thick green line.

Pimpinelli et al. [156] carried out the study of the island nucleation and proved that it is possible to obtain a material parameter of critical island size without *a priori* knowledge of aggregation-limiting process. Critical island size, in case of compact islands, can be calculated from the relationship:

$$\alpha \cdot \beta = i, \quad (26)$$

where α is the scaling exponent in (20) and β is the recently assigned fitting parameter of GWD in (8). As opposed to the DST with its analytical approximation derived solely for DLA, generalization (26) does not depend on the type of the aggregation regime and allows calculating critical island size for systems with unknown nucleation regime. Consequently, the proposed approach is a perfect match for the initial stages of PE growth on silicon where island formation mechanism was neither fully comprehended, nor predicted.

Combining ((25), (21)) \rightarrow (26) we extract a fundamental material parameter in physics of growing thin films – critical nucleus size:

$$i = 2.62 \pm 0.48. \quad (27)$$

Expression (27) indicates that either three or four PE oligomers form stable islands. The critical size is found to be at the lower limit of the range calculated by the rate equation approach (4-6 oligomers) when ALA was assumed.

Reportedly [161], the critical island size for metal film growth (individual atoms) is commonly equal to 1. The value of i calculated for the growth of rod-like pentacene (36 atoms in the molecule) on silicon dioxide was three [39], [162], [163]. The analysis of nucleation of spherical fullerene C₆₀ (60 atoms in the molecule) found that the critical nucleus size was between 0 and 1, i.e. oligomers/dimers are stable islands [164]. Direct comparison of our data with the critical island size published for organic molecular film growth should be taken with reserve for several reasons. Due to the wealth of conformations and configurations in organic chemistry, every organic molecule is a unique structure with its own set of physical interactions. Secondly, scientists tend to use ready solutions for film growth modelling without confirming validity of the solution in their particular case due to complexity of tailored work.

The main goal of the current study was to determine the critical island size of the PE oligomers by utilization of the existing models including the approach that does not require any presumption of the nucleation mechanism. From the GWD approximation of CZD and from the slope of the saturated island density as a function of the deposition rate, we found that for room temperature the stable nucleus is formed by three or four PE oligomers.

To the best of our knowledge, the nucleation phenomena of PE macromolecules at the vacuum/solid interface have never been investigated quantitatively so far. Considering above-mentioned information, the growth of PE islands on silicon manifests new and interesting phenomena of self-assembly on solid surfaces. Further experiments with extended organic macromolecules, supported by computational methods, will explain more physical aspects of the film formation and improve manufacture process for applications.

3.2. Dielectric barrier discharge activation of PE nano-pattern for covalent immobilization of biomolecules

Patterned surfaces with designed features at micro- and nanometer scales are important components of biosensor devices [126]. To make a device robust and stand out constant contact with liquids, strong covalent immobilization of proteins and peptides on surfaces is required [113], [165]. This part of the thesis aims at

developing a simple model platform for biosensing that includes both: polymeric nano-pattern with controllable morphology and covalently attached protein. The preparation of the polymeric nano-pattern was achieved by deposition of PE nano-islands as it was described in the previous chapter. The nano-pattern was subsequently activated by an atmospheric pressure DBD to create covalent linkages with BSA.

The unique nature of PE oligomers self-assembling on silicon provides ready-to-use two-dimensional polymeric islands. The islands may be fabricated to be of different lateral size but with constant thickness of 7-8 nm. PE coatings consist of uncross-linked linear $(\text{CH}_2)_{100}$ macromolecules and needs to be modified to generate free radicals for subsequent binding of proteins. Our research is focused on the surface activation by atmospheric-pressure DBD that combines the advantages of non-equilibrium plasma with the relative ease of atmospheric-pressure operation [128].

The aim of this chapter was to demonstrate the feasibility of the spot selective attachment of BSA to PE nano-islands because of DBD treatment in atmospheric pressure of non-depositing gas.

3.2.1. Types of PE nano-patterns for plasma activation

Formation of the 2D island pattern from the vacuum deposited $(\text{CH}_2)_{100}$ oligomers offers various possibilities for their use as nanostructured platforms. However, chemical inertness of saturated hydrocarbons limits the areas of their applicability. Therefore, surface activation is required to overcome this shortcoming.

Three types of the samples were modified by atmospheric pressure DBD: the PE nano-islands with the different surface coverage of 8% and 32%, and the continuous PE film with the thickness of 95 nm for comparison. The surface morphology was studied by AFM (Figure 24).

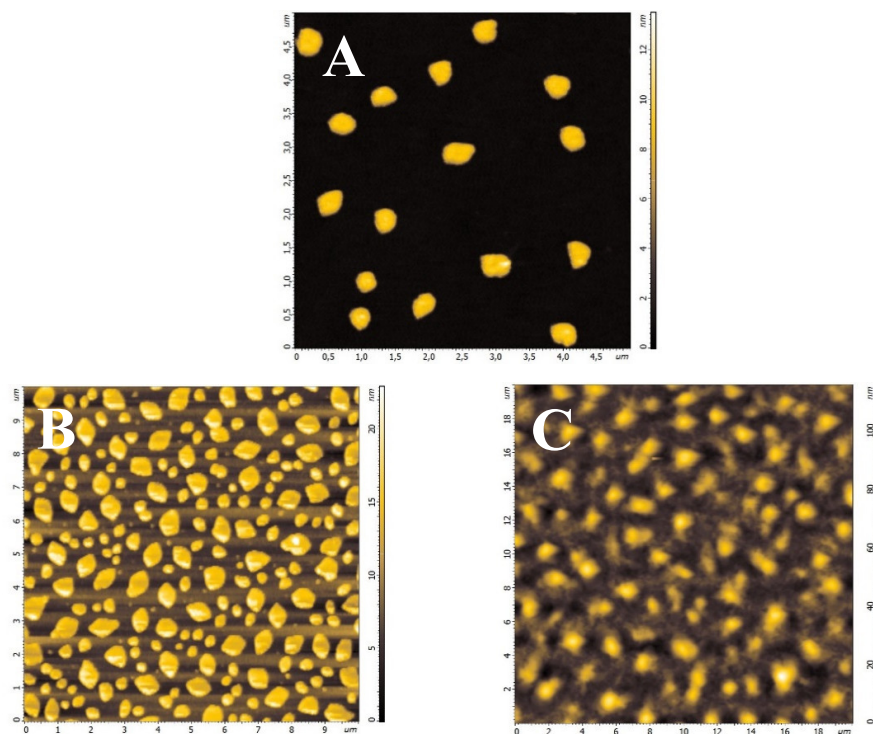


Figure 24. AFM images of pristine coatings prepared by vapor phase deposition of PE on Si. The deposition times determine the amount of the polymer on the surface: (A) 1 second deposition results in the island pattern with coverage of 8%, (B) 10 seconds - in the island pattern with coverage of 32% and (C) 10 minutes - in 95 nm thin film.

Two typical surfaces patterned with PE islands are displayed in Figure 24A and B. Latter figures represent irregular patterns of two-dimensional islands with different mean size and inter-island spacing. The nano-structured samples were characterized by two numbers: island coverage and mean island size. The smaller islands of $0.083 \pm 0.014 \mu\text{m}^2$ mean size occupy 8% whereas the larger $0.157 \pm 0.107 \mu\text{m}^2$ islands cover 32% of the silicon substrate. The thin PE film in Figure 24C reveals the mounded surface structure; the root mean square (RMS) roughness of the film was 14.6 nm if measured over $20 \times 20 \mu\text{m}^2$ area. We contrasted the surface morphologies to demonstrate the correlation of amount of immobilized protein with the available spot area for the protein attachment.

3.2.2. DBD plasma modification of continuous PE film

The samples were treated by DBD plasma to activate the surface. Two types of working gases (argon, helium) and various treatment times were used to modify the surface properties. The discharge was generated using a high voltage AC source operating at 23.2 kHz, the applied voltage was kept between 4.68 and 5.20 kV_{pp} (peak-to-peak voltage). Under these parameters, the plasma was mostly uniform; however, the presence of microdischarges was inevitable.

The effect of the plasma treatment was readily observed as darkening of the treated samples. The darker color points at carbonization of the surface and it intensified with the exposure time. The samples were characterized by water contact angle (WCA), ellipsometry, AFM, and X-Ray photoelectron spectroscopy.

3.2.2.1. Surface roughness and morphology

Treatment of polymers with non-depositing plasmas is usually associated with the changes of morphology and roughness of the surface [166]. Argon and helium plasmas are known to induce ablation processes in polymers including cleavage of the macromolecular chains and removal of low molecular weight fragments from the surface. Figure 25A shows the ellipsometric measurements of the thickness of the PE film after it has been Ar and He plasma treated for different periods of time. The initial thickness of the PE layer was 95 nm and it is evident that the thickness reduction depends on the gas type and the plasma exposure time. The helium plasma treatment revealed noticeable etching after 30 seconds while the argon plasma treatment demonstrated the detectable change only after 1 min of operation. An overall etching of the PE film with helium DBD was found to be more efficient and the rough estimate of the etching rate gives 12 nm·min⁻¹. The etching rate for argon DBD was 7.5 nm·min⁻¹.

Plasma etching is surface-related phenomena and it directly influences the morphology of modified polymer. For quantification of the surface roughness, the Root-Mean-Square (RMS) value of the surface height fluctuations is often used. Using the AFM technique, we examined the surface morphology of the PE film before and after the helium and argon plasma treatment. Highly mounded pristine PE

film is shown on Figure 25C. The RMS roughness values obtained for 20×20 μm areas are plotted in Figure 25B. Decaying with time development of the RMS roughness is observed for both gases. Previous research into the effect of plasma modification on RMS roughness of ultra-high-molecular-weight PE (UHMWPE) found the decrease of the surface roughness for Ar, He, dry air and N₂ [167]. A reason for the smoothing effect of the plasma etching may be related with the redeposition of ablated low molar mass fragments [168]. Fraction of the ablated species, instead of moving away from the substrate, returns back to the polymeric surface and contributes to the decrease in roughness.

Figure 25E-F give series of AFM images representing the morphology of the PE film treated in argon DBD for 3min, 10 min and treated in helium DBD for 3 min, respectively. Morphological changes of plasma treated specimens were more profound when helium was used as the working gas. For example, 3-minute plasma modification in helium produced smoother surface than it was achieved by 10 min exposure to the argon discharge.

Thus, the plasma treatment led to dramatic changes in the surface morphology due to ablation of the PE surface layer so that the RMS roughness declined with exposure time. In the light of final application of plasma for activation of nano-islands, it can be concluded that PE film is more resistant to the treatment by argon plasma

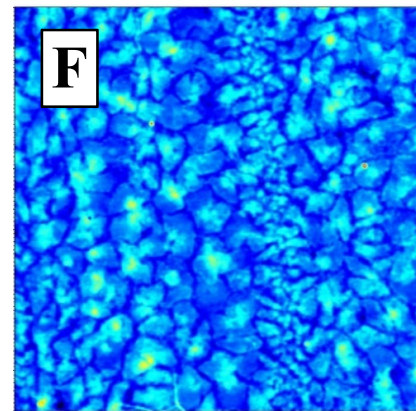
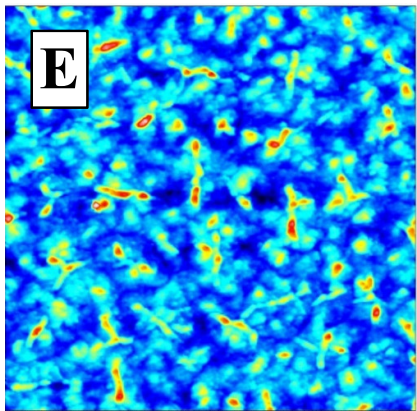
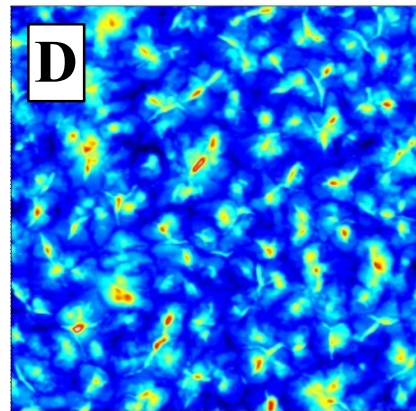
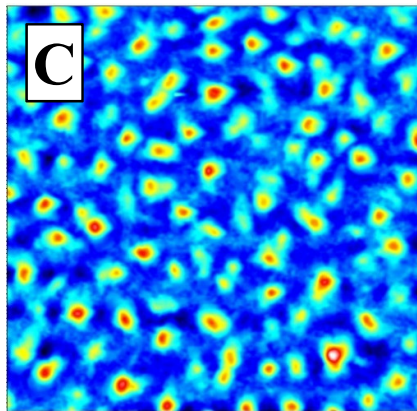
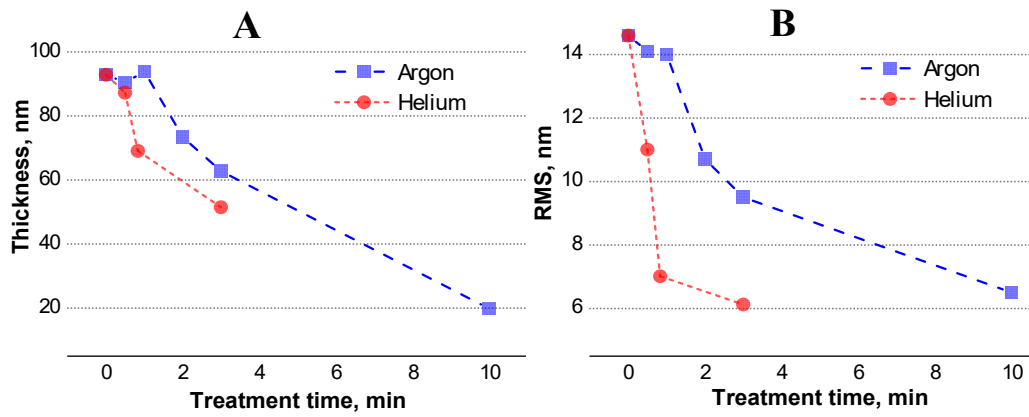


Figure 25. (A) Dependence of the PE film thickness on the exposure time in argon and helium plasmas. (B) Dependence of the surface roughness of the PE film on the exposure time in argon and helium plasmas determined by AFM. AFM images of the untreated PE film (C), the PE surface after the argon plasma treatment for 3 min (D)

and 10 min (E); PE surface after helium plasma treatment for 3 min (F). AFM image size: 20 μm ; z-scale: 115, 95, 52 and 98 nm.

3.2.2.2. Surface chemistry

XPS was used to determine the elemental composition of the untreated and plasma-modified PE films. The relative content of oxygen, carbon, silicon and nitrogen is illustrated in Figure 26. The XPS wide spectrum of the untreated sample revealed 97% of C but, in addition, approximately 1% of Si and 2% of O. High surface roughness may explain the presence of signals from silicon and oxygen coming from the substrate in the valley areas where the local film thickness may happen to be very small. Low-level oxidation of the PE film may also contribute to the detected oxygen content.

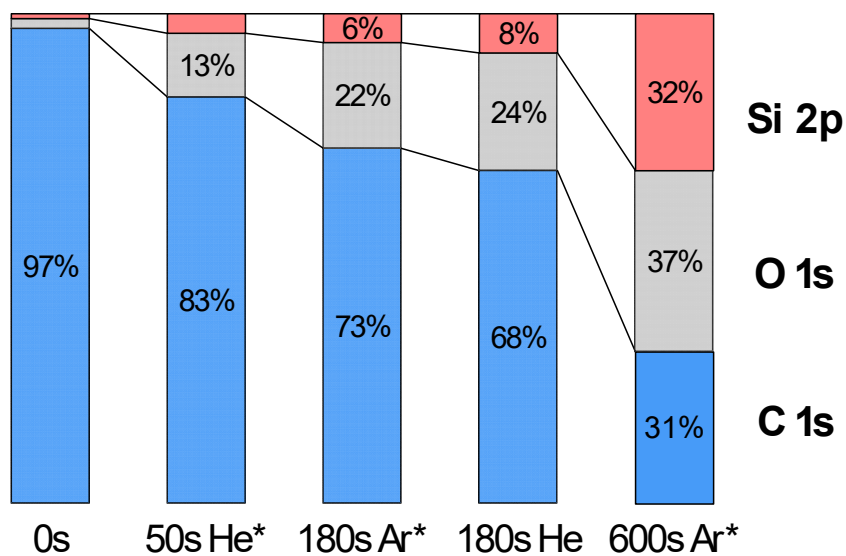


Figure 26. Changes of elemental composition obtained from XPS spectra for a series of PE films after various treatment time by argon or helium DBD. Asterisks indicate <0.5% presence of N in the spectra.

The concentration of oxygen and silicon increases after the plasma treatment. As it was mentioned in the previous chapter, the DBD discharge leads to polymer film ablation and it reduces the film thickness. This results in the increase of the signal from underlying native silicon oxide. Furthermore, the macromolecular bond

cleavage leads to the formation of radicals that react readily with atmospheric oxygen after the treatment procedure. The post-treatment chemical changes induced by the radical interaction with the ambient atmosphere are also manifested by the small increase of the nitrogen content in the films.

The high-resolution C1s XPS spectra were investigated to evaluate which functional groups are formed on the polymer surfaces by the plasma treatment. The comparison of the C1s peaks is given in Figure 27 for the untreated and for the 600 s argon plasma treated PE sample. The C1s spectrum of the untreated PE sample (Figure 27A) is dominated by the peak at 285.0 eV which corresponds to aliphatic carbon. The small contribution from the peak at 286.5 eV can be attributed to the presence of oxidized carbon species. In contrast, the spectrum of the plasma-modified film (Table 4) appear broadened and it reflects the higher level of the oxidation. The curve fit in Figure 27B differentiates the peaks for O-C-O/C=O at 287.7 eV and for O-C=O at 289.1 eV. Formation of these species is caused by radical-initiated oxidation reactions with atmosphere oxygen [169].

Thus, the DBD plasma treatment of the PE film proves to be an effective tool for the surface modification. The formation of radicals leads to the post-treatment oxidation of the surface. This can be of use for subsequent binding of biomolecules, as it will be discussed in the following chapter.

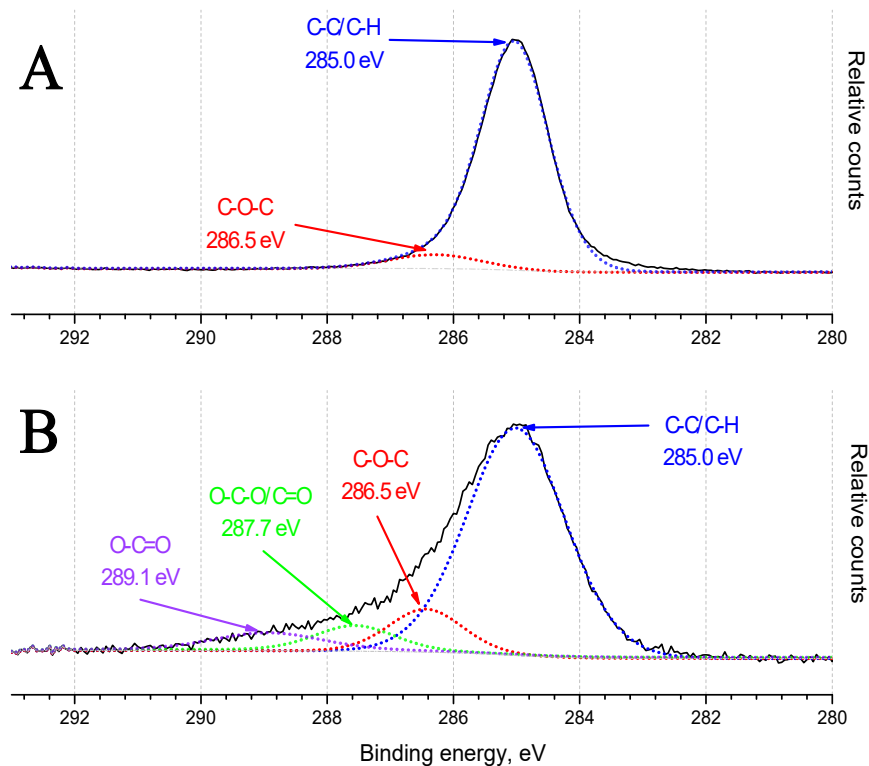


Figure 27. XPS high-resolution C 1s spectra recorded on (A) untreated PE thin film surface and (B) after 600 s plasma treatment with argon. The condition of the discharge were $V_{pp} = 5.2$ kV, $d = 2$ mm, frequency = 23.2 kHz.

Treatment time /Gas	C1s curve fit, at. %			
	C-C/C-H	C-O-C	O-C-O/C=O	C-O=C
Untreated	92.0	8.0	0	0
180 sec/Argon	78.2	8.0	9.8	4.0
600 sec/Argon	76.5	10.8	6.6	6.1
180 sec /Helium	85.8	5.1	5.7	3.4

Table 4. Concentration of chemicals groups in PE film plasma treated under different experimental conditions as detected from the C 1s XPS.

3.2.2.3. Wettability analysis

The wettability of the modified coatings was evaluated before and immediately after the treatment.

Figure 28A gives an overview of the change in the static WCA of the thin PE film treated with Ar and He plasma as a function of the treatment time. The untreated PE film exhibits the static WCA of $107.7 \pm 4.3^\circ$. For both gases, the static WCA decreases with the treatment time, the decrease being more pronounced for He. For instance, 3-minute He plasma exposure leads to the static WCA of $25.0 \pm 1.0^\circ$, while for the equivalent period in argon plasma the static WCA dropped to $57.7 \pm 2.3^\circ$. Remarkably, super-hydrophilic state (immeasurably small WCA) was achieved after 10 min of the argon plasma treatment.

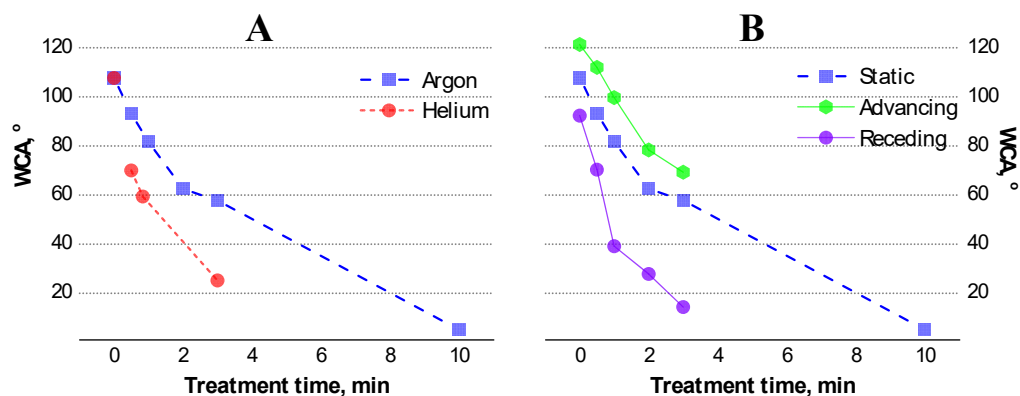


Figure 28. Evolution of (A) static WCA of argon and helium-treated PE thin films in dependence on DBD treatment time. Variation of (B) static, advancing and receding WCA of PE surface with argon DBD treatment time.

The drop in the contact angle is related to changes of the chemical composition and the topography of the surface [170]. From Figure 28B it is obvious that a difference between advancing and receding WCA (WCA hysteresis) grows steadily with the treatment time. The hysteresis on solid surfaces emerges in presence of surface roughness and chemical heterogeneity [171], [172]. Hence, in the case of PE, the longer argon DBD surface modification leads to the development of more profound surface heterogeneity.

3.2.3. Immobilization of BSA on DBD activated PE films

Before studying covalent attachment of biomolecules to nano-structured PE, continuous PE thin films were tested, the effect of the DBD on which was discussed in the previous chapters. The plasma treatment of the PE films for covalent attachment of biomolecules was carried out using argon atmospheric pressure DBD. Argon was selected because of the less destructive etching of PE and because of its lower cost.

Immobilization of proteins on radical-rich surfaces directly from solutions takes place in two stages. Firstly, a protein molecule randomly diffuses in the solution until it reaches the polymer surface and become physisorbed, usually by weak van der Waals forces. If radicals are present at the surface, they may participate in covalent binding of adsorbed proteins via the opening of carbonyl bonds of polypeptide chains or via the reactions with the functional groups of the amino acid residues. Nevertheless, the exact mechanism still remains unclear. The surface radicals consumed in these reactions can be replenished by radicals diffusing from the polymer bulk.

Four types of samples were analyzed for the ability to bind BSA: the continuous 95 nm PE films untreated and treated by plasma for 3 min, and nano-structured PE films with 32% and 8% coverage, both treated for 15 seconds. The level of adsorbed BSA was measured by XPS after the samples were incubated in 50 $\mu\text{g/mL}$ BSA solution and rinsed twice with de-ionized water. In accordance with XPS wide spectra, the average content of nitrogen for all the samples was 11% (column A on Figure 29) and it points at the similar amount of the protein accumulated on the surface. To remove the loosely bound proteins, an additional washing cycle with SDS was applied as it is described in the Experimental section. The sample coated with the continuous film retained 3.6% of N (column B on Figure 29), nano-patterns with 32% (column C on Figure 29) and 8% (column D on Figure 29) coverage demonstrated 1.8% and 1.4% of N, correspondingly. The samples untreated with plasma and processed with SDS showed no presence of nitrogen (column E on Figure 29). Treatment time of nano-islands was shortened to 5 seconds to avoid destruction effect of atmospheric pressure discharge on the islands. The detected

decrease of nitrogen signal with area covered by PE seems to be a reasonable evidence of our ability to bind protein in a spot-selective manner. By controlling the polymer coverage, we determine the amount of protein that can be immobilized since only treated polymer regions participate in radical-based capturing of biomolecules from solution.

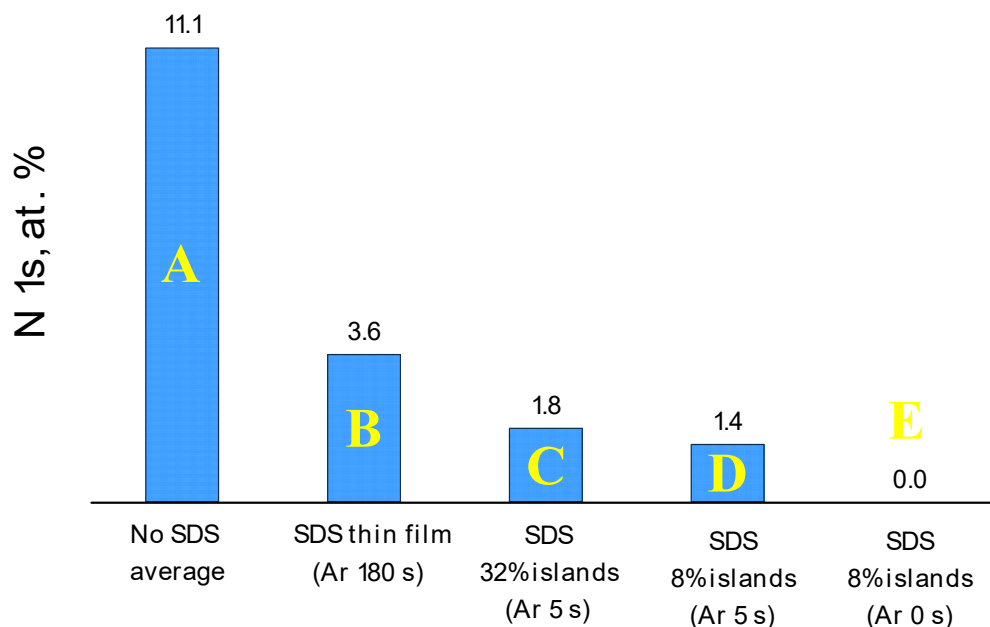


Figure 29. The level of residual nitrogen calculated from XPS survey spectra. All samples were immersed into 50 $\mu\text{g/ml}$ BSA solution in PBS for 24 h. (A) All the samples show the same level of the BSA adsorption immediately after the incubation and without the SDS washing. After the SDS processing, the samples show different amount of the protein left bound on the surface: (B) continuous PE thin film plasma treated for 180 s, (C) PE nano-islands with 32% coverage plasma treated for 5 s, (D) PE nano-islands with 8% coverage plasma treated for 5 s and (E) PE nano-islands with 8% coverage without the preliminary exposure to the discharge.

The AFM analysis performed on the PE nanoislands grafted with the protein shows significant changes of the surface morphology. The compact islands with constant thickness of 7-8 nm transform into the mounded objects (Figure 30A). Without the protein incubation, topography of the islands was fully preserved (Figure

30C) after the SDS washing. This fact confirms that changes in the surface morphology in Figure 30 correspond to protein agglomerates immobilized on top of the islands. Indeed, the height profile of a single mounded object reveals a symmetrical protein “hill” that reaches 35 nm in height (Figure 30B), and the underlying 7-nm thick plateau corresponding to the PE island. The dimensions of an albumin molecule diluted in distilled water are determined as 140×40×40 angstrom [173]. It implies that the agglomerate height is about double of the biggest albumin dimension.

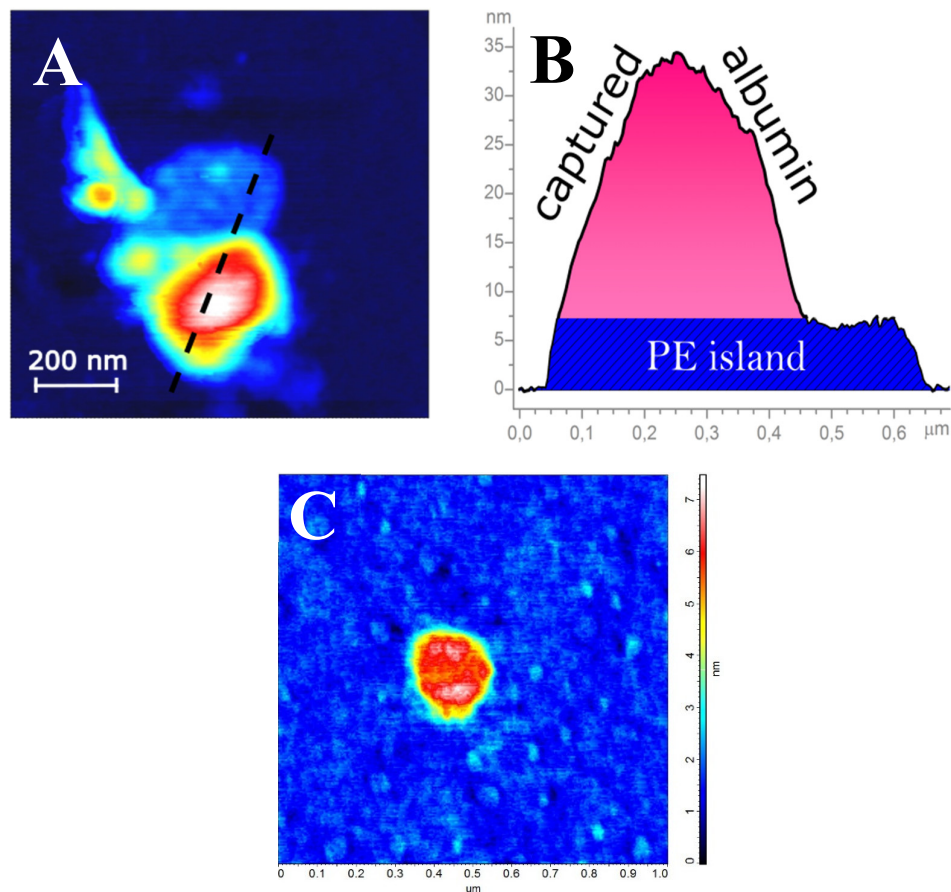


Figure 30. (A) The AFM height image of the PE nano-island treated with argon plasma for 5 seconds, incubated in 50 μg/mL BSA solution in water for 24 hours and rigorously washed in 3% SDS solution at 80 °C for 1 hour. (B) Corresponding cross-section indicated by the black line going across the PE island (blue) and the protein hill (pink). (C) The morphology of the island processed with the 5-second plasma treatment and SDS washing.

Thus, it can be concluded that the modification of ultra-thin island-type PE films by argon DBD enabled the formation of radicals that act as linkers in interaction with biomolecules. The treated PE samples immobilized BSA from solution and rigorous washing protocol did not remove the protein from the surface. The level of nitrogen detected by XPS after SDS washing, corresponding to the amount of the immobilized protein, was higher for the samples with larger island coverage, which proved the spot-selective role of the PE nano-islands. Therefore, PE nano-pattern in combination with plasma-based surface engineering technology has proved to have a great potential for various biomedical devices.

3.3. Control of osteoblast-like cell adhesion using a PE nano-pattern

The previous chapter examined protein immobilization on PE surfaces treated by atmospheric pressure DBD. The plasma modification was efficient for the activation of the PE nano-pattern that can be used for spot-selective strong attachment of biomolecules directly from the solution. The plasma treatment of compact nano-islands was found to fabricate a reliable biosensing platform, where the surface density of the nano-islands and strength of the protein attachment determine the device performance.

This chapter will focus on the surface topography as a factor in regulating cell adhesion and proliferation. An additional factor to promote the surface biocompatibility is anchoring of extracellular matrix (ECM) protein onto it. We will test a single step approach for covalent immobilization of proteins through CH plasma polymer layers. The following chapter will address the last research objectives aimed to:

- 1) Investigate covalent immobilization capability of ultra-thin hydrocarbon plasma polymer layers fabricated by magnetron sputtering;
- 2) Study biological response of the protein-attached multifunctional surfaces in terms of adhesion, growth and differentiation of human osteoblast-like MG 63 cells.

The chapter begins by looking briefly at fabricated surfaces. The next step will be to examine adsorption of proteins to surfaces, in particular, production of

covalently bound protein overlayer. The influence of the morphology and ECM protein overlayer on MG-63 cells will be presented. Cell tests will include temporal evolution of the number of cells and spreading area measurements.

3.3.1. Films analysis

It is known that cell/surface interaction depends strongly both on the surface chemistry and on the surface morphology. In many cases, cell adhesion was studied on micro-rough or multi-scale rough surfaces, although it has been acknowledged that roughness at nanoscale may have its peculiar influence [91], [93], [174], [175]. As it was shown above, the VPD of PE on Si results in the formation of the nano-island pattern with very specific morphology that can be controlled by the experimental conditions such as the deposition time and the rate. Subsequent plasma treatment leads to the creation of the surface that binds proteins in a manner selectively controlled by the surface pattern: proteins attach covalently to radical-rich islands whereas uncovered Si substrate immobilizes them only by weaker physisorption. Since the protein adsorption always precedes the cell adhesion, the resultant platform is attractive and can be used for the analysis of the nano-morphology-mediated cell adhesion capability. In this case, however, spatial chemical heterogeneity should be avoided in order to analyze the influence of the surface morphology itself. The deposition of an ultra-thin coating of plasma polymer over the nano-island pattern may offer the solution to this problem.

For this study, 2D pattern of PE nanoislands was designed to occupy 25% (Figure 31 type I) of the total surface of the substrate (Figure 31 type S). The statistical analysis of the surface revealed the mean island area of $1.8 \pm 1.4 \mu\text{m}^2$ and the average nearest neighbor distance of $2.2 \pm 0.8 \mu\text{m}^2$. The RMS roughness of the sample was $3.20 \pm 0.04 \text{ nm}$ as compared to $0.20 \pm 0.02 \text{ nm}$ for the flat silicon substrate (Figure 31 type S).

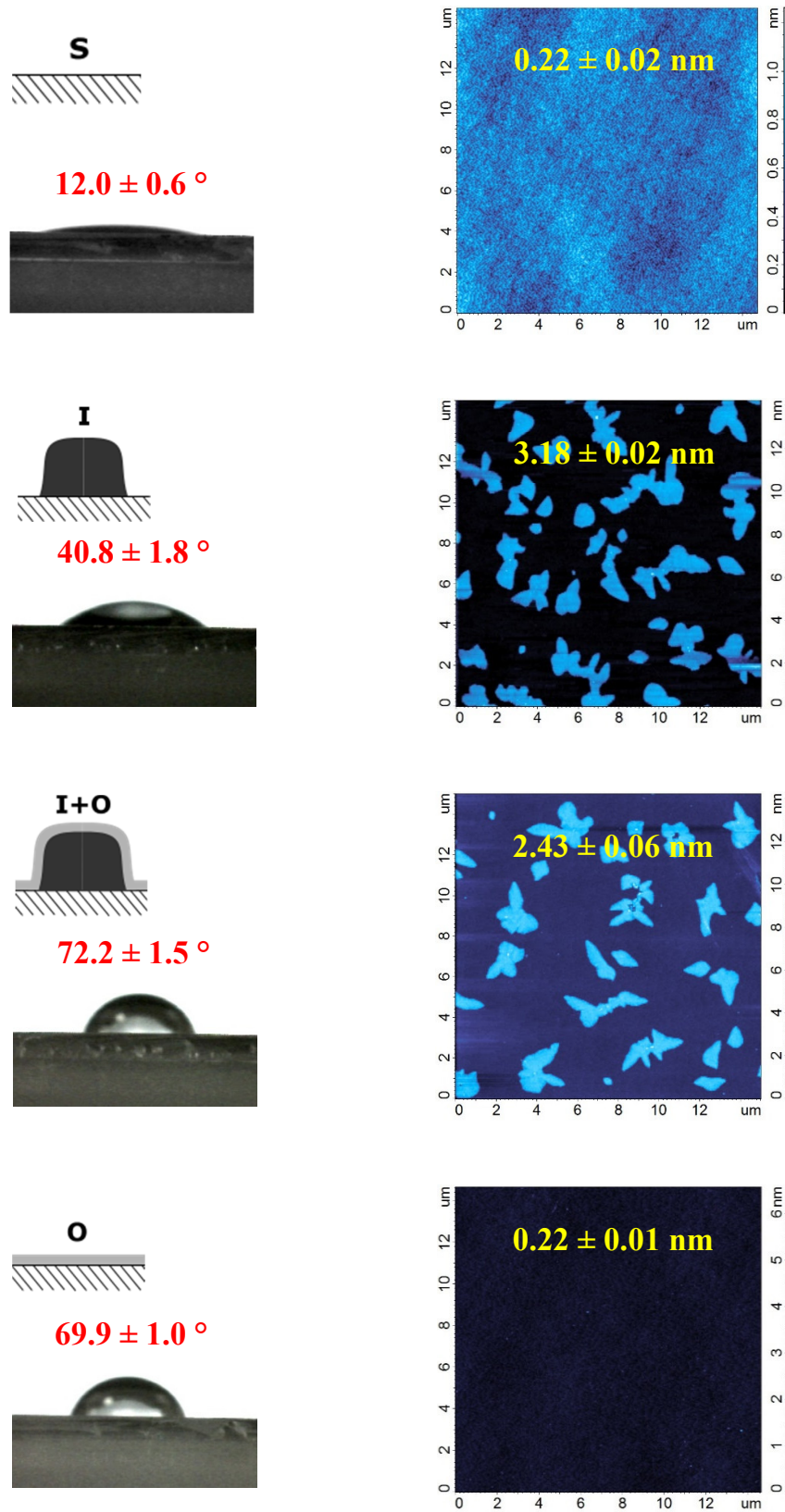


Figure 31. Comparison of surface wettability and morphology for (S) blank silicon

substrate, (I) 2D nano-pattern of PE islands, (I+O) PE nano-pattern overcoated with ultrathin CH plasma polymer and (O) overlayer of CH plasma polymer on silicon. Each sample is depicted with the schematic drawing, the photography of the water droplet on the specimen surface (WCA values are shown in red) and the AFM height image (RMS roughness values are shown in yellow).

The PE nanoisland pattern was activated by the low-pressure Ar plasma with simultaneous overcoating by a layer of hydrocarbon (CH) plasma polymer. For this purpose, an rf magnetron with a graphite target was located beneath the crucible and the substrates. The VPD performed in the first step resulted also in the accumulation of PE deposits on the magnetron target which, together with target's graphite, served as a source of hydrocarbon species for plasma polymerization. The preliminary tests were run to prepare the 40 nm thick CH films on gold-covered flat Si substrates. The FTIR spectrum of this film is presented in Figure 32. The spectrum shows the following absorption bands:

- The aliphatic CH_x groups (stretching vibrations below 3000 cm^{-1} , deformation vibrations bands at 1380 cm^{-1} and 1450 cm^{-1});
- The C=O and C-C groups (stretching over 1500 cm^{-1});
- The C-O-C and C-O-H groups (stretching at 1100 cm^{-1});
- The OH groups (broad stretching band around 3400 cm^{-1}).

The spectrum appears similar to slightly oxidized hydrocarbon plasma polymers produced by magnetron sputtering of PE [75].

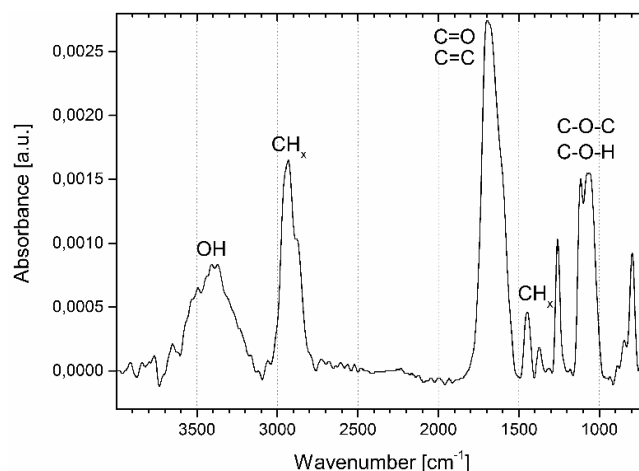


Figure 32. FTIR spectrum of a flat CH plasma polymer overlayer deposited on Si.

The deposition rate of the CH plasma polymer was found to be precisely controlled with sub-nanometer accuracy. As it was identified from ellipsometry measurements, the 30-second magnetron run produced 1.9 ± 0.2 nm thick film on Si. The AFM morphology analysis showed the smooth surface, visually and statistically indistinguishable from the blank silicon substrate (Figure 31 type O). Nevertheless, alteration of the surface properties was detected by measuring WCA. The contact angle of sample with the CH ultra-thin layer was found to be $69.9 \pm 1.0^\circ$ whereas for blank Si it was $12.0 \pm 0.6^\circ$. The increase of contact angle indicates that surface energy of the outermost layer decreased due to the formation of the coating consisting of non-polar hydrocarbon moieties.

The same CH layer was deposited over the pre-fabricated PE nanoisland pattern. The AFM image of the overcoated PE islands shows no changes in the island thickness and shape (Figure 31 type I+O) as compared to the uncoated samples. The island thickness was calculated with respect to the base plane of the underlying substrate, which, in this case, was represented by the CH layer deposited on Si. Invariance of the island thickness indicates that the CH film deposits with identical thickness over the entire surface including both nanoislands and Si. This surface exhibits WCA of $72.2 \pm 1.5^\circ$, corresponding closely to the one obtained for the flat CH plasma polymer. Hence, nano-roughness has negligible effect on the surface wettability.

In this section, physical and chemical properties of CH plasma polymer layer have been described and studied. When deposited over the PE nano-pattern, CH layer preserves the surface morphology and introduces chemical homogeneity over the whole specimen surface. In the section that follows, it will be argued that 2 nm ultra-thin film of CH plasma polymer is capable of immobilizing proteins.

3.3.2. Protein immobilization studies

Ultra-thin layer of CH plasma polymer is an interesting research subject, since the obtained coatings (see 3.3.1 Films analysis) may have numerous applications due to their conformal ability to preserve substrate topography and trapped free radicals. In the present chapter, we investigate biomolecule binding properties of the CH overcoating. First, we will address to the attachment of BSA on flat and on nano-structured thin films. Adsorption of tropoelastin will be discussed next. Moreover, the durability of the CH ultra-thin layer for postponed covalent attachment of biomolecules will be assessed.

The samples of the PE islands overcoated with the ultra-thin CH layer were immersed in 50 $\mu\text{g}/\text{ml}$ albumin solutions for a range of time intervals to examine their maximal BSA binding capacitance. The SDS washing protocol was used to remove physically bound BSA and, after the washing, the XPS analysis was performed to determine the level of N 1s signal related to the amount of albumin covalently attached to the surface (Figure 33). Our findings show that kinetics of covalent albumin binding via plasma polymer overlayer took place in two stages: fast accumulation in the beginning and reaching the saturation plateau later. Maximal binding occurred when specimens were incubated for at least 1 day; the corresponding nitrogen concentration for plateau region was 4.4%. Results of albumin adsorption from the literature point out high adsorption rates with saturation reached in the time scale of minutes, hours at worst [176], [177], [178]. However, the kinetics of irreversible adsorption was hardly studied. The incubation time of 65 h was chosen for the following experiments to maximize the protein attachment to the surface.

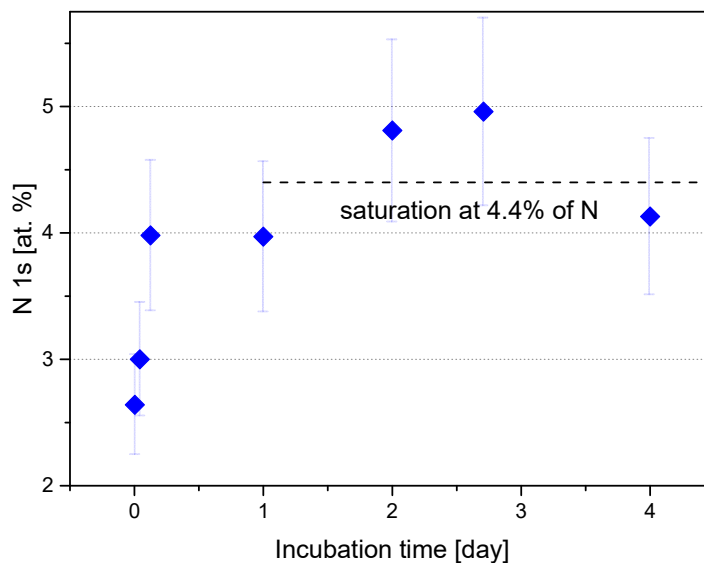


Figure 33. Nitrogen content in atomic percent as measured by XPS as a function of the incubation time in protein solution with albumin. PE islands overcoated with a CH layer were immersed into BSA solution with a delay of 5 min after extraction from deposition apparatus. XPS characterization was performed after SDS washing and indicates a fraction of adsorbed protein layer that is covalently immobilized. The dashed line shows the approximate protein binding saturation level.

The PE nano-island pattern without the CH overlayer was prone to damage by the SDS procedure (not shown). Uncross-linked PE oligomers held together by weak van der Waals forces were easily removed from the surface. The N 1s XPS signal was not detected after the SDS treatment either; hence, all adsorbed protein molecules were removed from the surface. Deposition of the CH plasma polymer overlayer rendered the surface resistant to the rigorous SDS treatment. The stabilization effect of the CH film can be attributed to the high level of crosslinking achieved by employing 30 W discharge.

The XPS analysis of surface chemical composition for flat and nano-structured specimens is demonstrated in Figure 34 to compare the amount of attached albumin before and after the SDS process. Good covalent retention of BSA on both flat and nanostructured samples can be seen: 70 ± 10 % of the initially adsorbed albumin was converted into irreversibly immobilized. Concentration of other elements did not vary significantly either. The presence of PE islands under the overcoating screened photoelectrons from the substrate; consequently, silicon content below of 13 % was detected for the nano-patterned samples while on flat plasma

polymer it exceeded 24%. Accordingly, the carbon content reached 67% for the nano-structured samples while being as low as 49 % for the flat CH layer only.

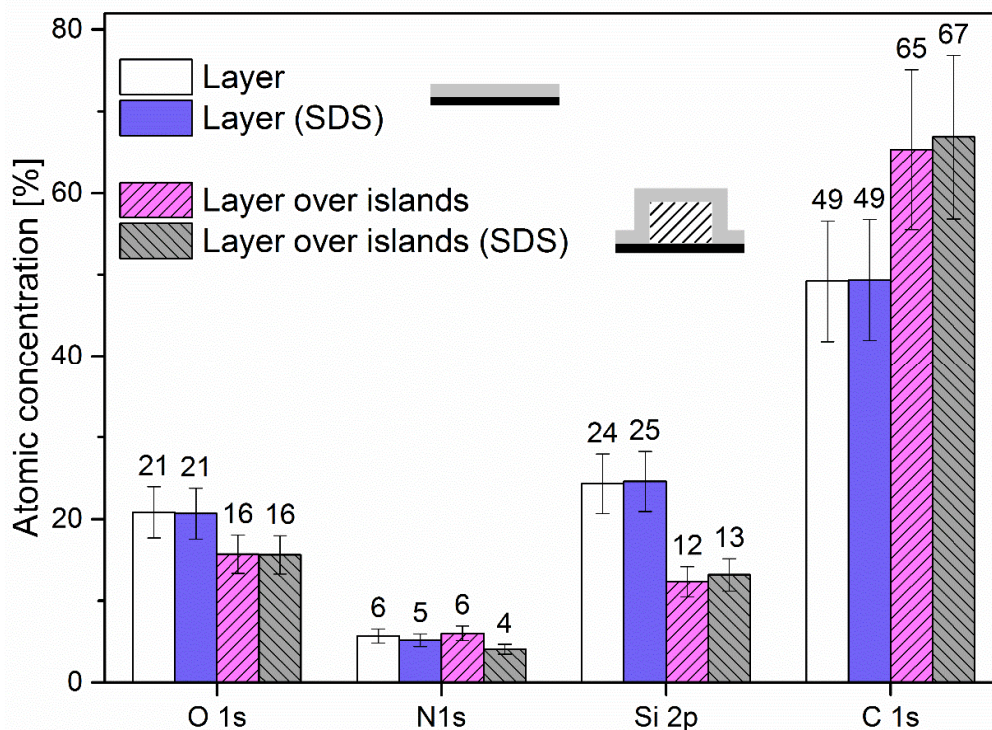


Figure 34. Surface chemical composition for flat and nanostructured thin films before and after SDS treatment. The preparation process included 65 h incubation of surfaces in 50 $\mu\text{g/ml}$ albumin solution.

Albumin is a protein very convenient for model studies of protein adsorption. However, it lacks biofunctionality. Our further research was focused on tropoelastin (TE) binding. TE is an ECM protein. It governs the cell attachment through the interaction with a wide range of cell surface receptors [150], [179], [180]. Tropoelastin was intended to enhance biocompatibility of a model surface with osteoblast-like cells.

Only flat CH plasma polymer was analyzed. Based on the data obtained from the BSA studies, we chose 65 h as the incubation time sufficient to form of the saturated protein concentration on the surface. Identically treated pairs of samples were incubated in the 50 $\mu\text{g/ml}$ solution of TE in PBS for 65 hours and then they were divided into two groups. The first group was processed by the SDS washing and the second group underwent directly the rinsing phase without the SDS washing.

The XPS nitrogen content measured on the sample pairs yields the higher value of 10.8 % for the samples without the SDS washing and 7.3 % for the SDS treated samples. The decrease is associated with the removal of loosely bound protein by the SDS treatment. Overall, TE demonstrated approximately the same value of the protein retention (68 ± 5 %) on the flat surface of CH plasma polymer as compared to anchoring of BSA.

The presence of tropoelastin was also identified in the high-resolution XPS spectra of Figure 35 where the N 1s and the C 1s signals are compared for the sample incubated in TE and for the sample simultaneously incubated in pure PBS without any protein. The N 1s region (Figure 35 A) clearly shows no nitrogen for the sample incubated in pure PBS (the black curve) whereas the N 1s peak is very well developed for the TE incubated sample (the blue curve). Subtraction of the spectra is represented by the red curve and it reasonably coincides with the spectrum of the protein-incubated specimen. The C 1s signal supports this trend. The C 1s peak of the pure PBS incubated sample (Figure 35 B, the black curve) is centered at 285.0 eV (the C-C/C-H bonds) with asymmetry to the higher binding energy side, showing slight oxidation of the CH plasma polymer layer. In the case of the TE-mediated surface (the blue curve), a tale at the higher binding energy side becomes more developed. The subtraction of the spectra (red curve) reflects the appearance of the bonding environment at 288.1 eV (C=O) and 286.3 eV (the C-O/C-N bonds) which is a characteristic feature of proteins [181].

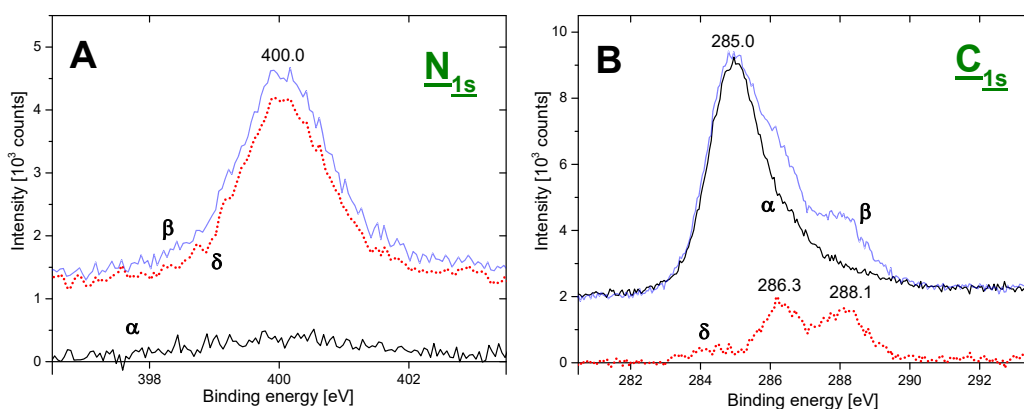


Figure 35. (A) XPS N 1s spectrum of CH plasma polymer layer incubated in (α) buffer solution and (β) TE solution with SDS post-processing and (δ) difference

between these two spectra. (B) XPS C1s spectrum of CH plasma polymer layer incubated in (α) buffer solution and (β) TE solution with SDS post-processing and (δ) difference between these two spectra.

Plasma polymers usually incorporate a significant amount of free radicals. It is known that radicals may recombine in the film bulk or migrate to the surface and react with adsorbed proteins via functional groups present in the protein structure. A fall in the radical concentration reduces the covalent binding ability of radical-rich layer with the storage time. For instance, the 14-month aging of PIII treated poly(tetrafluoroethylene) increased the incubation time required to covalently couple a monolayer of protein from 35 minutes to 92 hours [121]. The treated PTFE performance was dependent on the initial density of free radicals and the depth of the treated layer which served as a free radical reservoir.

Here, we report on the nitrogen content measured for the SDS-processed samples (7 nm-thick nano-pattern and 2 nm CH overlayer) as a function of the aging time in the laboratory atmosphere (Figure 36). The 65-hour incubation time in the 50 $\mu\text{g/ml}$ BSA solution was chosen for all the samples. The high level of residual nitrogen after the SDS washing was observed for the samples aged for up to several days with the mean level of N being at 4.9%. A related point to consider is that this value is in a close agreement with the saturation level of 4.4 % of N from the studies of the incubation time shown above (Figure 33). After 7 days of the storage, the amount of protein began to follow a decreasing trend indicating that there is a decrease in the CH plasma polymer capacity to covalently immobilize biomolecules. Nevertheless, even after a 3-month aging time the samples were able to covalently bind BSA to a reasonable extent (70 ± 10 % of the covalently bound protein on fresh surfaces). Thus, even ultra-thin CH plasma polymer maintains the protein covalent coupling capability for up to one week (if 65 h long incubation time is used) which is a sufficient timeframe for many practical applications.

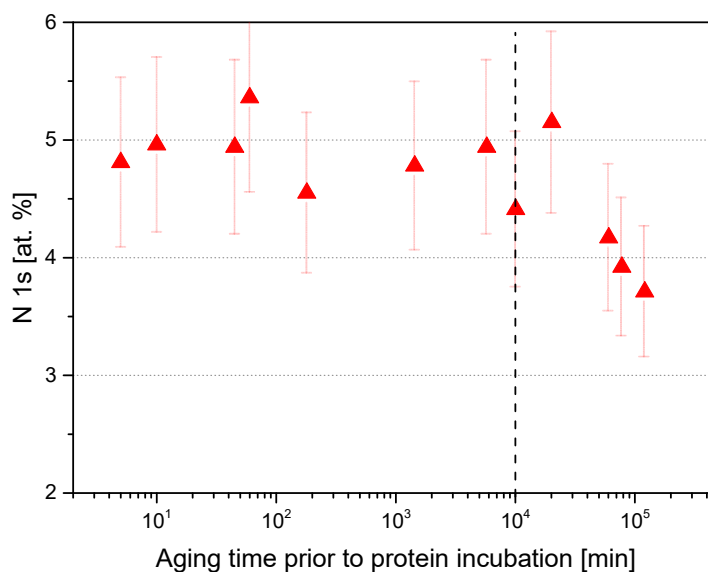


Figure 36. Nitrogen content in atomic percent as measured by XPS as a function of the time elapsed between fabrication of CH plasma polymer layer over PE nanopattern and their incubation in BSA solution. The incubation time in the protein solution was 65 hours for all samples. XPS was measured after SDS washing and double rinsing in purified water. A dashed line indicates the start of deterioration of covalent binding of albumin after 7 days of sample aging.

The most important outcome of this chapter is the evidence of the successful use of ultra-thin CH plasma polymer overlayer for covalent linking of proteins from solution. Radicals created within the film were employed for binding two different proteins (BSA and TE). A universal coupling mechanism for both types of the biomolecules was found. We discovered a remarkable characteristic of the ultra-thin plasma polymer coating to preserve long-term capturing performance even when specimens were stored in atmosphere for more than 7 days.

3.3.3. Osteoblast cell adhesion, growth and differentiation

Implanted biomedical devices, such as orthopaedic implants, pacemakers, or cochlear implants, extend functionality of human bodies in case of issues with native body parts. However, the implantation of devices into tissues is still not a well-established procedure and unfavorable body responses are common [117], [182]. Host's recognition of implanted material as a foreign body belongs to the most

frequent reasons of implant failure. The foreign-body response can be avoided by masking the artificial origin of implant surface, i.e. by improving biocompatibility. In this thesis, we aimed to understand the effectiveness of nano-topographical features and covalently adsorbed ECM protein to trigger favorable response of MG-63 osteoblast-like cells. PE nano-structured surfaces were employed to model nano-textured morphology. Ultra-thin CH plasma polymer provided conformal overcoating and binding platform for fabrication of functional tropoelastin interlayer. The discussion about cell adhesion tests is divided into two parts: first, the analysis of smooth surfaces will be presented followed by the studies of nano-structured surfaces.

Figure 37 A presents the experimental data on the number of osteoblast-like MG63 cells as a function of time after seeding on tropoelastin-coated and uncoated flat CH surfaces. The results on reference poly(styrene) (PS) are also shown. Cell count on Day 1 was higher for samples with pre-adsorbed protein. From Day 2 to 3 after seeding, the osteoblast-like cells proliferated with no significant difference between TE-coated flat films, flat films without TE and the reference TCP. However at Day 4, the number of cells on the CH flat layers without TE was 38 % lower than that on the TE-mediated surfaces. The latter even dominated the cell count on TCP controls. Furthermore, 24 % larger spreading area of cells was detected on TE-coated flat CH surface as compared to no-protein interlayer samples (Figure 38 A, B, F). Fluorescent imaging revealed well-developed (elongated and polygonal shapes) cytoskeletons for cells. The most likely cause of higher initial adhesion and spreading of cells on surfaces with TE is a higher concentration and accessibility of oligopeptidic ligands in tropoelastin molecules to cell adhesion receptors. In the instance of flat surfaces without TE, the cell adhesion is mediated only by proteins spontaneously adsorbed to the surface from the serum of the culture medium (i.e., fibronectin) [175]. These results suggest that despite granting high initial adhesion and spreading area, TE-modified CH surfaces require at least 4 days to provide the proliferation of MG63 cells superior to TCP controls. Our long-term vision is to develop multifunctional surfaces that enhance cell binding and promote bone-to-implant contact. Thus, CH overlayer coated with tropoelastin deserve attention in biomedical devices with long integration period, for example, hip prostheses. The 4-days lag in promotion of bone cell proliferation is not comparable with several months of hip prosthesis healing [183].

Osteoblast-like MG-63 cell behavior was also assessed on the nanostructured surfaces of PE islands overcoated with the ultra-thin CH layer with or without tropoelastin. Surface topography was constructed from 8 nm-thick PE islands with the mean area of $1.8 \pm 1.4 \mu\text{m}^2$ and the average nearest neighbor distance of $2.2 \pm 0.8 \mu\text{m}$. This pattern was chosen because it was at a comparable scale to the $\sim 15 \text{ nm}$ typical cell membrane-to-surface distance for integrin-mediated adhesion [184] and to typical focal adhesion size (units of μm^2) [185]. However, the cell spreading area on PE islands covered by the CH plasma polymer overlayer was lower than on the flat surfaces (Figure 38 F). The same tendency was observed even for specimens with the tropoelastin layer. The cell shapes on nanostructured materials were more round than on the flat surfaces (Figure 38 C, D). The number of initially adhering cells was similar on both elastin-coated and uncoated islands Figure 37 B. Further temporal evolution of the cell number copied the trend of the flat CH overlayer. Nevertheless, the statistical significance was found only on day 2 after seeding, when the number on tropoelastin-coated islands was higher than on uncoated islands. On days 3 and 4 after seeding, the cell number on tropoelastin-coated islands was on the average higher than on uncoated ones, but these differences were not significant. It could be due to the fact that the cell coverage of the surfaces with islands was less homogeneous, and thus the variation among the data was wider. It was concluded that nanostructured morphology at the scales studied here might have not been optimal for promoting the osteoblast adhesion.

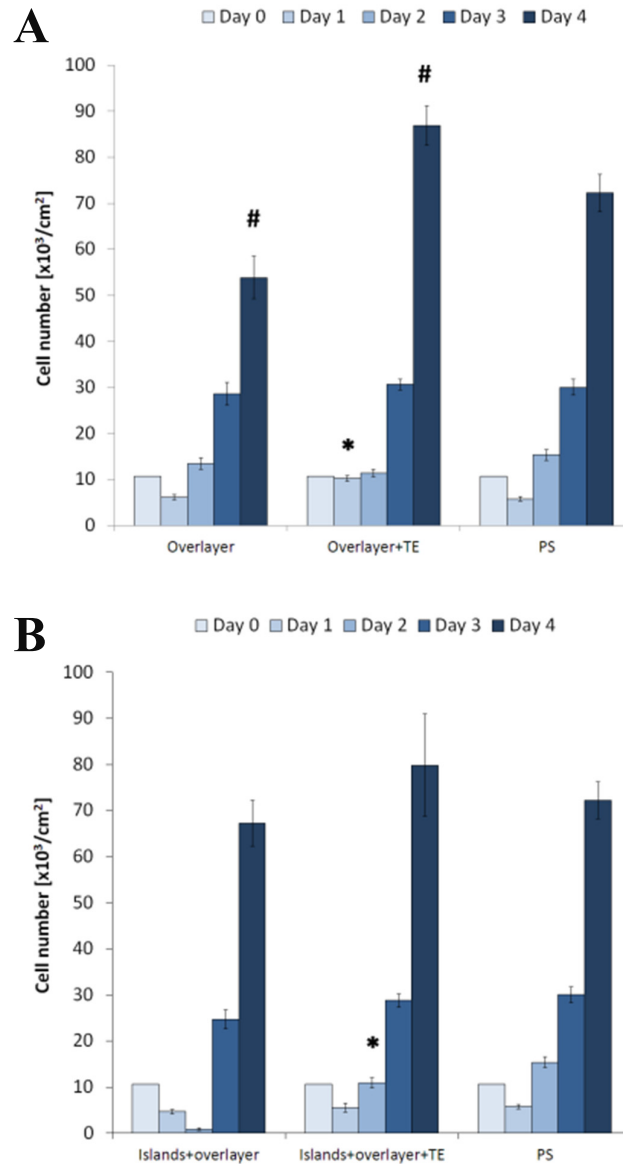


Figure 37. Temporal evolution of the number of human osteoblast-like MG-63 cells after seeding on the samples with the CH overlayer only, on the samples with the CH overlayer coated with tropoelastin and on the reference TCP (indicated by the label PS) cell culture dishes; (A) continuous CH plasma polymer overlayer on Si, (B) PE islands covered by the CH plasma polymer overlayer. Asterisks above the columns indicate the experimental groups significantly differing ($p \leq 0.05$) in cell number to the reference PS and CH plasma polymer layers (with or without islands) in individual time intervals. Hashmarks above the columns indicate the experimental groups significantly differing ($p \leq 0.05$) in cell number to the reference PS on day 4 after seeding.

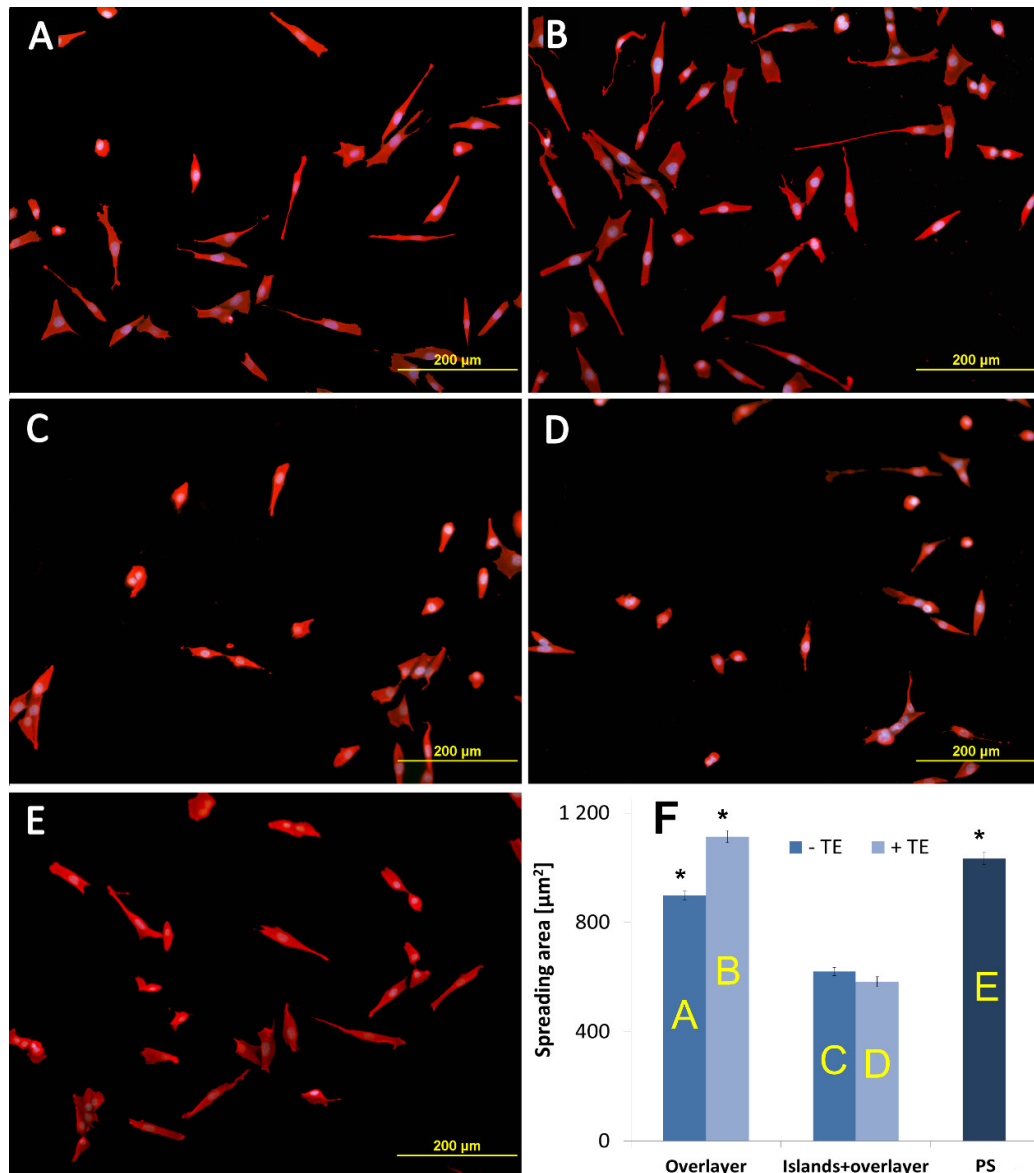


Figure 38. Human osteoblast-like MG-63 cells in 1-day-old cultures on the samples (A, C) without tropoelastin, (B, D) tropoelastin-coated and (E) on reference TCP. Panels A, B: flat CH plasma polymer overlayer on Si, C, D: PE islands covered by the CH plasma polymer overlayer, F: cell spreading area of human osteoblast-like MG-63 cells in 1-day-old cultures on the samples A-E. Asterisks above the columns indicate experimental groups significantly differing ($p \leq 0.05$) in spreading area to all tested samples.

CONCLUSIONS

The following objectives have been achieved:

- Poly(ethylene) films were produced by physical vapor deposition. This bottom-up approach revealed the island growth mode during the early stages of the film formation on silicon.
- For the first time, the size of the critical nucleus for macromolecular system at vacuum/solid interface was reported. Three methods were applied to measure the critical nucleus size for PE deposition on silicon. According to the capture zone distribution approach, the critical island size was either two or three PE oligomers.
- Modification by atmospheric pressure plasma discharge produced physico-chemical changes in a thin layer of PE. These changes include: an increase in surface energy, a carbonization process, appearance of active free radicals and smoothening of the polymer surface.
- Atmospheric pressure (helium and argon) DBD was efficient in the activation of PE nano-patterns that can be used for covalent immobilization of biomolecules directly from the solution. Tropoelastin was selectively bound to activated PE islands.
- Magnetron sputtering was used to produce ultra-thin hydrocarbon plasma polymer coating. The coating facilitated covalent immobilization of protein and demonstrated binding capability even after being stored in atmosphere for more than 7 days.
- Cell attachment experiments identified osteoblast-like cells behavior as a function of morphology and presence of ECM protein layer. Flat tropoelastin-coated surfaces promoted the cell adhesion, proliferation and differentiation. The enhancing effect of nanoarchitecture was not detected, probably due to mismatch between the surface nanostructure and the MG-63 cell adhesion complexes.

BIBLIOGRAPHY

- [1] I. Bars and J. Terning, *Extra Dimensions in Space and Time*. Springer-Verlag New York, 2010.
- [2] Y. Xia *et al.*, *Adv. Mater.*, vol. 15, no. 5, pp. 353–389, Mar. 2003.
- [3] S. Mueller, *Upgrading and Repairing PCs (17th Edition)*. Que, 2006.
- [4] Intel, ‘Intel® 14 nm Technology’, *Intel*, 2015. [Online]. Available: <http://www.intel.com/content/www/us/en/silicon-innovations/intel-14nm-technology.html>.
- [5] X. Sun and H. Li, *Nanotechnology*, vol. 24, p. 355706, 2013.
- [6] S. Thomas, J. Joy, and R. Shanks, ‘Micro- and nanostructured polymer systems : from synthesis to applications’. 2015.
- [7] H. Gleiter, *Acta Mater.*, vol. 48, no. 1, pp. 1–29, 2000.
- [8] F. Brétagnot, A. Valsesia, T. Sasaki, G. Ceccone, P. Colpo, and F. Rossi, *Adv. Mater.*, vol. 19, no. 15, pp. 1947–1950, 2007.
- [9] A. Biswas, I. S. Bayer, A. S. Biris, T. Wang, E. Dervishi, and F. Faupel, *Adv. Colloid Interface Sci.*, vol. 170, no. 1–2, pp. 2–27, 2012.
- [10] B. D. Gates, Q. Xu, M. Stewart, D. Ryan, C. G. Willson, and G. M. Whitesides, ‘New approaches to nanofabrication: Molding, printing, and other techniques’, *Chemical Reviews*, vol. 105, no. 4. pp. 1171–1196, 2005.
- [11] D. Mailly, ‘Nanofabrication techniques’, *European Physical Journal: Special Topics*, vol. 172, no. 1. pp. 333–342, 2009.
- [12] F. Dinelli, M. Murgia, P. Levy, M. Cavallini, F. Biscarini, and D. M. De Leeuw, *Phys. Rev. Lett.*, vol. 92, no. March, pp. 116802–1, 2004.
- [13] E. Bauer, *Zeitschrift fur Krist. - New Cryst. Struct.*, vol. 110, no. 1–6, pp. 372–394, 1958.
- [14] J. Bloem and W. A. P. Claassen, *J. Cryst. Growth*, vol. 49, no. 3, pp. 435–444, 1980.
- [15] J. Bloem, W. A. P. Claassen, and W. G. J. N. Valkenburg, *J. Cryst. Growth*, vol. 57, no. 1, pp. 177–184, 1982.

- [16] F. Schreiber, ‘Organic Molecular Beam Deposition: Growth Studies beyond the First Monolayer’, in *Physics of Organic Semiconductors*, vol. 1054, no. 6, Weinheim, FRG: Wiley-VCH Verlag GmbH & Co. KGaA, 2006, pp. 15–40.
- [17] S. Kowarik, A. Gerlach, and F. Schreiber, *J. Phys. Condens. Matter*, vol. 20, no. 18, p. 184005, May 2008.
- [18] G. Hlawacek, P. Puschnig, P. Frank, A. Winkler, C. Ambrosch-draxl, and C. Teichert, *Science (80-.)*, vol. 321, no. 5885, pp. 108–111, 2008.
- [19] P. Jensen, *Rev. Mod. Phys.*, vol. 71, no. 5, pp. 1695–1735, 1999.
- [20] J. a. Venables, *Vacuum*, vol. 33, no. 10–12, pp. 701–705, Oct. 1983.
- [21] J. G. Amar and F. Family, *Phys. Rev. B*, vol. 50, no. 12, pp. 8781–8797, 1994.
- [22] J. G. Amar and F. Family, *Phys. Rev. Lett.*, vol. 74, no. 11, pp. 2066–2069, 1995.
- [23] J. W. Evans, P. A. Thiel, and M. C. Bartelt, *Surf. Sci. Rep.*, vol. 61, no. 1–2, pp. 1–128, 2006.
- [24] A. Pimpinelli and T. L. Einstein, *Phys. Rev. Lett.*, vol. 99, no. November, p. 5, 2006.
- [25] C. K. Chiang *et al.*, *Phys. Rev. Lett.*, vol. 39, no. 17, pp. 1098–1101, Oct. 1977.
- [26] S. R. Forrest, *Chem. Rev.*, vol. 97, no. 94, pp. 1793–1896, 1997.
- [27] D. G. Castner and B. D. Ratner, *Surf. Sci.*, vol. 500, no. 1–3, pp. 28–60, 2002.
- [28] ‘This work, “An OMBD Chamber Concept Drawing”, is a derivative of “A Molecular Beam Epitaxy reaction chamber concept drawing” by Vegar Ottesen, used under CC BY-SA 3.0. “An OMBD Chamber Concept Drawing” is licensed under CC BY-SA 3.0 by Iurii Melnichuk.’ .
- [29] E. I. Haskal, F. F. So, P. E. Burrows, and S. R. Forrest, *Appl. Phys. Lett.*, vol. 60, no. 26, 1992.
- [30] H. Tada, T. Kawaguchi, and A. Koma, *Appl. Phys. Lett.*, vol. 61, no. 17, 1992.
- [31] M. Sparenberg *et al.*, *Phys. Chem. Chem. Phys.*, vol. 16, no. 47, pp. 26084–26093, 2014.
- [32] A. J. Lovinger, S. R. Forrest, M. L. Kaplan, P. H. Schmidt, and T. Venkatesan,

- J. Appl. Phys.*, vol. 55, no. 2, 1984.
- [33] L. Casalis *et al.*, *Phys. Rev. Lett.*, vol. 90, no. 20, pp. 18–21, 2003.
- [34] G. Hlawacek and C. Teichert, *J. Phys. Condens. Matter*, vol. 25, p. 143202, 2013.
- [35] ‘PubChem Compound Database; CID=8671’, *National Center for Biotechnology Information*. [Online]. Available: <https://pubchem.ncbi.nlm.nih.gov/compound/8671>. [Accessed: 27-Oct-2016].
- [36] R. Ruiz *et al.*, *Chem. Mater.*, vol. 16, pp. 4497–4508, 2004.
- [37] F. J. Meyer zu Heringdorf, M. C. Reuter, and R. M. Tromp, *Nature*, vol. 412, no. 6846, pp. 517–520, 2001.
- [38] A. Winkler and L. Tumbek, *J. Phys. Chem. Lett.*, vol. 4, no. 23, pp. 4080–4084, 2013.
- [39] B. Stadlober, U. Haas, H. Maresch, and a. Haase, *Phys. Rev. B - Condens. Matter Mater. Phys.*, vol. 74, pp. 1–9, 2006.
- [40] C. D. Dimitrakopoulos, a. R. Brown, and a. Pomp, *J. Appl. Phys.*, vol. 80, no. 1996, p. 2501, 1996.
- [41] M. Kasaya, H. Tabata, and T. Kawai, *Surf. Sci.*, vol. 400, no. 1–3, pp. 367–374, 1998.
- [42] K. P. Weidkamp, C. A. Hacker, M. P. Schwartz, X. Cao, R. M. Tromp, and R. J. Hamers, *J. Phys. Chem. B*, vol. 107, no. 40, pp. 11142–11148, 2003.
- [43] D. Käfer, C. Wöll, and G. Witte, *Appl. Phys. A Mater. Sci. Process.*, vol. 95, no. 1, pp. 273–284, 2009.
- [44] ‘PubChem Compound Database; CID=60081627’, *National Center for Biotechnology Information*. .
- [45] L. Athouël, G. Froyer, M. T. Riou, and M. Schott, *Thin Solid Films*, vol. 274, no. 1–2, pp. 35–45, 1996.
- [46] L. Tumbek, C. Gleichweit, K. Zojer, and A. Winkler, *Phys. Rev. B - Condens. Matter Mater. Phys.*, vol. 86, no. 8, pp. 1–11, 2012.
- [47] D. Wrana *et al.*, *J. Phys. Chem. C*, vol. 119, no. 29, pp. 17004–17015, 2015.
- [48] S. Lorbek, G. Hlawacek, and C. Teichert, *Eur. Phys. J. Appl. Phys.*, vol. 55,

no. 2, p. 23902, Aug. 2011.

- [49] T. Potocar *et al.*, *Phys. Rev. B - Condens. Matter Mater. Phys.*, vol. 83, pp. 1–10, 2011.
- [50] ‘PubChem Compound Database; CID=96712’, *National Center for Biotechnology Information*. [Online]. Available: <https://pubchem.ncbi.nlm.nih.gov/compound/96712>. [Accessed: 27-Oct-2016].
- [51] A. C. Dürr *et al.*, *Appl. Phys. Lett.*, vol. 81, no. 12, pp. 2276–2278, 2002.
- [52] X. N. Zhang, E. Barrena, D. G. de Oteyza, and H. Dosch, *Surf. Sci.*, vol. 601, no. 12, pp. 2420–2425, 2007.
- [53] ‘PubChem Compound Database; CID=6524626’, *National Center for Biotechnology Information*. .
- [54] E. Barrena, D. G. de Oteyza, H. Dosch, and Y. Wakayama, *ChemPhysChem*, vol. 8, no. 13, pp. 1915–1918, 2007.
- [55] J. O. Ossó *et al.*, *Adv. Funct. Mater.*, vol. 12, no. 6–7, pp. 455–460, 2002.
- [56] W. Chen, H. Huang, S. Chen, Y. L. Huang, X. Y. Gao, and A. T. S. Wee, *Chem. Mater.*, vol. 20, no. 22, pp. 7017–7021, 2008.
- [57] P. J. Flory, *Principles of polymer chemistry*. Cornell University Press, 1953.
- [58] S. L. Madorsky, S. Straus, D. Thompson, and L. Williamson, *J. Polym. Sci.*, vol. 4, no. 5, pp. 639–664, 1949.
- [59] S. L. Madorsky, *J. Polym. Sci.*, vol. 9, no. 2, pp. 133–156, 1952.
- [60] P. P. Luff and M. White, *Thin Solid Films*, vol. 6, no. 3, pp. 175–195, 1970.
- [61] N. Boonthanom and M. White, *Thin Solid Films*, vol. 24, no. 2, pp. 295–306, 1974.
- [62] M. White, *Vacuum*, vol. 15, no. 9, pp. 449–450, 1965.
- [63] M. Satou, Y. Watanabe, and H. Hayashi, *J. Polym. Sci. Part A-2 Polym. Phys.*, vol. 10, no. 5, pp. 835–845, May 1972.
- [64] N. Li, B. Li, G. Yang, and C. Y. Li, *Langmuir*, vol. 23, no. 16, pp. 8522–8525, 2007.
- [65] B. Chu, B. Chu, J. E. Spanier, J. E. Spanier, C. Y. Li, and C. Y. Li, *Nano*, pp.

24–29, 2006.

- [66] O. Kylián, A. Choukourov, and H. Biederman, *Thin Solid Films*, vol. 548, pp. 1–17, Dec. 2013.
- [67] J. Friedrich, *Plasma Process. Polym.*, vol. 8, no. 9, pp. 783–802, 2011.
- [68] A. . Thenard and C. R. Hebd, *Seances Acad. Sci.*, vol. 78, p. 219, 1874.
- [69] M. P. Wilde, *Eur. J. Inorg. Chem.*, vol. 7, p. 352, 1874.
- [70] H. König and G. Helwig, *Zeitschrift für Phys.*, vol. 129, no. 5, pp. 491–503, 1951.
- [71] H. Kobayashi, A. T. Bell, and M. Shen, *Macromolecules*, vol. 7, no. 3, pp. 277–283, 1974.
- [72] M. Shen, *Plasma Chemistry of Polymers*. New York: Marcel Dekker, 1976.
- [73] H. Yasuda and C. E. Lamaze, *J. Appl. Polym. Sci.*, vol. 15, no. 9, pp. 2277–2292, 1971.
- [74] H. Yasuda, *Plasma Polymerization*. New York: Academic Press, 1985.
- [75] I. Kholodkov, H. Biederman, D. Slavinská, A. Choukourov, and M. Trchova, *Vacuum*, vol. 70, no. 4, pp. 505–509, 2003.
- [76] A. Michelmore, P. Martinek, V. Sah, R. D. Short, and K. Vasilev, *Plasma Process. Polym.*, vol. 8, no. 5, pp. 367–372, 2011.
- [77] R. Gristina *et al.*, *J. Biomed. Mater. Res. Part B Appl. Biomater.*, vol. 88B, no. 1, pp. 139–149, 2009.
- [78] G. Cicala, A. Milella, F. Palumbo, P. Favia, and R. d’Agostino, *Diam. Relat. Mater.*, vol. 12, no. 10–11, pp. 2020–2025, 2003.
- [79] A. . Milella, F. . Palumbo, P. . Favia, G. . Cicala, and R. . D’Agostino, *Pure Appl. Chem.*, vol. 77, no. 2, pp. 399–414, 2005.
- [80] A. Milella, R. Di Mundo, F. Palumbo, P. Favia, F. Fracassi, and R. d’Agostino, *Plasma Process. Polym.*, vol. 6, no. 6–7, pp. 460–466, 2009.
- [81] R. Di Mundo *et al.*, *Plasma Process. Polym.*, vol. 7, pp. 212–223, 2010.
- [82] M. Drábik *et al.*, *Plasma Process. Polym.*, vol. 7, no. 7, pp. 544–551, 2010.
- [83] O. Kylián *et al.*, *Thin Solid Films*, vol. 519, no. 19, pp. 6426–6431, 2011.

- [84] A. Choukourov *et al.*, *Plasma Process. Polym.*, vol. 9, no. 1, pp. 48–58, 2012.
- [85] A. Choukourov *et al.*, *Plasma Process. Polym.*, vol. 7, no. 6, pp. 445–458, 2010.
- [86] P. Koegler, A. Clayton, H. Thissen, G. N. C. Santos, and P. Kingshott, *Adv. Drug Deliv. Rev.*, vol. 64, no. 15, pp. 1820–1839, 2012.
- [87] P. Kingshott, G. Andersson, S. L. McArthur, and H. J. Griesser, *Curr. Opin. Chem. Biol.*, vol. 15, no. 5, pp. 667–676, 2011.
- [88] W. Song and H. Chen, *Chinese Sci. Bull.*, vol. 52, no. 23, pp. 3169–3173, 2007.
- [89] V. A. . Schulte, M. . Diez, M. . Möller, and M. C. . b Lensen, *Biomacromolecules*, vol. 10, no. 10, pp. 2795–2801, 2009.
- [90] J. . Heitz *et al.*, *J. Nanomater.*, vol. 2011, 2011.
- [91] M. J. Dalby *et al.*, *Nat. Mater.*, vol. 6, no. 5, pp. 407–413, 2007.
- [92] M. Vandrovcova *et al.*, *J. Biomed. Mater. Res. A*, vol. 100, no. 4, pp. 1016–32, Apr. 2012.
- [93] L. E. McNamara, R. J. McMurray, M. J. P. Biggs, F. Kantawong, R. O. C. Oreffo, and M. J. Dalby, *J. Tissue Eng.*, vol. 2010, no. 1, p. 120623, 2010.
- [94] G.-J. Zhang *et al.*, *Small*, vol. 1, no. 8–9, pp. 833–837, 2005.
- [95] L. G. Rosa and J. Liang, *J. Phys. Condens. Matter*, vol. 21, no. 48, p. 483001, 2009.
- [96] X.-M. Li, J. Huskens, and D. N. Reinhoudt, *J. Mater. Chem.*, vol. 14, no. 20, p. 2954, 2004.
- [97] J. R. Kenseth, J. a. Harnisch, V. W. Jones, and M. D. Porter, *Langmuir*, vol. 17, no. 13, pp. 4105–4112, 2001.
- [98] T. Blättler *et al.*, *J. Nanosci. Nanotechnol.*, vol. 6, no. 8, pp. 2237–2264, 2006.
- [99] R. Langer and D. a Tirrell, *Nature*, vol. 428, no. 6982, pp. 487–492, 2004.
- [100] K. Rezwan, Q. Z. Chen, J. J. Blaker, and A. R. Boccaccini, ‘Biodegradable and bioactive porous polymer/inorganic composite scaffolds for bone tissue engineering’, *Biomaterials*, vol. 27, no. 18. pp. 3413–3431, 2006.
- [101] B. D. Ratner, A. S. Hoffman, F. J. Schoen, and J. E. Lemons, *Biomaterials*

Science, Third Edition: An Introduction to Materials in Medicine, 3rd ed. Academic Press, 2012.

- [102] B. D. Ratner, *J. Biomed. Mater. Res.*, vol. 27, no. 7, pp. 837–850, 1993.
- [103] Y. Naito *et al.*, *Adv. Drug Deliv. Rev.*, vol. 63, no. 4–5, pp. 312–323, 2011.
- [104] M. Sokolsky-Papkov, K. Agashi, A. Olaye, K. Shakesheff, and A. J. Domb, *Adv. Drug Deliv. Rev.*, vol. 59, no. 4–5, pp. 187–206, 2007.
- [105] M. . Gerard, A. . Chaubey, and B. D. . Malhotra, *Biosens. Bioelectron.*, vol. 17, no. 5, pp. 345–359, 2002.
- [106] R. Morent, N. De Geyter, T. Desmet, P. Dubruel, and C. Leys, *Plasma Process. Polym.*, vol. 8, no. 3, pp. 171–190, 2011.
- [107] C. Mao, J. Yuan, H. Mei, A. Zhu, J. Shen, and S. Lin, *Mater. Sci. Eng. C*, vol. 24, no. 4, pp. 479–485, 2004.
- [108] J.-C. Lin, T.-M. Ko, and S. L. Cooper, *J. Colloid Interface Sci.*, vol. 164, no. 1, pp. 99–106, 1994.
- [109] K. Ishihara, Y. Iwasaki, S. Ebihara, Y. Shindo, and N. Nakabayashi, *Colloids Surfaces B Biointerfaces*, vol. 18, no. 3–4, pp. 325–335, 2000.
- [110] O. H. Kwon, Y. C. Nho, K. D. Park, and Y. H. Kim, *J. Appl. Polym. Sci.*, vol. 71, no. 4, pp. 631–641, 1999.
- [111] G. Voggenreiter, K. Hartl, S. Assenmacher, M. Chatzinikolaidou, H. P. Jennissen, and H. M. Rumpf, *Materwiss. Werksttech.*, vol. 32, no. 12, pp. 942–948, 2001.
- [112] B. R. Coad, M. Jasieniak, S. S. Griesser, and H. J. Griesser, *Surf. Coatings Technol.*, vol. 233, pp. 169–177, Oct. 2013.
- [113] P. Kingshott, J. Wei, D. Bagge-Ravn, N. Gadegaard, and L. Gram, *Langmuir*, vol. 19, no. 17, pp. 6912–6921, Aug. 2003.
- [114] P. Angenendt, *Drug Discov. Today*, vol. 10, no. 7, pp. 503–511, 2005.
- [115] S. Puertas *et al.*, *Biosens. Bioelectron.*, vol. 43, pp. 274–280, 2013.
- [116] M. Cretich, F. Damin, G. Pirri, and M. Chiari, *Biomol. Eng.*, vol. 23, no. 2–3, pp. 77–88, 2006.
- [117] M. M. M. Bilek, *Appl. Surf. Sci.*, vol. 310, pp. 3–10, 2014.

- [118] J. R. Conrad, J. L. Radtke, R. A. Dodd, F. J. Worzala, and N. C. Tran, *J. Appl. Phys.*, vol. 62, no. 11, pp. 4591–4596, 1987.
- [119] M. M. Bilek and D. R. McKenzie, *Biophys. Rev.*, vol. 2, no. 2, pp. 55–65, Feb. 2010.
- [120] A. Kondyurin, P. Naseri, K. Fisher, D. R. McKenzie, and M. M. M. Bilek, *Polym. Degrad. Stab.*, vol. 94, no. 4, pp. 638–646, 2009.
- [121] M. M. M. Bilek, D. V Bax, A. Kondyurin, Y. Yin, N. J. Nosworthy, and K. Fisher, *Proc. Natl. Acad. Sci.*, vol. 108, no. 35, p. 6, 2011.
- [122] Y. Yin *et al.*, *Plasma Process. Polym.*, vol. 6, no. 10, pp. 658–666, 2009.
- [123] N. J. Nosworthy, J. P. Y. Ho, A. Kondyurin, D. R. McKenzie, and M. M. M. Bilek, *Acta Biomater.*, vol. 3, no. 5, pp. 695–704, Sep. 2007.
- [124] J. P. Y. Ho *et al.*, *Plasma Process. Polym.*, vol. 4, no. 5, pp. 583–590, 2007.
- [125] B. K. Gan, N. J. Nosworthy, D. R. McKenzie, C. G. Dos Remedios, and M. M. M. Bilek, *J. Biomed. Mater. Res. A*, vol. 85, no. 3, pp. 605–10, Jun. 2008.
- [126] P. Lisboa, A. Valsesia, P. Colpo, F. Rossi, and M. Mascini, *Anal. Lett.*, vol. 43, no. 10–11, pp. 1556–1571, Jul. 2010.
- [127] W. Siemens, *Ann. Phys.*, vol. 178, no. 9, pp. 66–122, 1857.
- [128] U. Kogelschatz, vol. 23, no. 1, pp. 1–46, 2003.
- [129] C. Tendero, C. Tixier, P. Tristant, J. Desmaison, and P. Leprince, *Spectrochim. Acta - Part B At. Spectrosc.*, vol. 61, no. 1, pp. 2–30, 2006.
- [130] N.-Y. Cui and N. M. D. Brown, *Appl. Surf. Sci.*, vol. 189, no. 1–2, pp. 31–38, 2002.
- [131] Z. Fang, J. Lin, H. Yang, Y. Qiu, and E. Kuffel, *IEEE Trans. Plasma Sci.*, vol. 37, no. 5, pp. 659–667, May 2009.
- [132] O. Kylián *et al.*, vol. 357, pp. 5–7, 2015.
- [133] K. G. Kostov *et al.*, *Surf. Coatings Technol.*, vol. 204, no. 18–19, pp. 3064–3068, 2010.
- [134] T. Shao *et al.*, *Appl. Surf. Sci.*, vol. 256, no. 12, pp. 3888–3894, 2010.
- [135] C. Ren, K. Wang, Q. Nie, D. Wang, and S. Guo, *Appl. Surf. Sci.*, vol. 255, pp. 3421–3425, 2008.

- [136] G. Borcia, C. A. Anderson, and N. M. D. Brown, *Appl. Surf. Sci.*, vol. 221, pp. 203–214, 2004.
- [137] T. Homola, J. Matoušek, B. Hergelová, M. Kormunda, L. Y. L. Wu, and M. Černák, *Polym. Degrad. Stab.*, vol. 97, no. 6, pp. 886–892, 2012.
- [138] A. Kuzminova *et al.*, *Polym. Degrad. Stab.*, vol. 110, pp. 378–388, 2014.
- [139] T. Desmet, R. Morent, N. De Geyter, C. Leys, E. Schacht, and P. Dubruel, *Biomacromolecules*, vol. 10, no. 9, pp. 2351–78, Sep. 2009.
- [140] F. Massines and G. Gouda, *J. Phys. D. Appl. Phys.*, vol. 31, no. 24, p. 3411, 1998.
- [141] T. Yokoyama, M. Kogoma, T. Moriwaki, and S. Okazaki, *J. Phys. D. Appl. Phys.*, vol. 23, no. 8, p. 1125, 1990.
- [142] P. Kikani, B. Desai, S. Prajapati, P. Arun, N. Chauhan, and S. K. Nema, *Surf. Eng.*, vol. 29, no. 3, pp. 211–221, 2013.
- [143] A. Van Deynse, N. De Geyter, C. Leys, and R. Morent, *Plasma Process. Polym.*, vol. 11, no. 2, pp. 117–125, 2014.
- [144] J. L. Bohnert, B. C. Fowler, T. A. Horbett, and A. S. Hoffman, *J. Biomater. Sci. Polym. Ed.*, vol. 1, no. 4, pp. 279–297, 1989.
- [145] F. Khelifa, S. Ershov, Y. Habibi, R. Snyders, and P. Dubois, *Chem. Rev.*, vol. 116, no. 6, pp. 3975–4005, 2016.
- [146] A. Kondyurin *et al.*, *Plasma Process. Polym.*, vol. 5, no. 8, pp. 727–736, Oct. 2008.
- [147] F. Palumbo *et al.*, *Plasma Process. Polym.*, vol. 12, no. 11, pp. 1302–1310, 2015.
- [148] M. Strobel and C. S. Lyons, *Plasma Process. Polym.*, vol. 8, no. 1, pp. 8–13, 2011.
- [149] C. A. Schneider, W. S. Rasband, and K. W. Eliceiri, *Nat. Methods*, vol. 9, no. 7, pp. 671–675, Jul. 2012.
- [150] U. R. Rodgers and A. S. Weiss, *Biochimie*, vol. 86, no. 3, pp. 173–178, 2004.
- [151] K. Pielichowski and J. Njuguna, *Thermal degradation of polymeric materials*. Shawbury: Rapra Technology Limited, 2005.

- [152] T. Yamanobe, ‘Structure and Dynamics of Crystalline and Noncrystalline Phases in Polymers’, in *Studies in Physical and Theoretical Chemistry*, vol. 84, 1998, pp. 267–305.
- [153] D. Kandel, *Phys. Rev. Lett.*, vol. 78, no. 3, pp. 499–502, 1997.
- [154] J. A. Venables and H. Brune, *Phys. Rev. B*, vol. 66, pp. 1–16, 2002.
- [155] A. Ghosh, R. Batabyal, G. P. Das, and B. N. Dev, *AIP Adv.*, vol. 6, no. 1, p. 15301, 2016.
- [156] J. R. Morales-Cifuentes, T. L. Einstein, and A. Pimpinelli, *Phys. Rev. Lett.*, vol. 113, no. 24, p. 246101, Dec. 2014.
- [157] L. Tumbek and a. Winkler, *Surf. Sci.*, vol. 606, 2012.
- [158] C. Ratsch, P. Smilauer, A. Zangwill, and D. D. Vvedensky, *Surf. Sci.*, vol. 329, no. 1–2, 1995.
- [159] A. Pimpinelli and T. L. Einstein, *Phys. Rev. Lett.*, vol. 226102, no. 99, p. 5, 2007.
- [160] A. Pimpinelli, L. Tumbek, and A. Winkler, *J. Phys. Chem. Lett.*, vol. 5, no. 6, pp. 995–998, 2014.
- [161] H. Brune, *Surf. Sci. Rep.*, vol. 31, no. 4–6, pp. 125–229, 1998.
- [162] M. Tejima, K. Kita, K. Kyuno, and a. Toriumi, *Appl. Phys. Lett.*, vol. 85, pp. 3746–3748, 2004.
- [163] R. Ruiz *et al.*, *Phys. Rev. Lett.*, vol. 91, no. September, p. 136102, 2003.
- [164] M. a. Groce, B. R. Conrad, W. G. Cullen, a. Pimpinelli, E. D. Williams, and T. L. Einstein, *Surf. Sci.*, vol. 606, no. 1–2, pp. 53–56, 2012.
- [165] L. Vroman, A. L. Adams, G. C. Fischer, and P. C. Munoz, *Blood*, vol. 55, no. 1, pp. 156–159, Jan. 1980.
- [166] V. Švorčík, K. Kolářová, P. Slepíčka, A. Macková, M. Novotná, and V. Hnatowicz, *Polym. Degrad. Stab.*, vol. 91, no. 6, pp. 1219–1225, 2006.
- [167] P. Cools, S. Van Vrekhem, N. De Geyter, and R. Morent, *Thin Solid Films*, vol. 572, pp. 251–259, 2014.
- [168] M. Pelliccione and T.-M. Lu, *Evolution of thin film morphology: modeling and simulations*. Berlin New York: Springer, 2008.

- [169] T. R. Gengenbach, Z. R. Vasic, R. C. Chatelier, and H. J. Griesser, *J. Polym. Sci. Part A Polym. Chem.*, vol. 32, no. 8, pp. 1399–1414, 1994.
- [170] S. Rimpelová, N. S. Kasálková, P. Slepíčka, H. Lemerová, V. Švorčík, and T. Ruml, *Mater. Sci. Eng. C Mater. Biol. Appl.*, vol. 33, no. 3, pp. 1116–24, Apr. 2013.
- [171] M. Morra, E. Occhiello, and F. Garbassi, *Langmuir*, vol. 5, no. 3, pp. 872–876, 1989.
- [172] L. Gao and T. J. McCarthy, ‘Contact angle hysteresis explained’, *Langmuir*, vol. 22, no. 14, pp. 6234–6237, 2006.
- [173] a K. Wright and M. R. Thompson, *Biophys. J.*, vol. 15, no. 2 Pt 1, pp. 137–141, 1975.
- [174] K. Anselme, P. Davidson, a. M. Popa, M. Giazzon, M. Liley, and L. Ploux, *Acta Biomater.*, vol. 6, no. 10, pp. 3824–3846, 2010.
- [175] L. Bacakova, E. Filova, M. Parizek, T. Ruml, and V. Svorcik, *Biotechnol. Adv.*, vol. 29, no. 6, pp. 739–67, 2011.
- [176] Y. Zhang, Y. Fung, H. Sun, D. Zhu, and S. Yao, in *Sensors and Actuators, B: Chemical*, 2005, vol. 108, no. 1–2 SPEC. ISS., pp. 933–942.
- [177] A. Choukourov, A. Grinevich, N. Saito, and O. Takai, *Surf. Sci.*, vol. 601, no. 18, pp. 3948–3951, 2007.
- [178] P. Roach, D. Farrar, and C. C. Perry, *J. Am. Chem. Soc.*, vol. 127, no. 1, pp. 8168–8173, 2005.
- [179] R. Mecham, A. Hinek, G. Griffin, R. Senior, and L. Liotta, *J. Biol. Chem.*, vol. 264, no. 28, pp. 16652–16657, Oct. 1989.
- [180] T. J. Broekelmann *et al.*, *J. Biol. Chem.*, vol. 280, no. 49, pp. 40939–47, Dec. 2005.
- [181] M. S. Wagner, S. L. McArthur, M. Shen, T. A. Horbett, and D. G. Castner, *J. Biomater. Sci. Polym. Ed.*, vol. 13, no. 4, pp. 407–428, 2002.
- [182] W. Chrzanowski *et al.*, *Adv. Funct. Mater.*, vol. 25, no. 2, pp. 193–205, 2015.
- [183] T. Albrektsson, P.-I. Brånemark, H.-A. Hansson, and J. Lindström, *Acta Orthop. Scand.*, vol. 52, no. 2, pp. 155–170, 1981.

[184] R. Zaidel-Bar, M. Cohen, L. Addadi, and B. Geiger, *Biochem. Soc. Trans.*, vol. 32, no. Pt3, pp. 416–20, 2004.

[185] D. H. Kim and D. Wirtz, *FASEB J.*, vol. 27, no. 4, pp. 1351–1361, 2013.

LIST OF TABLES

Table 1	Organic semiconductor molecules and molecular orientation on substrate.
Table 2	A list of parameters a_i and C_i in Eq. (6), for $i = 1-3$ [49].
Table 3	A list of parameters in Eq. (8) simulating the best fit of experimental data.
Table 4	Concentration of chemicals groups in PE film plasma treated under different experimental conditions as detected from the C 1s XPS.

LIST OF ABBREVIATIONS

IC	integrated circuit
CMOS	complementary metal-oxide semiconductor
PEO	poly(ethylene oxide)
PAAC	plasma-polymerized acrylic acid
SK	Stranski-Krastanov
PE	poly(ethylene)
DST	dynamic scaling theory
CZD	capture zone distribution
GWD	generalized Wigner distribution
UHV	ultrahigh vacuum
OMBD	organic molecular beam deposition
QCM	quartz crystal microbalance
RHEED	reflection high energy electron diffraction
XRD	X-ray diffraction
AFM	atomic force microscopy
5A	pentacene
6P	para-hexaphenyl
DIP	diindenoperylene
VPD	vapor phase deposition
CNT	carbon nanotube
UV	ultraviolet
RF	radio frequency
CAP	competitive ablation and polymerization
PTFE	polytetrafluoroethylene
PP	polypropylene
PES	polyesters
PA	polyamides
PU	polyurethane
PEEK	polyetheretherketone
LDPE	low-density polyethylene
PIII	plasma immersion ion implantation

EPR	electron paramagnetic resonance
SDS	sodium dodecyl sulfate
HRP	horseradish peroxidase
AP	atmospheric pressure
DBD	dielectric barrier discharge
HV	high-voltage
PET	poly(ethylene terephthalate)
AC	alternating current
2D	two dimensional
CH	hydrocarbon
XPS	X-ray photoelectron spectroscopy
NMR	nuclear magnetic resonance
CP/MAS	cross polarization magic angle spinning
FTIR	Fourier transform infrared spectroscopy
GPC	gel permeation chromatography
BSA	bovine serum albumin
TE	tropoelastin
PBS	phosphate buffered saline
TCP	phosphate buffered saline
LRR	low deposition rate regime
HRR	high deposition rate regime
DLA	diffusion-limited aggregation
ALA	attachment-limited aggregation
HMA	hot monomer aggregation
WCA	water contact angle
UHMWPE	ultra-high-molecular-weight PE
RMS	root mean square
ECM	extracellular matrix

ATTACHMENTS

Attachment 1

This script demonstrates a visual step-by-step pathway of executed functions to obtain capture zone distribution from a single AFM image.

△

```
i = Import ["C:\\Users\\Yuri\\Desktop\\Dissertation\\CZD Data\\10 sec 1 cut.tif"  
];
```

```
(*Figure 1 - Imported image *)
```

```
Image [i, ImageSize → Medium]
```

```
(*Remove point -like objects *)
```

```
d = DeleteSmallComponents [i, 50 ] ;
```

```
(*Figure 2 - Show the image without small components and islands are black *)
```

```
Image [ColorNegate [d] , ImageSize → Medium]
```

```
(*Create intensity map farther from the island corresponds to higher intensity *)
```

```
(*Figure 3 - Show outcome of the DistanceTransform function *)
```

```
k = DistanceTransform[ColorNegate [d]] // ImageAdjust
```

```
(*Watershed image *)
```

```
l = WatershedComponents [k] ;
```

```
(*Figure 4 - Visualize obtained cells *)
```

```
n = Image [Colorize [l] , ImageSize → Medium]
```

```
(* Figure 5 - Forbid edge cells *)
```

```
p = Image [RemoveBackground @Colorize @DeleteBorderComponents  
@MorphologicalComponents [l] , ImageSize → Medium]
```

```
(*Figure 6 - Superimpose capture zones over islands,  
color intensity corresponds to capture zone area *)
```

```
m = Colorize @DeleteBorderComponents @MorphologicalComponents [l ] ;  
area = SortBy [ComponentMeasurements [m, "Count" ] , Last ] ;  
c = Colorize [m /. area, ColorFunction → "RustTones" ] ;  
x = RemoveBackground @ColorNegate @ImageAdd[d, c ] ;  
(*Before + After, highlight CZ on islands *)  
Image [x, ImageSize → Medium]
```

(*Get capture zone areas *)

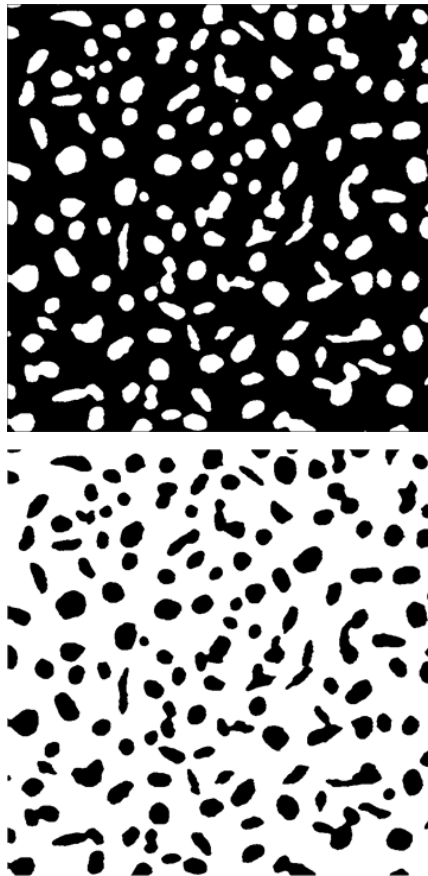
```
a = ComponentMeasurements [l, "Area" ][[ ;; , 2 ] ] ;
```

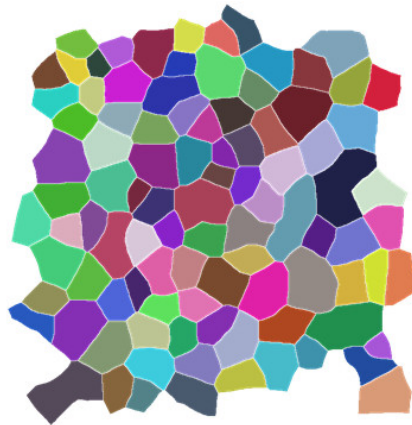
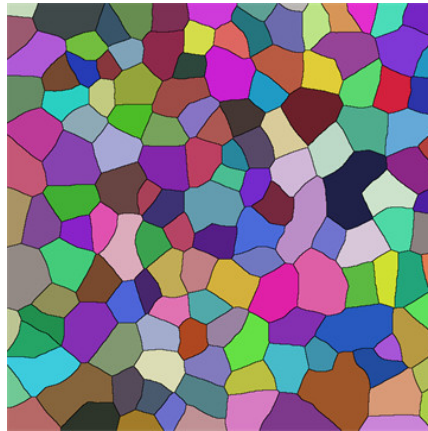
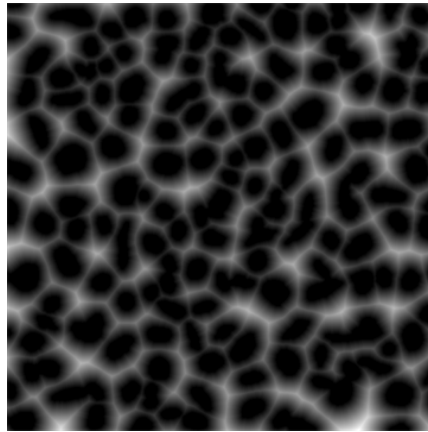
(*Figure 7 - Histogram of Capture Zone Distribution *)

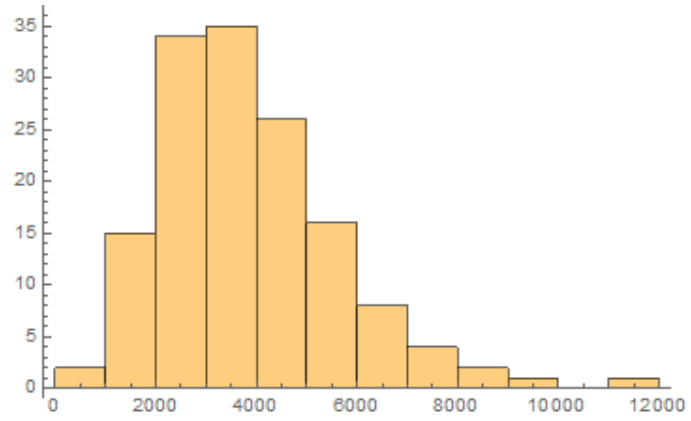
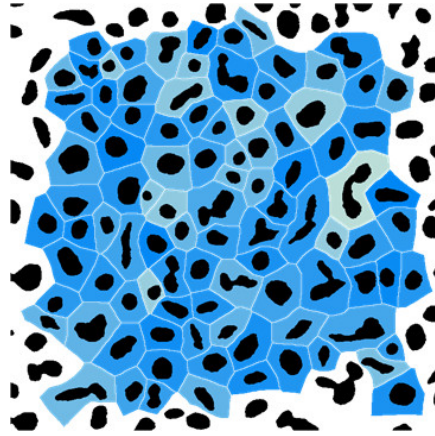
```
Histogram[a ]
```

▲

Outcome of executed commands in the code, the figure order was described in the code:







Attachment 2

This code processes a set of AFM images similarly to Attachment 1. After obtaining capture zone distribution, histogram is normalized and fitted with generalized Wigner distribution.

Δ

```
(*5 images for each sample, name corresponds to deposition time*)
sec1 = {"1 sec 1 cut", "1 sec 2 cut", "1 sec 3 cut", "1 sec 4 cut", "1 sec 10 cut"};
sec5 = {"5 sec 1 cut", "5 sec 2 cut", "5 sec 3 cut", "5 sec 4 cut", "5 sec 5 cut"};
sec7 = {"7 sec 2 cut", "7 sec 3 cut", "7 sec 4 cut", "7 sec 6 cut", "7 sec 8 cut"};
(*removed scratches from AFM images for sec7*)
sec7new = {"7 sec cut 1", "7 sec cut 5", "7 sec cut 7", "7 sec cut 9", "7 sec cut 10"};
sec10 = {"10 sec 1 cut", "10 sec 3 cut", "10 sec 4 cut", "10 sec 5 cut", "10 sec 6 cut"};
sec15 = {"15 sec 5 cut", "15 sec 6 cut", "15 sec 7 cut", "15 sec 8 cut", "15 sec 9 cut"};

(*Collect all images to a big image pool from destination folder*)
o=Table[Import["C:\\Users\\Yuri\\Desktop\\Dissertation\\CZD
Data\\"<image>".tif"],{image, Join[sec1, sec5, sec7new,sec10,sec15]}};

(*Remove very small objects (defects, scratches)*)
oi=Flatten@Table[DeleteSmallComponents[afm, minsize],{afm,o},{minsize,{50}}];

(*Form Voronoi cells and obtain size of each cell not located on the edge of the
image*)
c=ComponentMeasurements[#, "Area"][[;;,2]]&@DeleteBorderComponents@WatershedComponents@DistanceTransform@ColorNegate[#]&/@oi;

(*Combine data of all images and form a histogram*)
cc=Flatten[c];
Nbins= 16;
hsgraph=Histogram[cc, {"Raw", Nbins}];
```

```

hsdata:=HistogramList[cc, {"Raw", Nbins}];

(*Find values of bin width and values of bin center *)
binWidth:=Differences[hsdata[[1]]];
binCenter =hsdata[[1,1;;Length[hsdata[[2]]]]+binWidth/2;

(*Normalization to convert raw histogram N(v) to P(s)*)
(*Finding the sum*)
A= binWidth.hsdata[[2]];
h = hsdata[[2]]/A;
(*Calculate first momentum*)
first= h[;;]]binCenter[;;]];
B= binWidth.first;
(*Define s=v/<v>*)
s = binCenter/B;
(*Capture zone distribution*)
Ps = {s, B/A*hsdata[[2]]};
T = Transpose[Ps];

(* Fit CZD by the single-parameter generalized Wigner distribution *)
ClearAll[s];
modelwigner := n*s^ω*Exp[-m*s^2];
fitw = NonlinearModelFit[T,modelwigner,{n,m,ω},s];
fitw[{"ParameterTable", "RSquared"}];

(*Build a P(s) and a fitting function *)
graph =Show[Plot[fitw[s],{s,0,3},PlotTheme->"Detailed",PlotStyle->{Green, Thick},
  PlotLegends->Placed[{" GWD βw = 2.38"}, {0.72,0.6}],
  ListPlot[T, PlotStyle->{PointSize[0.024],Blue, Opacity->0.4}],
  PlotRange->{{0,3},{0,1.3}},FrameLabel->{"s", "Pβ(s)"}]
▲

```

AUTHOR'S CONTRIBUTION

The author performed all the depositions and treatments but cell adhesion studies. The following post-measurement analyses and measurements were also performed by the author: water contact angle measurements, FTIR, XPS, AFM and image processing.

GPC characterization was accomplished by Jiří Sedlář, NMR measurements by Lenka Hanyková, ellipsometry measurements by Jaroslav Kousal, cell tests by Lucie Bačáková and Marta Vandrovcová. The author participated in processing and evaluation of the data obtained in the mentioned measurements.